UCLouvain

École polytechnique de Louvain

Numerical investigation of droplet trajectories in a raindrop erosion test bench

Author: **Sébastien Masson**
Supervisors: **Yann Bartosiewicz, Thomas Pardoen**
Readers: **Pierre Bollen, Juray De Wilde, Matthieu Duponcheel**
Academic year 2018–2019
Master [120] in Mechanical Engineering

Abstract

As part of a TECCOMA research project in collaboration with industrial partners in the field of aeronautics (Sonaca, Safran Aero Boosters, and Sabca), UCL is developing an erosion test bench to test the resistance of materials to water droplet impacts on the wings leading edges during the flight. Composite materials continue to gain interest in aerospace applications because of their low weight and high strength. However, their use generates wear problems if they are not provided with a specific coating to protect the composite.

The design of the bench consists of a sample installed on a double arm that rotates at high speed in an artificial rain.

The objective of this master thesis is to model and understand the interaction between the drops and the non-realistic velocity field created by the experimental conditions (containment, cyclic wake, etc.) in order to better characterize their impact during the measurements that will be made.

Acknowledgments

I first would like to thank my supervisors, Y. Bartosiewicz and T. Pardoen, and advisers, P. Bollen and M. Duponcheel, who guided me throughout this research, despite my rocky beginnings. They were present for all my questions and always provided wise reflections on my work that pushed me forward. Thanks to them I greatly improved my communication skills and learned how to properly conduct a numerical study. I would like to thank them for their patience.

I'm also grateful to J. De Wilde who accepted to take the time to read my work and be part of my jury.

I wish to thank the Louvain School of Engineering who provided me with the education, facilities and resources, to complete my academic studies.

I thank Conor McMahon that even from Vancouver took the time to proofread this paper.

Finally, I want to express my deepest thankfulness to my family, who have always been there for me and supported me throughout the years. I wouldn't be there without them. Special thanks to my father who proofread this paper.

Contents

1 Introduction **1**

1.1 Context . . . 1

1.2 Description of the test bench . . . 2

1.3 Scope of This Study . . . 4

2 Computational Methodology **5**

2.1 Software . . . 5

2.2 Mesh Generation . . . 5

2.2.1 Inflation Layer . . . 5

2.2.2 Structured vs. Unstructured Mesh . . . 7

2.2.3 Resolution . . . 7

2.2.4 Mesh Validation . . . 9

2.2.5 The Meshes General Information . . . 9

2.3 Flow Field Solution Methodology . . . 10

2.3.1 Flow Solver Description . . . 10

2.3.2 Operating Conditions . . . 11

2.3.3 Boundary Conditions . . . 12

2.3.4 Post Processing . . . 12

2.3.5 Turbulence Model Selection . . . 13

2.3.6 Fluent Input Parameters . . . 14

3 Flow Field Results and Discussion **15**

3.1 2D Sample Analysis . . . 15

3.2 2D Cross Section Analysis . . . 24

3.3 Actuator Disk . . . 31

3.4 Simplified 3D Bench . . . 46

4 Particle Impact Statistics **49**

4.1 Implementation Methodology . . . 49

4.2 Complete Room Analysis . . . 50

4.3 Local Sample Analysis . . . 55

4.4 Reconciliation . . . 58

5 Conclusion **61**

A Validation of the Sample Simplification **63**

B User Defined Function for the Actuator Disk **69**

C 3D Actuator Disk Maximum Height Configuration **75**

D Particle Injection Complete Data Tables **81**

List of Figures

1 CAD model of the complete erosion test bench . . . 2
2 CAD model of the arm and sample holders . . . 3
3 CAD model of different components of the test bench . . . 3
4 Subdivision of the Near-Wall Region . . . 6
5 Illustration of the two wall resolution strategies . . . 6
6 Comparison of an Unstructured (a) and a Structured (b) mesh . . . 7
7 2D Profile of the sample holders . . . 7
8 Example of mesh refinement zones for a 2D domain . . . 8
9 Example of a hybrid mesh generated in a 2D domain . . . 10
10 Execution scheme of the two pressure-based algorithms . . . 11
11 Intermediate mesh of the 2D channel . . . 16
12 Velocity U/U_∞, with streamlines, for the 2D channel . . . 17
13 Velocity comparison between the four 2D channel meshes . . . 18
14 Velocity comparison of the four 2D channel meshes on the symmetrical axe after the profile . . . 19
15 Pressure Coefficient distribution over the chord of the half profile for the four meshes . . . 19
16 Convergence comparison of the different models . . . 20
17 y^+ distribution around the half profile . . . 20
18 Velocity comparison between the two turbulence models . . . 21
19 Velocity comparison of the two turbulence models on the symmetrical axe after the profile . . . 21
20 Pressure Coefficient distribution over the chord of the half profile for the three wall treatments . . . 22
21 The 2D cross section symmetrical domain . . . 24
22 Optimal mesh for the 2D cross section domain . . . 26
23 Velocity U/U_∞, with streamlines, for the 2D cross section . . . 27
24 Velocity distribution on the center trajectory of the profile, for the 2D cross section 28
25 Pressure Coefficient distribution around the sample holder for the three meshes . 29
26 Velocity comparison of the 2D cross section on the center trajectory of the profile 30
27 Actuator disk concept illustration . . . 32
28 Profile comparison between the arm and the modeled profile . . . 33
29 General structure of the User Defined Function used for the Actuator disk . . . 34
30 2D Cross section mesh for the Actuator Disk implementation . . . 34
31 Velocity U/U_∞ comparison between the 2D cross section and the 2D actuator disk 35
32 Velocity U/U_∞ of the Actuator Disk on the coarse mesh . . . 35
33 3D Actuator disk domain . . . 36

34 Domain comparison between the two support heights 37
35 Complete information and representation of the 3D actuator disk meshes 38
36 Streamlines visualization of the room color graded for the Velocity U/U_∞ 38
37 General flow circulation in the room visualization 39
38 Velocity comparisons at the actuator disk's center. Initial mesh on the left-hand side, Fine mesh on the right-hand side 41
39 Velocities comparisons at injection height. Initial mesh on the left-hand side, Fine mesh on the right-hand side 42
40 General flow circulation comparison on the periodic boundary 44
41 Velocity comparison at injection height. Minimum height on the left-hand side, maximum height on the right-hand side 45
42 Simplified 3D bench domain 46
43 Simplified 3D bench mesh 47
44 Velocity U/U_∞ in the simplified 3D bench's center 48
45 Velocity U/U_∞ in the actuator disk's center 48
46 CAD model of the droplet injection mechanism 50
47 Water droplet trajectories with their velocity magnitude, in the minimum height configuration 51
48 Intersecting water droplets with the sample in the minimum height configuration 52
49 Injection locations that intersect the sample for all the tested heights 54
50 Some droplet trajectories in the simplified 3D bench 55
51 Intersecting trajectories comparison between the two domains 57
52 2D Cut of the real sample holder geometry 63
53 Fine mesh for the exact sample holder geometry 64
54 Velocity U/U_∞, with streamlines, on the exact sample holder geometry 64
55 Velocity comparison between the two sample holder geometries 65
56 Velocity comparison of the two sample holder geometries on the symmetrical axe after the profile 66
57 Velocity U/U_∞, with streamlines, close up on the sample front 66
58 Streamlines visualization of the flow in the maximum height configuration (HC), color graded for the Velocity U/U_∞ 75
59 General flow circulation in the room visualization for the HC 76
60 Velocity comparisons at the actuator disk's center. Initial mesh on the left-hand side, fine mesh on the right-hand side 78
61 Velocity comparisons at the lowest injection height. Initial mesh on the left-hand side, fine mesh on the right-hand side 79

List of Tables

1 Mesh Quality Measurements 9
2 Edges size for the 2D channel meshes in chord lengths 17
3 Forces applied on the sample holder for the four meshes 17
4 Drag and Lift magnitude applied on the half sample 22
5 Forces comparison between the two wall treatments 23
6 Edges size of the cross section domain meshes in chord lengths 26
7 Forces applied on the sample holder for the three meshes 28
8 Period fraction of the time, a particle, spent on the sample's trajectory for the four analyzed injection height configuration. (LC stands for Low height Configuration and HC for High height Configuration) 53
9 Periodic fraction comparison between the complete 3D room and the simplified 3D bench analysis 56
10 Probability of impact on a specific sample 59
11 Tube locations for maximum impact probability 60
12 Velocity and Angle of attack of the droplets in the minimum height configuration (LC) 60
13 Forces applied on the two different half profile geometries 67
14 Velocity and Angle of attack for the LC 81
15 Velocity and Angle of attack of the HC for the 7mm injection distance 82
16 Velocity and Angle of attack of the HC for the 2cm injection distance 83
17 Velocity and Angle of attack of the HC for the 2.5cm injection distance 84
18 Velocity and Angle of attack of the HC for the 3cm injection distance 84
19 Velocity and Angle of attack of the HC for the 3.5cm injection distance 85
20 Velocity and Angle of attack of the HC for the 4cm injection distance 85
21 Velocity and Angle of attack of the HC for the 4.5cm injection distance 85
22 Velocity and Angle of attack of the HC for the 5cm injection distance 86
23 Probability of Impact on a specific sample (complete table) 87

1 Introduction

1.1 Context

Since the invention of the airplane in 1903 by the Wright Brothers air transport has known incredible growth. Such a growth that nowadays airplanes are just another way of traveling or shipping. With the development of newer, more efficient, airplanes came a great new deal of technologies. From the turbofan engines to the automatic pilot, a lot has changed since this first one passenger commercial flight of 1914.

One key aspect of a plane's design is its weight. Throughout the years, efforts have been made to make planes more effective and lighter. Historically aluminum has played a great role in aviation since it offers great mechanical properties for a reasonable weight. But nowadays new composite materials are even more effective. Composite materials offer such a good lighter alternative to metallic alloys that inside Airbus planes, the proportion of composite materials, went from 4% in their first plane, the A300, to 53% in their current A350. The parts of the plane where the composite materials have trouble replacing alloys are the external body and engine parts.

The problem with composite materials is that they do not offer a structural solution on their own. Their major drawback in comparison to metallic alloys is their rapid rate of erosion due to dust or water. Solutions are available to improve the resistance to erosion. The composite is either coated with a more resistant material or integrated with another material in a hybrid structure. This implies the need to accurately test and measure the erosion rate of the different implemented solutions. No commercial erosion bench is able to test erosion to dust and water. Three types of erosion test bench exist:

- **Raindrop Erosion Test:** This system is adapted to test the erosion of a material upon water droplet impacts. It is composed of a rotating arm on which samples are fixed. Water injection mechanisms are mounted on the far end of the arms to simulate rain. This test evolves over several parameters: angle of impact, rotation speed of the arm and the trial's duration .

- **Blast Erosion Test:** This system projects particles through a jet onto a sample. The parameters are the speed of the jet, the type and quantity of the particles, the angle of impact and the trial's duration. The jet can be a jet of water or air.

- **Centrifugal Erosion Test:** This system consists of the injection of particles on a rotating table that will expel the particles through small holes thanks to the centrifugal forces. Samples are located on the outside of the disk on a stationary platform. This setup has for its advantage that all types of eroding particles can be easily implemented. It has great control over the speed and angle of attack.

As erosion testing is clearly a major point in the development of new composite materials. The UCL has started the development of a raindrop erosion test bench. This effort is made as part of a TECCOMA research project in collaboration with industrial partners (Sonaca, Safran Aero Boosters, and Sabca).

1.2 Description of the test bench

The aim of the test bench is to investigate the degradation occurring on composite materials due to water droplets impacts at an airplane travel speed of 180 m/s.

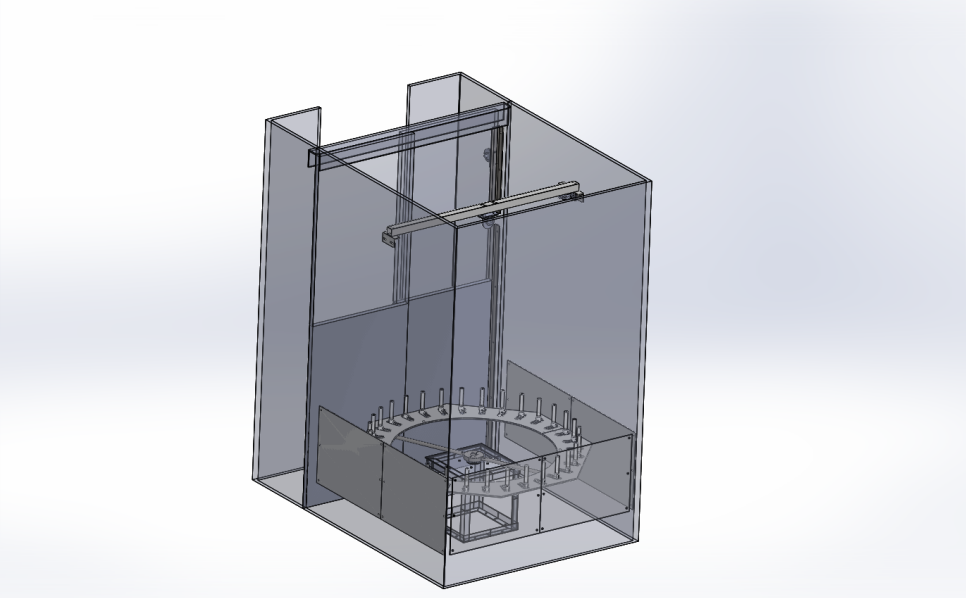


Figure 1: CAD model of the complete erosion test bench

Figure 1 shows the complete bench developed by the UCL. It consists of a double-rotating arm mounted on a motor case inside a dedicated room. The room is a local inside the UCL facilities and is a closed rectangular room of 1.8 × 1.8 meters and 3 meters high. A separation sliding door and wall protections are placed around the arm in case of any mechanical failure. The water injection mechanism will work as follows. A reservoir will feed water to syringes that are piercing through the plug of protecting tubes. Those tubes will protect the water injection at the tip of the syringe to allow the formation of a water droplet. The tubes are mounted in adjustable slots on an octagonal support. This support is attached to the ceiling with a system of pulleys that allows the adjustment of its height.

The arm and the sample holder are presented in Figure 2. This double arm has a diameter of almost 1.61 meters. The sample is a small circular sheet of material whose center is located at a radius of 0.785 meters and has a diameter of 28 millimeters. It is inserted in the open orifice in front of the sample and is held in place by a spring pressing it against the small edge.

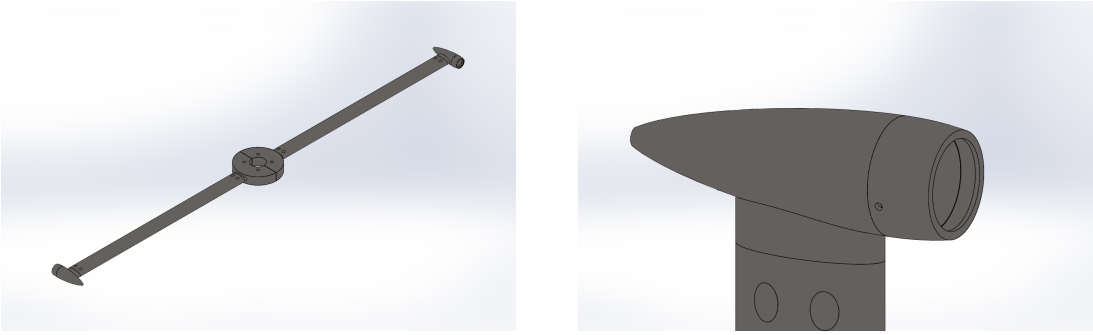
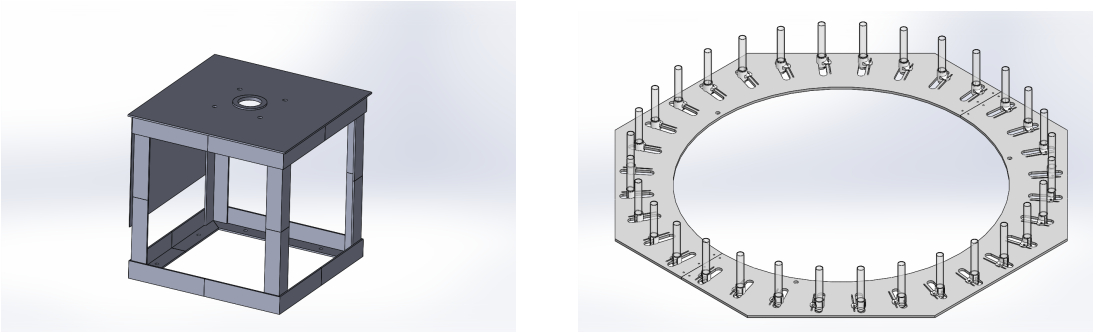


Figure 2: CAD model of the arm and sample holders



(a) Motor Case

(b) Complete Injection Mechanism

Figure 3: CAD model of different components of the test bench

A closer look at the motor case and the injection mechanism is taken in Figure 3. The motor case is 51 centimeters high, 52 centimeters wide and is fixed to the ground. The arms will be mounted on top of it with the appropriate bearing, and inside it will be an electric motor. The injection mechanism is composed of two plates that are held together. The final shape is an octagonal exterior limit with 70 centimeters edges and a circular inner limit with a radius of 62.5 centimeters. There are 32, 13 centimeters long, slots evenly distributed around the circle. In each slot an injection tube of 20 centimeters high and 28 millimeters in diameter can be mounted. Since the support is mounted to the ceiling by a pulley, its height in the room is adjustable. This also has the added advantage to insulate it from the electrical motor and reduce the vibrations. This will help to ensure a good formation of water droplets.

To match the required investigation velocity the arms will rotate at 2190 rpm. This rotation speed allows the center of the samples to evolve at a tangential velocity of 180 m/s. The water droplet injection mechanism is designed to produce water droplets with a diameter of two millimeters. The testing sessions can last as long as water is injected and the arm is rotating.

The main difficulty is to ensure a successful impact of droplets on the sample. And consequently the quantification of the impacts number. This is important in order to determine the deterioration rate of the composite material.

1.3 Scope of This Study

The difficulties encountered could be solved using Computational Fluid Dynamics (CFD) to model the flow created by the arm and determine the optimal location to position the tubes in order to impact the sample. CFD uses numerical analysis to predict and analyze the interaction of fluid flows with different surfaces. Over the years, different numerical models have been implemented and improved. Today it's an important part of design as it is an inexpensive way to find the exact behaviour of a large quantity of flows. However the complete simulation of the room with several different tubes configurations in a time dependent solution is unrealistic to perform. Therefore the problem has to be simplified and then divided into different steps/sub problems to be resolvable.

The first and obvious simplification is the time dependency. Since the flow is occurring inside a closed symmetrical room with a constant velocity, the flow can be time averaged. This simplifies greatly all the problems.

The second simplification will occur on the details that are relevant to the study. Every corner of every point in the room will not be modeled, and some geometric simplification will be applied.

The third and final simplification will concern the final aim of the study. A deterministic solution of the exact droplet injection positions leading to an impact on the exact center of the sample is simply impossible to achieve and also is not useful. Indeed since there is no way to, perfectly, synchronize the arm rotation and the droplet injection, there is no use for a deterministic solution.

In conclusion, the aim of this study is to successfully model the turbulent viscous flow that will be produced by the rotation of the erosion test bench's arms. From this model an investigation on the water droplet's behaviour inside the flow will be performed in order to find a realistic positioning of the tubes to maximize the chances of a droplet impact on the studied samples.

Ideally, the calculation would be performed immediately on the complete 3D bench. But this is not an optimal solution. Indeed the computation requirements for this kind of simulation are huge. Therefore the problem is divided into smaller, more manageable, problems. The first step is to ensure the correct treatment of the flow and select an appropriate model. Then a short study on a 2D cut of the sample holder will be performed to ensure good treatment of the near-wall region. Once all of this is accurate, a simplified 2D cross section of the bench will be modeled to verify the need of a 3D simulation. Then, if the 2D study requires it, a 3D study of the bench will be performed. And finally, once the final flow field is known, the water droplets can be injected inside it to analyze their behaviour.

2 Computational Methodology

In this section, explanations will be given to the different implementation choices made for the model of the erosion test bench. For each step the relevant options will be presented, discussed and the optimal one will be selected. It is understood that the selected options will be used in all the simulations that follows except stated otherwise.

2.1 Software

Computational Fluid Dynamics (CFD) investigations being an important step in the design process a lot of different software are available. This study will be carried with ANSYS Fluent. Fluent is a powerful, user-friendly software that allows the user to choose between numerous options to deliver accurate quantitative predictions. Furthermore Fluent offers a free to use Student license with only a limit on the number of mesh elements. The limit is set to 512,000 elements, which is reasonable for any 2D simulation. The advantage of that limited number of elements is also that it can be performed on a personal computer within an acceptable time. For the 3D simulations, the limited number of elements will be insufficient and the computation on a personal computer will no longer be reasonable. Therefore they will be performed using the full version of Fluent available on the UCL cluster 'Le Maître 3'. The options discussed further are available in Fluent and the ANSYS products. Other options may be available in different software.

2.2 Mesh Generation

The choice of the correct mesh is a critical aspect of the simulation. Its resolution has to be controlled over different areas of interest. In high velocity and pressure gradients, it will have to be refined enough to capture the flow without loss of information. And for less active zones, the mesh should be coarser to reduce the computation time, but not too coarse that it will lead to inaccurate results due to numerical diffusion. The appropriate mesh is essential for an accurate solution, faster convergence and reduction of numerical inaccuracies.

2.2.1 Inflation Layer

The first step is to generate the appropriate mesh around the studied profile. Since the profile's effect on the flow is the aim of the study and that the profile modifies the behaviour of the flow, this is where the resolution will have to be the highest. The interaction between the profile and the flow will create a boundary layer. In the boundary layer, the velocity of the flow decreases non-linearly up to the profile wall where it reaches zero. This is due to the no-slip condition between the wall and the fluid. Figure[1] 4 illustrates the typical non-dimensional velocity u/u_T inside the near-wall region $y^+ = \rho u_t/\mu$ (with the frictional velocity $u_t = \sqrt{\tau_w/\rho}$).

[1] ©ANSYS Fluent Theory Guide

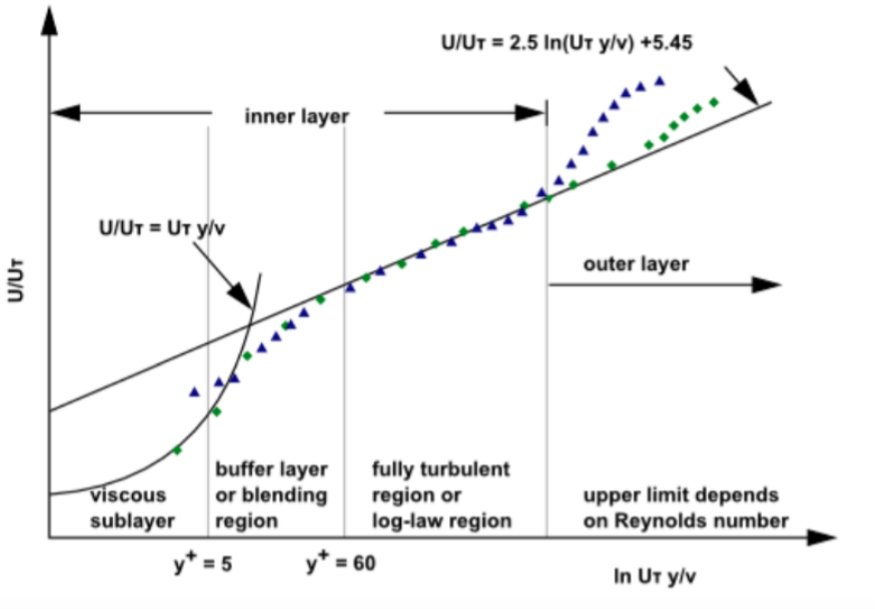


Figure 4: Subdivision of the Near-Wall Region

To accurately predict the near-wall region, inflation layers are used. Two options can be considered. Either the complete resolution of the boundary layer or the use of empirical wall functions. The two options are presented on Figure[2] 5. On the left-hand side, the wall function approach is implemented. It has the benefit to reduce cell count. However for certain flows a complete resolution of the boundary layer profile is necessary and therefore the increase of cell count inside the layer is needed as depicted on the right-hand side.

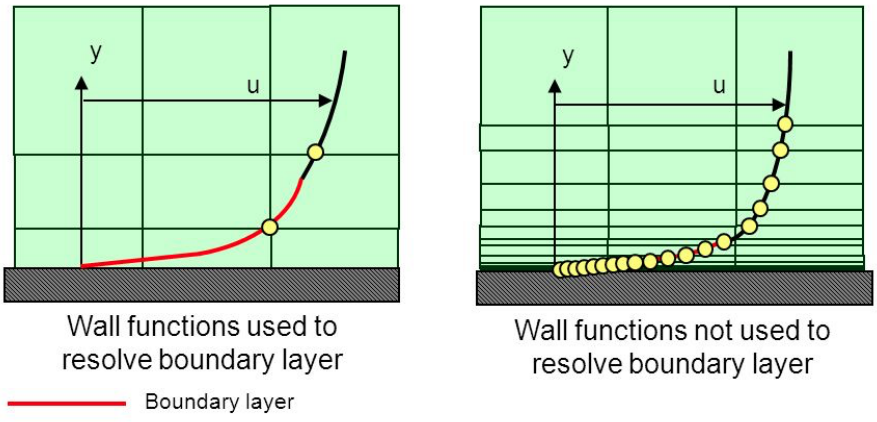


Figure 5: Illustration of the two wall resolution strategies

It is clear that the placement of the first node in the near-wall region is a critical part of the mesh generation. To ensure a correct mesh the non-dimensional distance y^+ is used. The two approaches will have different ranges of y^+. This topic is highly dependent on the turbulence model used and will be discussed in Section 2.3.5. For now consider that the wall function approach will have a first node outside of the boundary layer, typically a y^+ higher than 60

[2] ©2009 ANSYS, Inc.

and the fully resolved boundary layer will count between 10 and 20 nodes inside it, so with y^+ lower than 60.

2.2.2 Structured vs. Unstructured Mesh

The next step is to generate a mesh for the flow field. There exist many methods and those are mainly split in two categories: structured and unstructured/hybrid.

Unstructured meshes are composed of non-orthogonal cells with irregular connectivity. Their shape allows a more accurate caption of complex geometries. This is the reason why they are mostly used for flow fields with multiple components. Unstructured meshes require high computational time and large memory to store elements, nodes and their connectivity.

Structured meshes are mostly composed of quadrilateral cells and allow less memory allocation and less computational time. But are less able to capture complex geometries and accurately follow a curve.

A comparison between a structured and unstructured grid is shown in Figure 6.

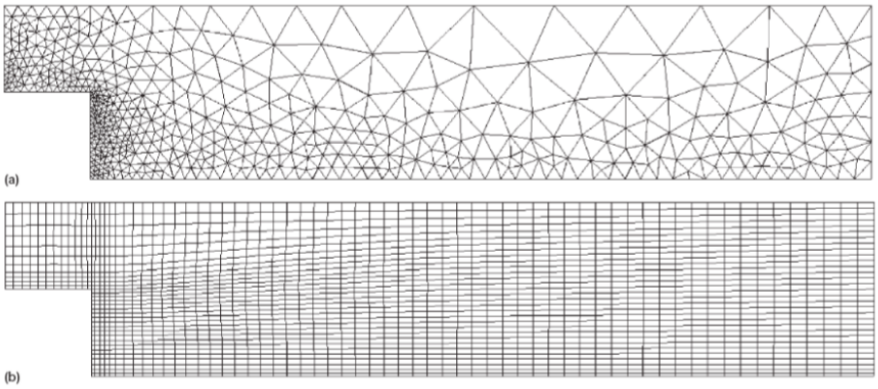


Figure 6: Comparison of an Unstructured (a) and a Structured (b) mesh

2.2.3 Resolution

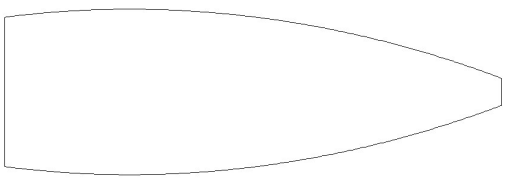


Figure 7: 2D Profile of the sample holders

As stated before an important part of the domain meshing is to ensure a good resolution in the critical areas where the velocity and pressure gradients are the highest. A quick look at the studied aerodynamic profile (Figure 7) and two information can be taken for the mesh

resolution. First, there will be significant pressure gradient in front of it due to the flat front. Second, the wake will be significant. Those two areas will need a fine mesh.

With the ANSYS Meshing software, the refinement of the mesh can be controlled in two ways. The first way is the global control of the domain. This method gives the user control over the main characteristics of the mesh:

- Max/min Size of the cells
- Parameters of adaptation based on proximity, curvature or both.
- Growth Rate

After selecting the desired options, the software will generate a mesh with the requested characteristics.

The second way to control the mesh refinement is to control it locally. This implies a greater effort by the user but ensure better control over the refinement. The local control is essentially a sizing control over specific zones defined by the user. Note that when the mesh is controlled locally certain global parameters are not available but the main ones remain. For instance, the growth rate of the global method will be applied if the local specification does not say otherwise but the adaptation of the mesh near the profile cannot be based on proximity if the local specifications fix its size.

To get the maximum control over the resolution around the profile and the wake, a local zone refinement will be implemented. The refinement zones will depend on the different domains but will mainly be composed of three zones. The closest to the profile has the task to capture the near-profile region and will be the most refined. The second one ensures a good resolution for the front perturbation due to the profile and the near wake, it will also act as a buffer between the near-profile region and the 'far field'. The last zone is the general field, this one is the least refined. Because of its more distant position to the profile, the flow will be less affected and therefore requires less resolution. An example of the 3 zones for the 2D symmetric study of the profile inside a channel is shown on Figure 8.

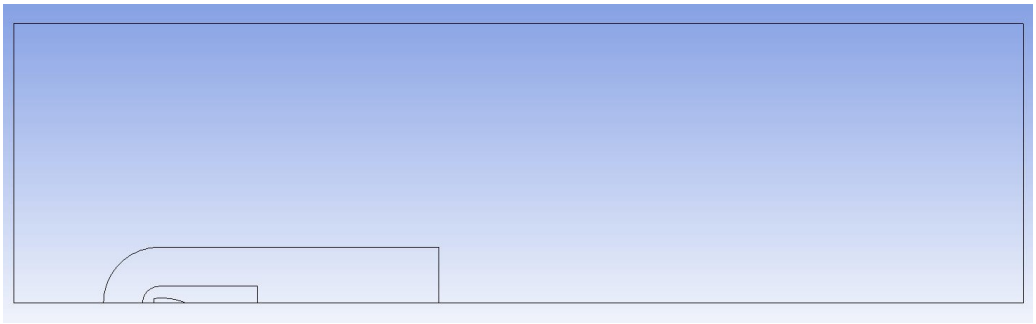


Figure 8: Example of mesh refinement zones for a 2D domain

2.2.4 Mesh Validation

Normally the mesh created by ANSYS Meshing, when the global parameters are used, will be a mesh that ensures a good mathematical convergence. However, since the meshes used in this study are locally controlled by the user, it's important to verify that a good mathematical convergence can be achieved.

To evaluate the quality of the mesh generated it is useful to look at two mesh measurements. The first one is the skewness of the cells. The skewness describes how close a cell is of its equilateral form. According to its definition, an equilateral cell will have a value of 0 and a value of 1 indicates a complete degenerate cell. The second quality is the orthogonality of the cells. The mesh orthogonality is the comparison of the angles between adjacent element faces or edges and their optimal angle (for instance 90^o for a quadrilateral face and 60^o for a triangular face). A value of 1 indicates an optimal angle as a value of 0 indicates the worst possible angle. The appropriate judgment based on the value of those quality factors is shown in Table 1.

	Excellent	Very Good	Good	Sufficient	Bad	Inappropriate
Skewness	0-0.25	0.25-0.50	0.50-0.80	0.80-0.95	0.95-0.98	0.98-1.00
Orthogonal Quality	0.95-1.00	0.70-0.95	0.20-0.70	0.15-0.20	0.001-0.15	0-0.001

Table 1: Mesh Quality Measurements

After mesh generation it is necessary to have the high majority of the cells with a good factor to ensure the numerical stability. If this is the case then the simulations carried with this mesh have good chances to converge towards a solution. For this study, all meshes used were examined to ensure that the majority of their cells achieved a minimum of a good score for both the skewness and orthogonality.

2.2.5 The Meshes General Information

In this study, since the structure is quite simple, a structured quadratic mesh is the best way to go. It will, however, need a refinement near the profile. To ensure maximal control over the resolution of the mesh a zone refinement has been implemented. To keep a homogeneous transition between different resolution zones some of the cells will be triangular. Classing the mesh used as a hybrid mesh.

Figure 9 shows an example of mesh implementation for one of the intermediate studies performed. Each mesh will be briefly presented when appropriate later.

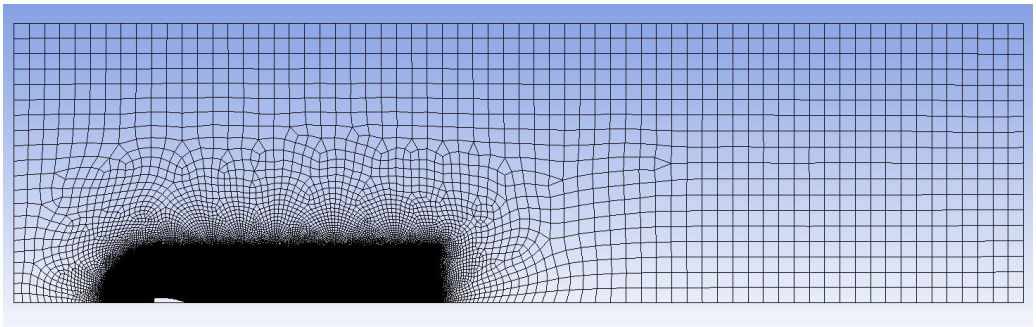


Figure 9: Example of a hybrid mesh generated in a 2D domain

2.3 Flow Field Solution Methodology

As mentioned previously the simulation of the flow will be carried with ANSYS Fluent. The simulation of turbulent compressible flows around an aerodynamic profile involves complex turbulence models and discretization schemes. Fluent is a user-friendly software with a Graphic User Interface (GUI) that allows the modification of a big range of parameters for different models. This section will go over the choice of different turbulence models, how to implement them and select the optimal one for this study.

2.3.1 Flow Solver Description

Fluent offers two numerical methods, the pressure-based solver and the density-based solver. Historically the density-based solver is used for compressible flows and the pressure-based one for incompressible flows. Today, however, both have been modified to successfully solve a wide range of flows. Considering the operating conditions, see section 2.3.2, the reasonable amount of compression, the reasonable speed and the easier accessibility, the pressure-based solver will be used. The pressure-based solver will solve the governing integral equations for the conservation of mass and momentum, and for energy and turbulence. It uses a control-volume-based technique to do so. The domain is first divided into discrete control volumes. Then the integration of the governing equation on the individual control volumes is performed to construct algebraic equations for the unknowns. Finally, it linearize the discretized equations and the solution of the resultant linear equation system is found. The discretization scheme and its order can also be selected by the user. In this case the Second-Order Upwind Scheme will be selected.

The algorithms employed by the solver belong to the general class of projection method. This method consists of repeatedly solving the entire set of governing equation until it converges. Two different algorithms are available. A segregated and a coupled algorithm. A comparison of the two is shown in Figure 10.

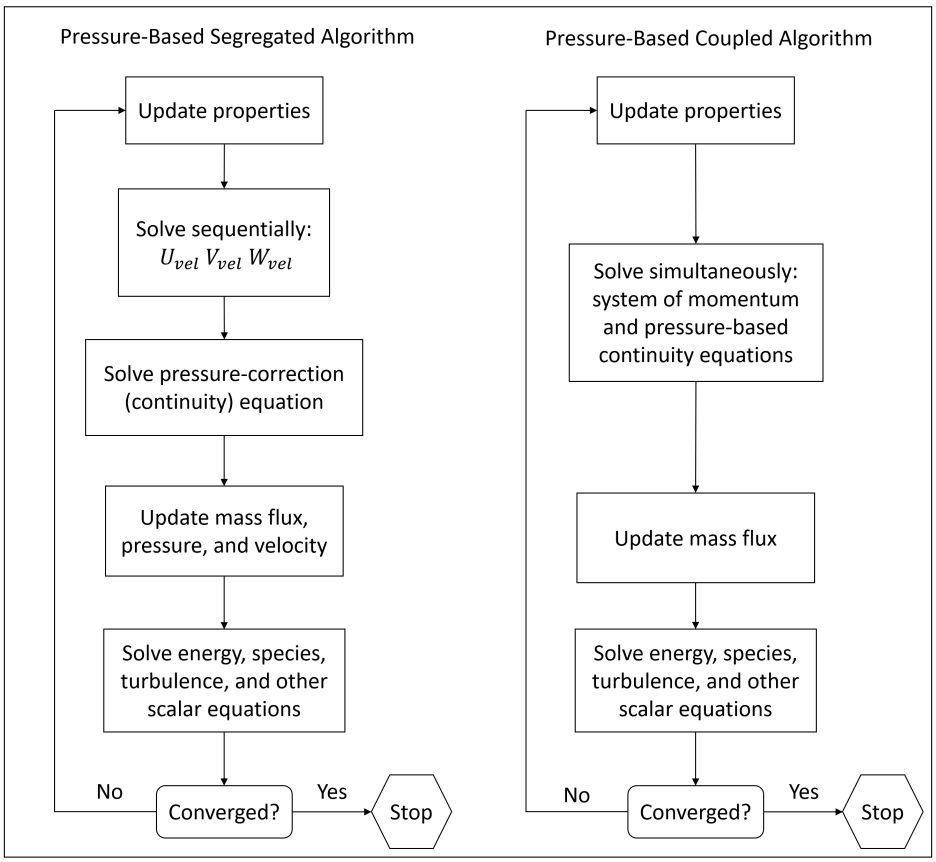


Figure 10: Execution scheme of the two pressure-based algorithms

This study will use the coupled algorithm. Indeed since the momentum and continuity equations are solved in a coupled manner the convergence improves. However more memory is required than in the segregated algorithm but, considering the size of the used meshes, memory is not a constricting factor for this study.

2.3.2 Operating Conditions

The operating conditions will be the first input parameters that the solver will use. To find the correct conditions let's look at where the erosion test bench is located and what its goal is. This bench is operating in a room inside a normal building in Louvain-la-Neuve. Its aim is to study the effect raindrop impacts have on a sample moving in a circular motion with a tangential speed of 180 $[m/s]$.

From its location, it is obvious that it operates under normal conditions of temperature and pressure. Its aim dictates that the main goal is to operate at a flow speed of 180 $[m/s]$ relative to the sample. At this speed the compressibility of the gas is no longer negligible and will thus be taken into account. Hence the air will be treated as an ideal gas.

These observations will be useful to define the input parameters of our simulations.

2.3.3 Boundary Conditions

It is well known that the solution of a simulation will be dependent on the boundary conditions of the problem. Therefore establishing accurate and clear boundary conditions is essential to the correct resolution of any numerical simulation. Fluent offers a wide range of boundary conditions and will not perform any solving iteration if all of the boundaries are not defined. In these studies the different boundary conditions used are viscous isothermal walls, free shear walls, mass flow inlets, pressure outlets, periodic conditions and symmetrical conditions.

The viscous isothermal wall ensure a no-slip condition and a stable temperature. Indeed since compression in closed systems is taken into account it is necessary to ensure a stable temperature. This condition is applied to all the walls and the profile.

Free shear walls are used on boundaries that are assimilated to far-field conditions. Those are essentially the boundaries that are far away from the studied profile and whose only usefulness in the study are to bound the domain.

For the 2D non-periodic studies. Since the simulations are carried with an ideal gas, Fluent does not ensure accurate results if the inlet conditions are velocity based. The inlet condition will be a constant mass flow rate calculated with the formula $\dot{m} = \rho v A$.

The pressure outlet condition will simply fix the outlet pressure at normal atmospheric conditions since it was defined as the operating conditions.

For the periodic studies, a zero pressure drop will be imposed through the periodic boundaries. As for the symmetrical conditions, they will be used when the domain is symmetrical to reduce the mesh size.

2.3.4 Post Processing

Once the simulation has converged and a solution is given some conclusions can be drawn from it. The data that will be analyzed has to be selected carefully. Indeed, it is essential to select global factors that include various data to effectively evaluate the quality of the results. Another point to keep in mind is the relevance of the data to the global aim of the project. It has, for instance, no point to investigate the temperature of the region affected by compression in front of the sample since it has no relevance to the study at hand. Furthermore the data selected will be used to compare results between different meshes of the same domain. This is necessary to ensure that the converged solution is a valid solution to the problem. Indeed the convergence of the mathematical model does not guarantee the accuracy of its solution.

Since the main goal is to determine the trajectories of water droplets in the flow, one result of major importance will be the velocity field of the flow in front and after the sample. This will give an idea of how the droplets could be affected in front of the sample holder and what would happen to them if they miss it.

Another important part of the study is the way the sample holder profile is treated. It is the sample holder that gives its motion to the flow so it is important to know that its effect is properly calculated. To do so, the drag and lift forces of the sample holder will be investigated and compared. The initial guess would have been to compute the drag and lift coefficient but the reason for that selection will become clear once the 3D simulations are explained.

2.3.5 Turbulence Model Selection

One great challenge of the flow field calculation is the turbulence model. Indeed it has been an important area of interest for research and development for the last century. This is explained by the influence that the turbulence model has on the solution. The impact of it is even greater if the area of interest is the boundary layer separation, or complex vortex flows. Each model has its optimal operating conditions and its weak spots. It's critical to select an appropriate model for the studied case. Fluent offers a large selection of models. Two models will be selected and compared to ensure an accurate representation of the flow. The models selected will resolve the Navier-Stokes equations. They are called Reynolds-Averaged Navier–Stokes (RANS) models. To be more specific this study will compare the results of the two equations models, k-ϵ and k-ω. Those models consist of the resolution of Partial Differential Equations (PDE) for their turbulent kinetic energy, k, the turbulence kinetic dissipation rate ϵ for the first one, and the turbulent specific dissipation rate ω for the second one. The resolution of those equations provides the velocity, and length scale needed to solve the RANS model. The two models have their benefits and inconvenience.

$k-\epsilon$ model. The first assumption when using this model is that the flow is fully turbulent, and has a high Reynolds number. It's a widely used model that offers good convergence and isn't memory expensive. However this model has one big limitation. It isn't resolved all the way to the wall. Indeed since the boundary layer isn't only composed of a fully turbulent flow, the model fails. Fluent offers different solutions to handle that limitation that will be discussed later.

Shear-Stress Transport (SST) $k-\omega$ model. The $k-\omega$ model aim is to accurately model the near-wall interaction of the flow. It's a popular model for turbo machinery and flows with strong vortices. Limitations of this model are that it is more sensitive to initial conditions, and that it has more difficulties converging compared to the $k-\epsilon$ model. The SST version was developed later and incorporates the robustness and accuracy of the standard $k-\omega$ model in the near-wall region and the independence of the $k-\epsilon$ model in the free stream region. This is achieved by converting the $k-\epsilon$ model into a $k-\omega$ formulation. This makes the SST $k-\omega$ model more accurate and reliable for more types of flows.

Near-wall treatment. As mentioned before the big difference between the two models is that the $k-\epsilon$ model is not resolved all the way to the wall. Since turbulent flows are significantly affected by the walls, a solution has to be found. Fluent offers two solutions.

For the first one, instead of resolving the wall-bounded region it is replaced with a semi-empirical formula that is called 'wall function'. This formula approximate the velocity profile in the boundary layer based on the y^+ distance of the mesh elements. When using a wall function it is essential to control the mesh refinement in the region near the wall. If the start of the mesh is located inside the boundary layer and has a y^+ value inferior to 15, the results deteriorate.

The second one is the implementation of a two-layer model. The whole domain is divided into a viscosity affected region and a fully turbulent region. The two regions are demarcated by a wall-distance-based turbulent Reynolds number (Re_y). If the local Reynolds number is greater than 200, the region is fully turbulent and the $k-\epsilon$ model is maintained. If it is lower, the one equation model of Wolfstein is implemented. This model requires a high resolution mesh near the profile. The first point has to be located at $y^+ = 1$, and a number of 10 to 20 points have to be inside the wall affected region to provide adequate solution. Fluent offers a function called 'Enhanced Wall Treatment' where it automatically detects if the mesh is fine enough to implement the two layer model, and if not, chose the wall function approach.

As mentioned before the $k-\omega$ model is resolved all the way to the wall. It therefore does not need a different handling of the wall-bounded region. Nevertheless the same refinement of the mesh as the two layer method has to be in place to provide accurate results.

2.3.6 Fluent Input Parameters

Fluent is controlled through a wide range of parameters to perform all kinds of simulations. The scope of this study involves only a few parameters modification. The modified parameters will be presented when they occur, otherwise the default parameters will be kept. Note that since the fluid used is compressible air, the additional options in the turbulence models of 'Compressibility Effects' and 'Viscous Heating', activated by the user, will be considered as default settings in this study.

3 Flow Field Results and Discussion

In this section all the methodology discussed before will be applied to different case studies. Those studies are designed to go from a simple case to more complex ones to achieve the most accurate simulation of the complete erosion test bench's flow field. First a simple study of the sample holder profile will be conducted. This will allow the selection of an appropriate turbulent model for the rest of the simulations. The next investigation will be of a simplified 2D model of the erosion test bench. Once completed the 3D simulations of the test bench will be presented. Those simulation will be the ones used to investigate the droplet trajectory analysis.

3.1 2D Sample Analysis

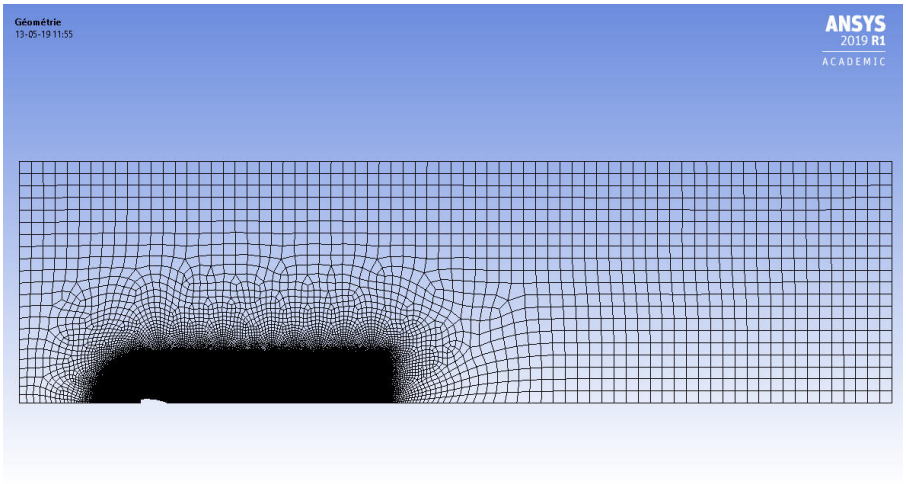
As mentioned before the first step of the simulation is to investigate the turbulence model in order to ensure the validity of the simulation. To do so, a simple symmetrical channel around a simplified sample holder profile will be implemented. The simplification of the sample holder's profile is addressed in Appendix A, and will be used during all this study. The domain is represented in Figure 8. It's a simple 2D channel that is 9 chord lengths high and 33 chord lengths long. The sample holder is located 5 chord lengths after the left boundary and facing it. Two refinement zones are enclosing the profile. The first one (Zone 1) starts 2 chord lengths before the profile and ends 9 chord lengths behind. The second (Zone 2), smaller one, starts only half a chord length before and ends 3 chord lengths behind.

As for the boundary conditions, the left boundary will be a constant mass flow inlet matched through the formula $\dot{m} = \rho v A$ to a flow velocity of 180 m/s. The right boundary is a pressure outlet at normal atmospheric pressure. The upper boundary is a free shear wall, and the lower boundary is the symmetry axe. The profile is, of course, a no-slip wall.

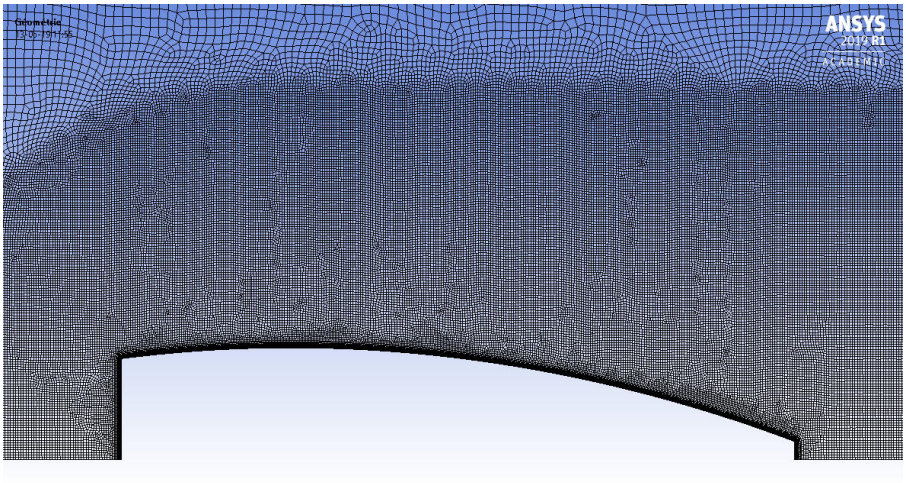
Mesh Validation

To appropriately compare different turbulence models an accurate mesh must be used. Therefore four different meshes will be compared and the optimal one will be used to select a turbulent model. For now, the SST $k-\omega$ model will be used. Since a complete resolution of the near-wall region is performed, it implies a high number of inflation layers around the profile with the first one not further than $y^+ = 1$. This is the only binding constrain, for now. The different refinement sizes of the mesh zones are presented in Table 2, and one meshed domain is visible on Figure 11. Note that the division of the profile edge will be handled in the same way as the second zone refinement.

Figure 12 shows the contour plot of the velocity, with streamlines, achieved inside the domain with the intermediate mesh. As it can be seen, the flow separation with the profile occurs immediately at the flat front of the profile. This was to be expected with such a geometry.



(a) Complete mesh



(b) Zoom on the sample holder

Figure 11: Intermediate mesh of the 2D channel

This creates two strong opposite vortices that develop over and after the profile. The wake after the profile is quite big. The recirculation due to the vortices only stops one and a half chord lengths after the trailing edge and the velocity in the wake stays reduced by half until the end of the domain. This is already an important information since the domain length after the profile is 2 chord lengths bigger than the arc that separates the two sample holders of the erosion test bench. This indicates that there will, more than probably, be interaction between the sample holders and their wakes.

To efficiently compare the different meshes three data will be used. The first ones is the velocity distribution at one chord distance in front and after the sample. The second is the size of the recirculation in the wake of the profile, this will be achieved by comparing the velocity magnitude on the symmetric boundary. The last ones will be the pressure coefficient and the lift and drag forces applied on the half sample holder. Those data were selected for their usability in the studied case and for their relevance in order to accurately model the interaction of the flow with the profile.

	Coarse	Normal	Intermediate	Fine
Channel	1	1	0.5	0.25
Zone 1	0.04	0.02	0.015	0.01
Zone 2	0.01	0.005	0.004	0.003
# of elements	40 885	168 753	262 563	491 081

Table 2: Edges size for the 2D channel meshes in chord lengths

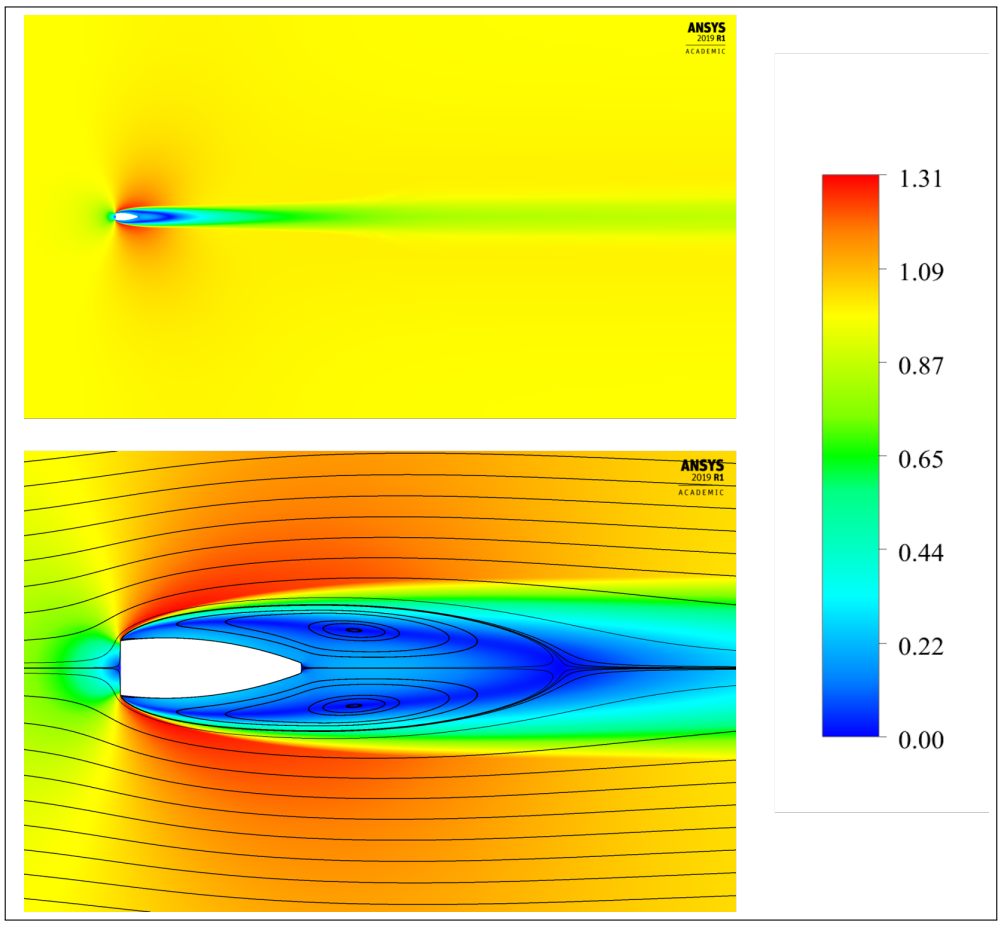
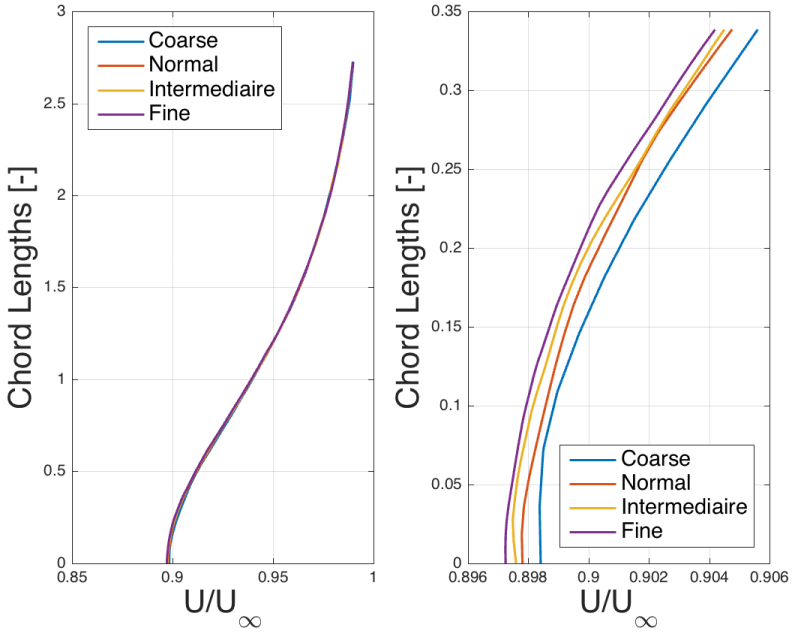


Figure 12: Velocity U/U_∞, with streamlines, for the 2D channel

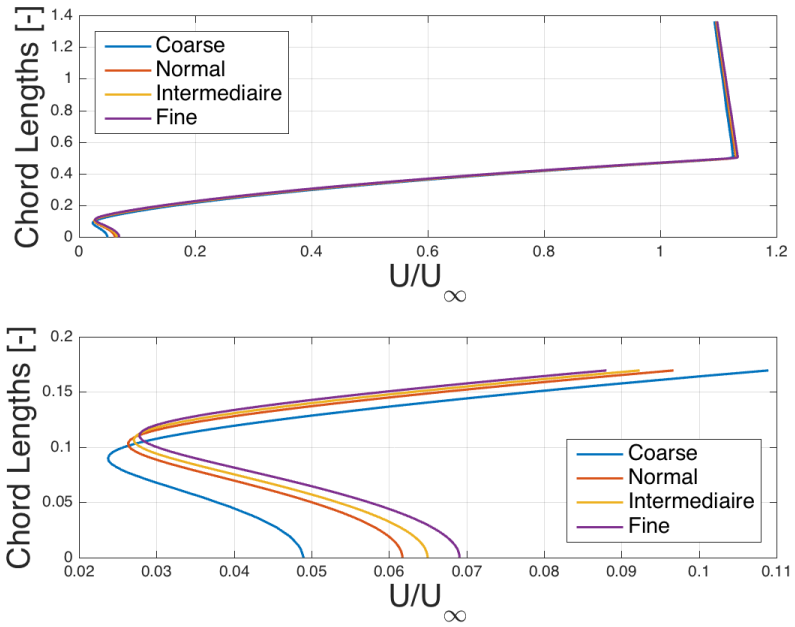
	Coarse	Normal	Intermediate	Fine
Drag [N]	490.130	489.755	490.975	492.032
Lift [N]	1422.607	1424.827	1420.56	1416.934

Table 3: Forces applied on the sample holder for the four meshes

As the Figure 13 is examined, it is obvious that the results of the simulations are very similar. The velocity distributions are almost identical. However the coarse mesh is slightly off (still a difference of 34% in comparison to the fine mesh) and will therefore be considered to coarse in the wake. In comparing the size of the recirculation in Figure 14, the same conclusion can be made for the coarse mesh. It becomes clear that the Intermediate mesh seems to be the middle ground between the normal and fine mesh for the velocity comparison.



(a) 1 chord length in front of the profile



(b) 1 chord length after the profile

Figure 13: Velocity comparison between the four 2D channel meshes

As the next subject of interest is the pressure coefficient on the side of the profile, Figure 15 proves that all the refinements of the profile provide the same results. Table 3 backs that conclusion up for the lift and drag forces (maximum difference between the forces magnitudes is only 0.5 %).

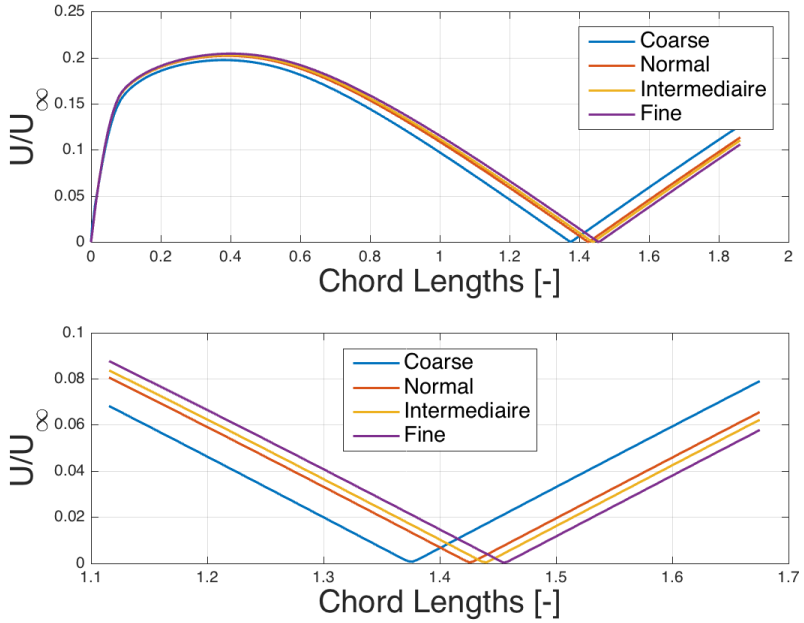


Figure 14: Velocity comparison of the four 2D channel meshes on the symmetrical axe after the profile

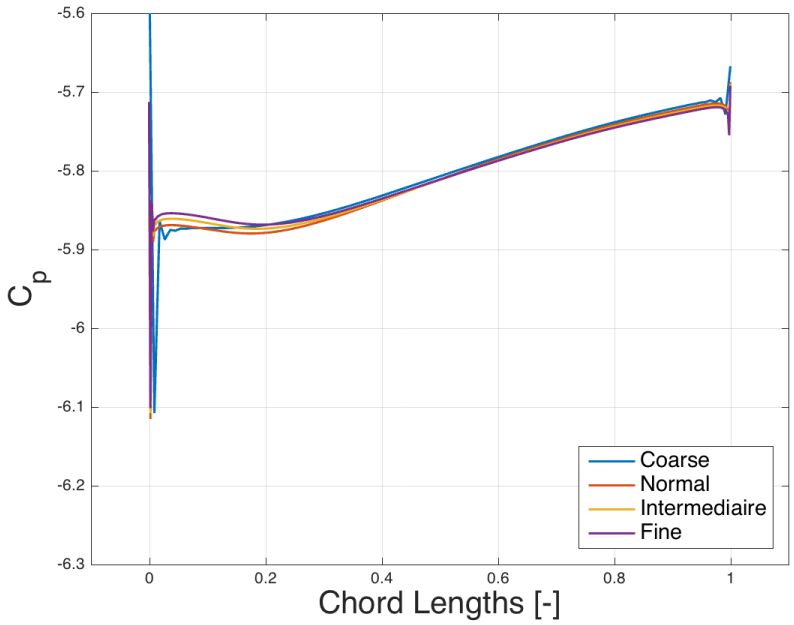
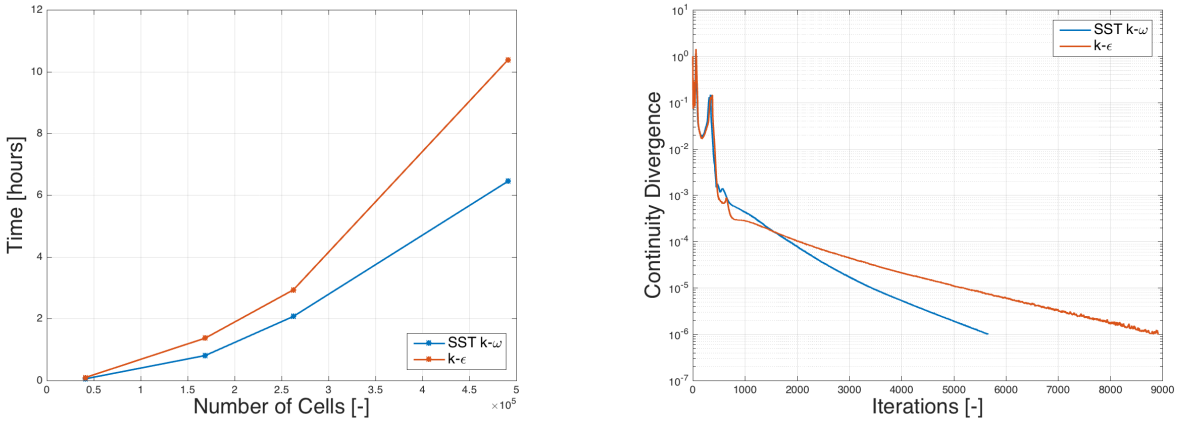


Figure 15: Pressure Coefficient distribution over the chord of the half profile for the four meshes

A final aspect that can be analyzed to determine the best mesh is the computation time needed to converge. Larger meshes will take longer to compute. But, as the time needed to convergence does not follow a linear evolution, it is interesting to see at which point it is no longer advantageous to refine the mesh for better accuracy. Figure 16 shows that the time needed for convergence explodes after the intermediate mesh. It's once more an indication to select this mesh refinement for the turbulence model selection.



(a) Convergence Time

(b) Continuity convergence

Figure 16: Convergence comparison of the different models

Turbulence Model Selection

Now that the intermediate mesh was selected as the optimal mesh, the two different turbulence models can be tested on it. To compare them both on the same ground the $k-\epsilon$ model will use the enhanced wall treatment approach to resolve the boundary layer near the profile. To be certain of the correct resolution, the first mesh point of the inflation layers has to be at a maximum distance of $y^+ = 1$ for both models. To ensure that an estimation of the y^+ value can be made using its definition. With that value fixed for the first inflation point, a preliminary simulation is carried out. The exact y^+ value is then computed from the results and the inflation layers adapted accordingly. Figure 17 shows the computation of the y^+ value for the resolved cases around the profile. The first inflation layer is well below the maximum allowed value.

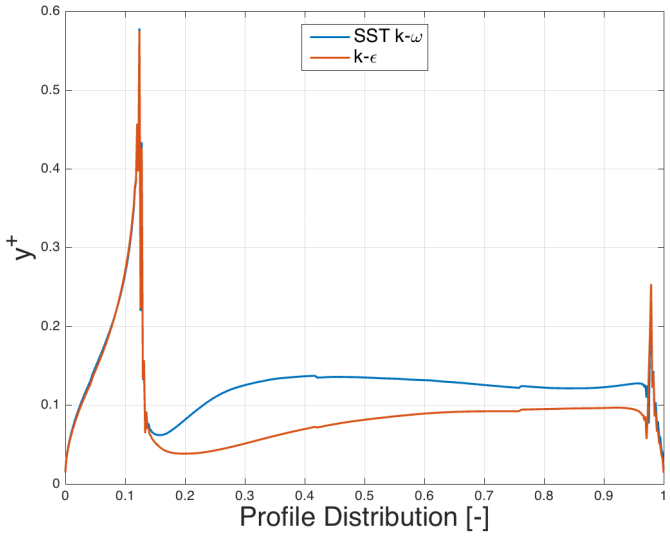
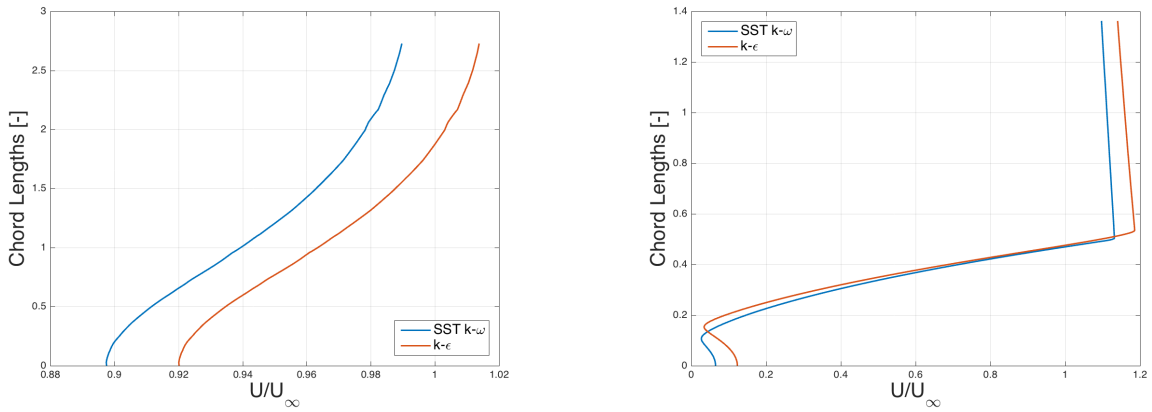


Figure 17: y^+ distribution around the half profile

To compare the two turbulent model the same data will be analyzed as for the mesh validation in the previous section. Since the SST $k-\omega$ model was found to be accurate with those data, the $k-\epsilon$ model will therefore be validated through the comparison process.



(a) 1 chord length in front of the profile

(b) 1 chord length after the profile

Figure 18: Velocity comparison between the two turbulence models

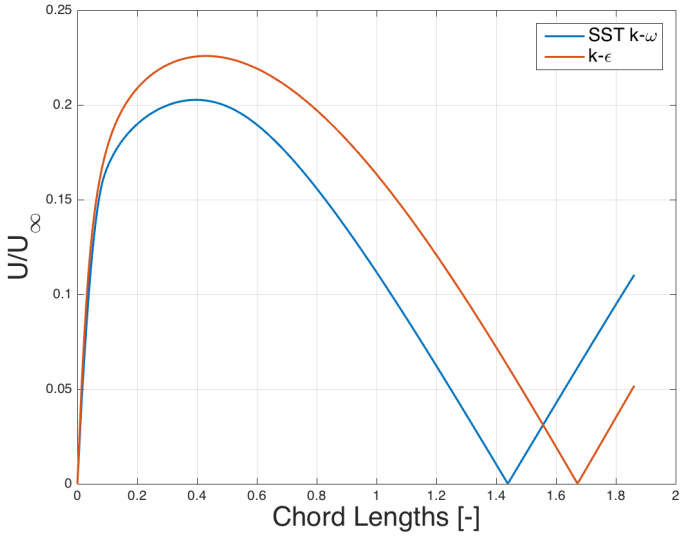


Figure 19: Velocity comparison of the two turbulence models on the symmetrical axe after the profile

As it can be seen on Figure 18, there is a slight difference (2.2%) in front of the profile. As for what happens in the wake, Figure 19 shows that the recirculation after the profile is 13% larger for the $k-\epsilon$ model. This was a bit predictable since the $k-\epsilon$ model has a tendency to diffuse more.

The velocity comparison does not seem to invalidate one of the models, and the difference between the drag and lift magnitudes does not help either, as the maximum difference is, once again, of 2%. To be completely thorough the pressure coefficients of the profile given by the two

	SST $k-\omega$	$k-\epsilon$
Drag [N]	490.975	500.474
Lift [N]	1420.566	1404.532

Table 4: Drag and Lift magnitude applied on the half sample

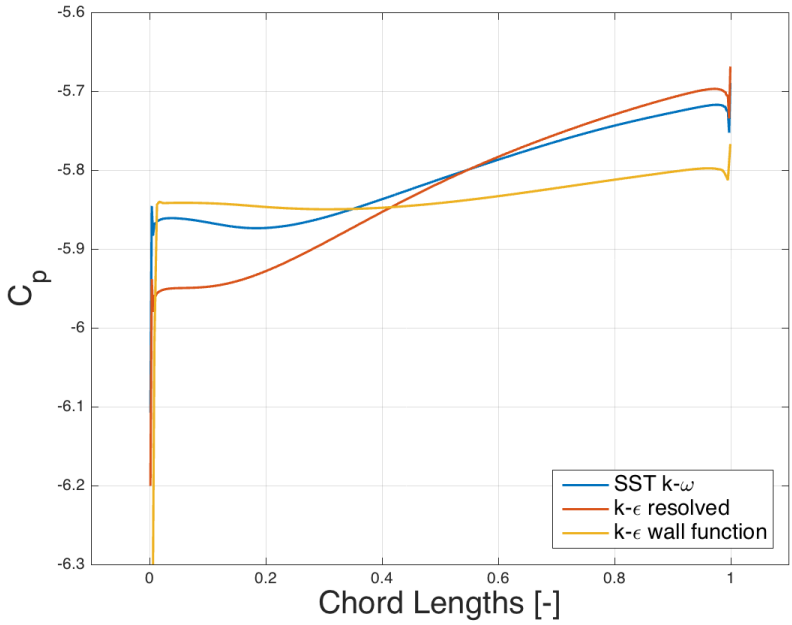


Figure 20: Pressure Coefficient distribution over the chord of the half profile for the three wall treatments

models can be compared. But the inspection of Figure 20 shows once again limited difference (maximum of 2%).

The results show that both of the models are tending to the same solution. This enforced the previous statement that the converge solution is the correct solution.

Wall Treatment Analysis

Since both of the models are converging towards a good solution, both of them are eligible for this study. The next point of interest is the time in which the simulation is performed. One way of reducing it is in reducing the mesh element count and therefore reducing the refinement in the wall affected region. This is possible by using wall functions. As this concerns only the wall, the compared data will be the drag and lift forces, as well as the pressure coefficient. Table 5 shows the different forces. It is clear that the difference of wall treatment enforce a larger difference that the difference of models. However a difference of 5% is still negligible. As for the pressure coefficient difference shown in Figure 20, the difference is also negligible since it does not exceed 2 %.

	Two Layer Method	Wall Function
Drag [N]	500.474	470.122
Lift [N]	1404.532	1336.84

Table 5: Forces comparison between the two wall treatments

Model Selection

In conclusion, the faster convergence of the SST $k-\omega$ model and its natural form that allows it to be resolved all the way to the wall will be used to perform the 2D analysis. This will ensure a very accurate result for the 2D analysis.

However the wall function approach of the $k-\epsilon$ model offers a great reduction of mesh refinement for larger domains, with a limited loss of accuracy. Coupled with the fact that the $k-\omega$ model has to be resolved all the way to the wall to remain accurate, it excludes the $k-\omega$ model for the larger 3D simulations. This is mainly motivated by the crucial aspect of limiting as much as possible the number of mesh elements in the 3D model. And so the $k-\epsilon$ model, in its wall function form, will be used for the 3D analysis.

3.2 2D Cross Section Analysis

Now that the mesh refinement and the turbulence model required to ensure an accurate solution of the flow around the sample holder are selected, the next step is to model a simplified 2D bench. Two options are available, either a 2D plane that will represent the circumference of the circle in which the center of the sample holder revolves, or the 2D cross section of the sample holder in the revolution plane. The combination of the two simulations could be very interesting because a droplet could be injected in the two simulations and with a simple cross reference a 3D trajectory could be computed. Thus eliminating the need for a 3D simulation of the complete erosion test bench.

However, a 2D channel with the circumference's length of the sample holder center will not be modeled. The reason behind it is the way it has to be implemented. In order to be physically relevant, the channel should be periodic. This is imperative to capture the effects of the cyclic wake created by the two sample holders. But, in Fluent, it is not possible to implement periodic conditions that impose a flow in this configuration. This comes from the way the periodic condition has to be implemented. There are two different impositions that can be done to a periodic condition. Either a constant pressure drop is applied through that boundary, or a constant mass flow is imposed through it. For the first one, there is no physical reason to have a pressure drop in a specific location around the sample's trajectory. And for the second one, a constant mass flow rate is impossible to implement with a compressible gas.

The 2D channel also has flows, the main one is that the radial velocity would not be taken into account yet it will have a major effect on the behaviour of the water droplet and the general flow. So modeling the 2D cross section of the erosion test bench will be the 2D study to prepare the 3D simulations. The same concerns can be raised for the implementation of the periodic conditions as for the channel. However in this case the flow is imposed through the rotation of the reference frame and not the boundaries of the domain.

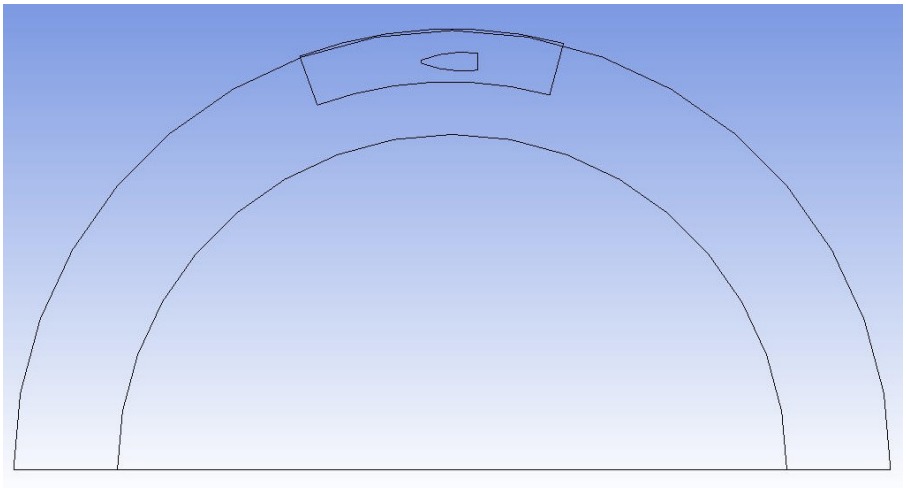


Figure 21: The 2D cross section symmetrical domain

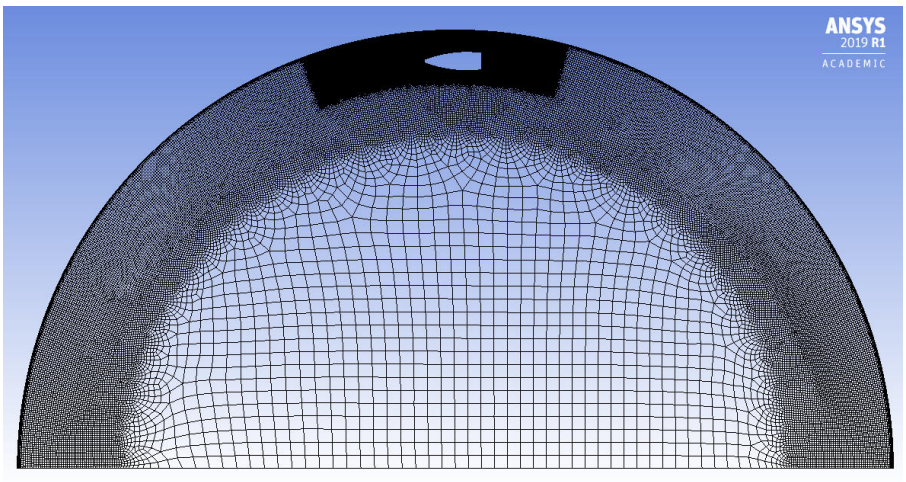
The modeled domain, represented on Figure 21, has a radius of 0.845 meters. It corresponds to the inscribed circle of the octagonal plate holding the droplets injection system. This simplification of the actual domain is needed to ensure the periodicity of the solution. If the real squared wall protections, see description of the erosion test bench in section 1.2, where to be modeled a time dependent simulation would be needed. The sample holder's center is located on a radius of 0.785 meters. That corresponds to the real radial position of the sample. Two refinements zones are enclosing the profile. The first one (Zone 1) encloses the cyclic wake of the profile, this zone is 2 chord lengths high. The second one (Zone 2) is enclosing the profile and the close wall, this is only one chord length wide, start 1.5 chord lengths before the sample and stops 3 chord lengths behind. To match the general direction of the flow, the start and end distances are expressed on the arc.

As for the boundary conditions, the sample holder is a no-slip wall that rotates with the domain at -2190 rpm. The rotation of the domain is necessary to replicate the arm's motion since the flow can't be imposed by the periodic conditions, as mentioned earlier. The outer wall is a stationary no-slip wall, the diameter of the circle is split into two radii. Those are periodic boundaries that impose a zero pressure drop between them.

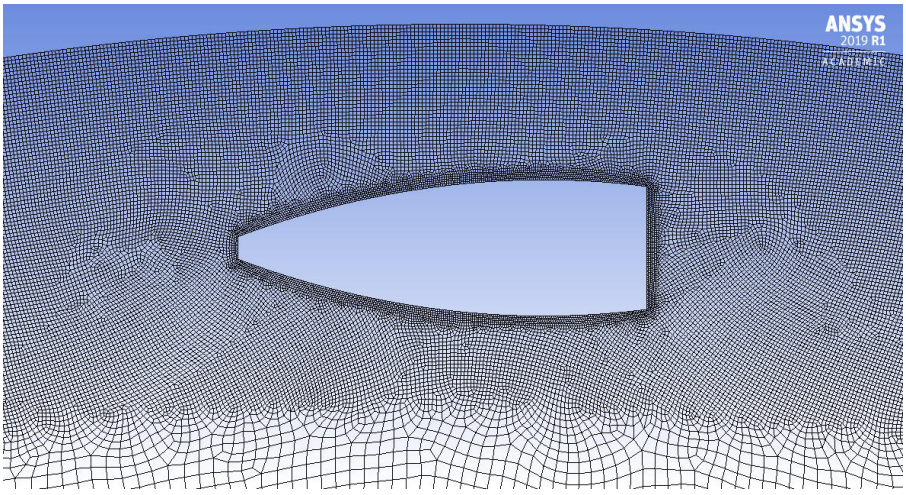
Mesh Validation

Once again a mesh validation is needed. This time the purpose of multiple mesh comparison is two-fold. First there is the critical aspect of ensuring a correct convergence of the solution. Second since the next step is a 3D modeling of the bench, an optimal mesh refinement that can be exported in 3D has to be selected. Indeed, since 3D modeling adds an enormous amount of mesh elements, a reasonable compromise between refinement and solution error has to be found to implement a usable 3D mesh.

Since the analysis of the 2D sample holder's profile was already conducted, the starting mesh resolution is already known. However, the refinement zones are bigger in this domain so the edges size factor could not be kept. It had to be slightly coarsened in order to keep a similar number of elements inside the domain, and therefore under the 512,000 limit imposed by the student version of Fluent. This does not really affect the accuracy of the results since they will be tested. To validate that mesh resolution one coarser and one finer mesh will be implemented and their velocity at the center of the sample holder's trajectory will be compared. A similar comparison of the wall treatment than the previous analysis will also be performed. The lift and drag forces on the sample holder will be compared as well as the pressure coefficient distribution around its profile. The different mesh resolutions are presented in Table 6, and one meshed domain is visible on Figure 22.



(a) Complete mesh



(b) Zoom on the sample holder

Figure 22: Optimal mesh for the 2D cross section domain

	Coarse	Initial	Fine
Domain	0.3	0.25	0.25
Zone 1	0.04	0.02	0.015
Zone 2	0.01	0.0075	0.005
# of elements	76 825	214 086	415 365

Table 6: Edges size of the cross section domain meshes in chord lengths

Figure 23 shows the velocity of the flow inside the simplified cross section domain. In examining the complete domain, it is obvious that the sample holder drives the air significantly on its trajectory but does not seem to drives the inner half of the domain. This was to be expected in sight of the observations made on the previous domain. Since the wake was longer than the distance between the two sample holders and its height not too big. The comparison of the velocities achieved in the wake of this domain and the previous one shows that they are in the same order of magnitude. About half of the sample holder's target velocity.

When zooming on the sample holder itself, the behaviour of the flow near its profile can be examined. On the inner part of the trajectory, the flow separates immediately at the front of the profile as observed in the previous domain. However the presence of the wall on the outer part of the trajectory, and the reduced relative velocity of the flow, modifies greatly the vortices behaviours. On the wall side, the wall pushes the flow back on the profile. This creates a small vortex on the upper front of the profile. This is a separation bubble due to the reattachment of the flow to the profile. The only vortex present after the profile is there for the inner one.

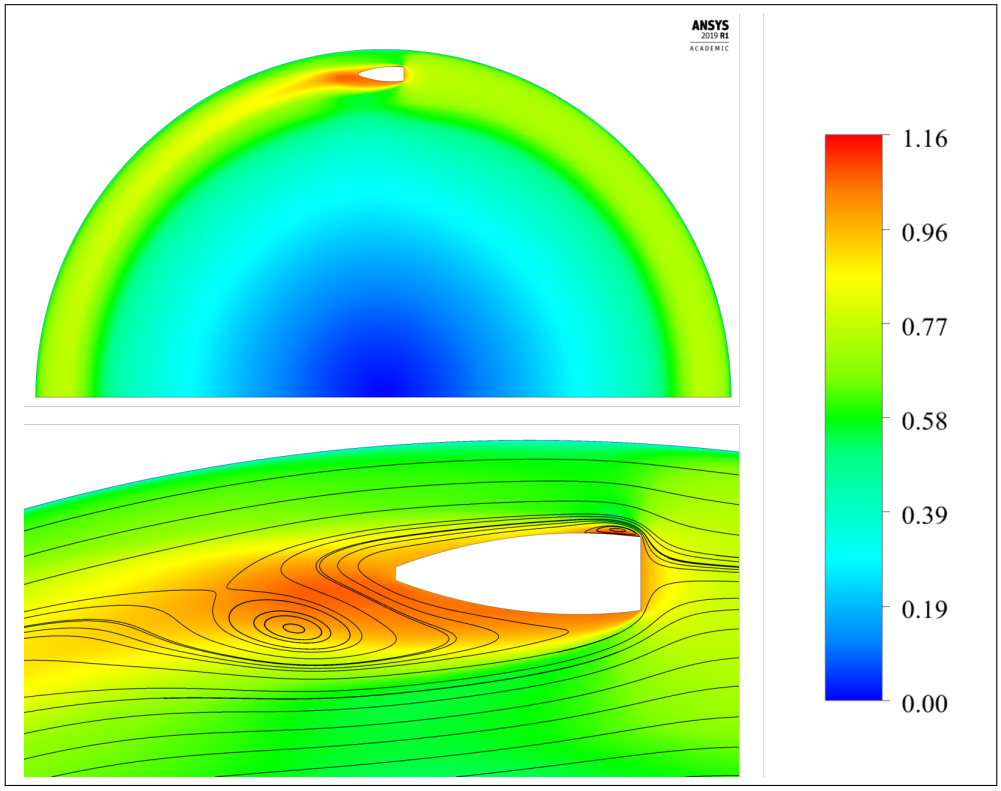


Figure 23: Velocity U/U_∞, with streamlines, for the 2D cross section

Figure 24 shows the general velocity on the sample holder's center trajectory for the finest mesh. The differences with the finer of the two others are shown in the Figure 26. All the differences are below 5%. This is not a significant difference which ensure the accuracy of the converged solution.

The examination of the forces on the sample holder shown in Table 7 shows also no major difference and ensure a good treatment of the boundary layer. The same can be said of the pressure coefficient distribution shown in Figure 25. The distribution is here very similar except when a closer look it took at the front of the curve. The intersection of the upper and lower parts, happening at 0.2 chord lengths from the start, does not occur for the coarse mesh. For the coarse mesh, it takes place right at the beginning. This is probably due to the difference in sizes of the recirculation bubble discussed earlier. The coarser mesh has difficulties computing it precisely. This could disqualify it to be selected as an accurate mesh. However, since the general flow seems unaffected, and that the forces are consistent, this will not be the case.

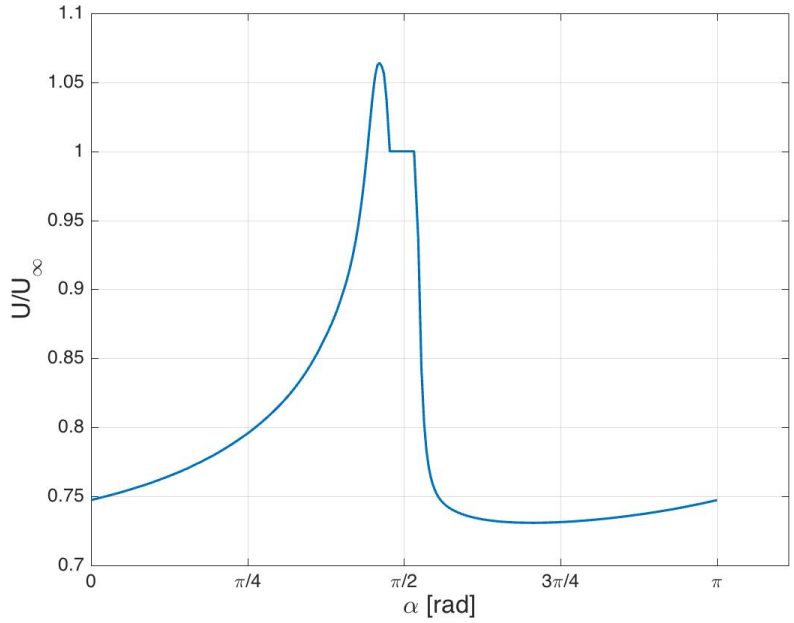


Figure 24: Velocity distribution on the center trajectory of the profile, for the 2D cross section

	Coarse	Initial	Fine
Drag [N]	79.95	81.56	87.19
Lift [N]	65.97	68.10	72.6

Table 7: Forces applied on the sample holder for the three meshes

Now that the solutions have been confirmed it is time to compare them to find an optimal first try refinement for the 3D mesh of the bench. During this selection, it is important to keep in mind that, the smaller the refinement is, the bigger the impact it has on the number of elements. This is quite obvious since the added dimension. Therefore the first tried mesh will be a combination between the coarse mesh, for the domain and Zone 2, and the initial one, for Zone 1. The choice of the coarser mesh in the closest zone to the sample holder could be criticized due to its feeble capacity to model the recirculation bubble pointed in the pressure coefficient examination. But since the 3D analysis will be carried out using the wall function approach the recirculation bubble is not a problem. Indeed the wall function is not able to model the detachment and reattachment of boundary layers.

The difference for the velocity distribution of the optimal mesh and the finest is shown in Figure 26 and it is clear that it never exceeds 5% even at the most critical zones directly before and after the sample holder.

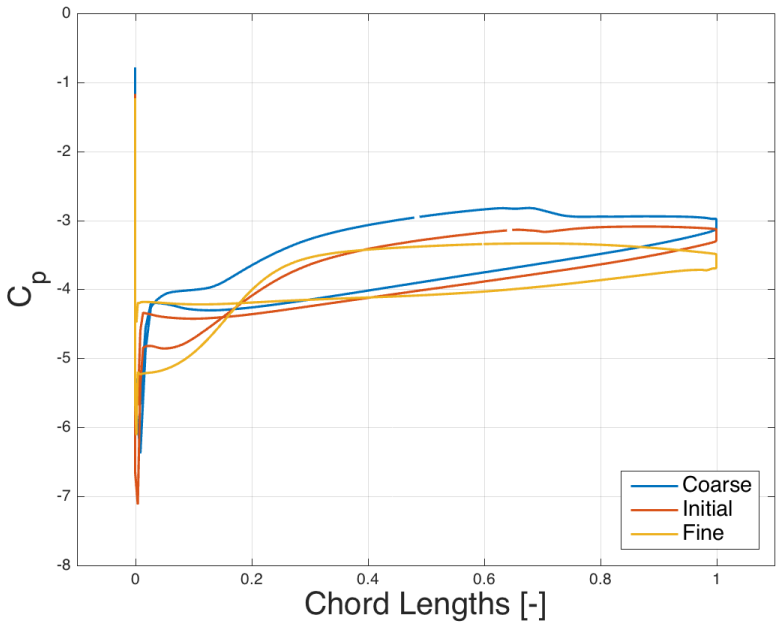
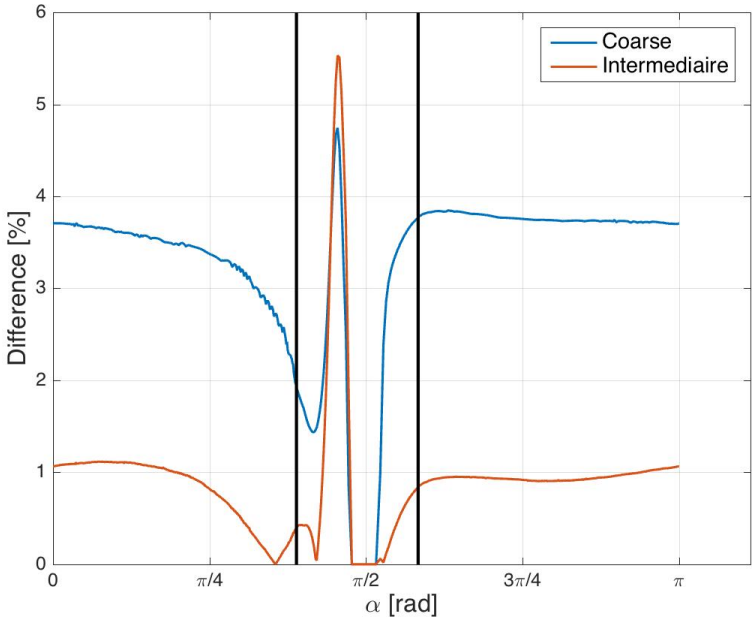
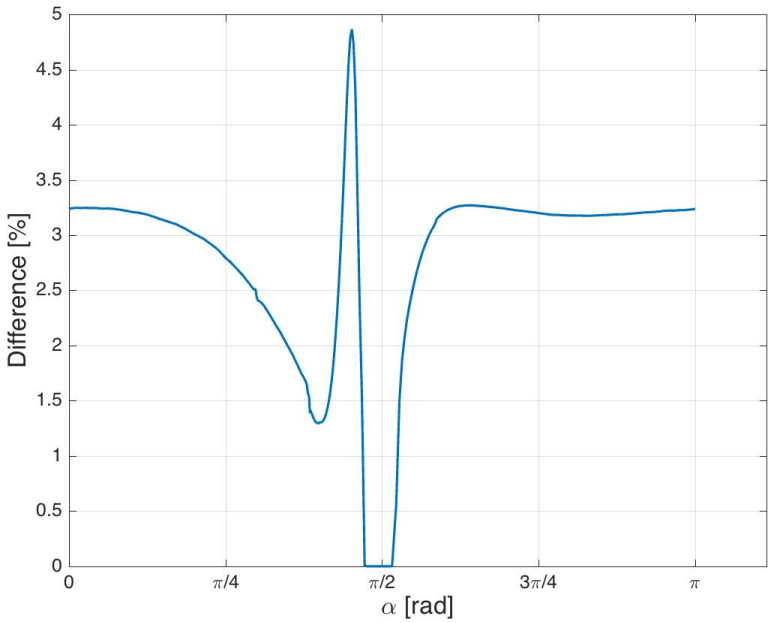


Figure 25: Pressure Coefficient distribution around the sample holder for the three meshes



(a) Difference with the finest mesh



(b) Difference between the finest and the optimal meshes

Figure 26: Velocity comparison of the 2D cross section on the center trajectory of the profile

3.3 Actuator Disk

Now that the 2D preliminary analysis is completed the 3D analysis can be carried out. It has been proven that the $k-\epsilon$ and SST $k-\omega$ model are relevant for this study and a general order of mesh refinement requirements is known. As mentioned before, the size of the mesh is an important factor that has to be taken into account. It is relevant to reduce the time needed to converge and also to reduce the memory usage. For this reason the complete resolution of the boundary layers on the walls in the near-wall region is not possible. This will automatically select the $k-\epsilon$ model with its wall function approach to be the one used for the 3D simulations. Another essential aspect of the mesh size limitation is to keep the number of elements under a maximum of 15 million in order to get a reasonable solving time.

As those considerations are taken into account, a problem is raised. It is not possible to allow enough refinement in the near-wall regions and the general flow in the room with those limitations. The problem has to be divided into smaller manageable ones. That's where the actuator disk method becomes useful. Indeed the actuator disk method, usually used in wind farm modeling, has the benefit of reproducing the effect of the wind turbine blades without having to actually solve the real flow around the blades. In this case it will be used to reproduce the effect of the rotating arms and therefore the flow that it induces in the room. After those effects are known, a smaller domain can be used to capture the flow around the actual arm. Those two separated analyses, combined, will ensure a sufficient knowledge of the flow characteristics to perform the study of the water droplets trajectories.

Actuator Disk Concept

An actuator disk aim is to replicate the effects an aerodynamic component has on the flow without having the actual component in the flow domain. This is done by imposing specific conditions in the domain to replicate the actual effects of the aerodynamic component. This can be done through various methods, the typical one is the application of an equivalent force on the flow in the concerned area of the domain. In Fluent, those forces will be transferred to the flow as a source term added in a specific area by a User-Defined Function (UDF). The following part describes in detail the reasoning behind the forces imposed to the flow[3].

As the actuator disk replaces the global effect of the blade on the flow, it has to be time-averaged. This implies that the forces on the flow will be averaged over the period of an element revolution:

$$T = \frac{2\pi}{N\omega} \tag{1}$$

The force on an infinitesimal blade element can be computed using the decomposition on Figure 27. The instantaneous drag and lift of an infinitesimal blade element of radius ∂r and

[3]The mathematical reasoning is based on the paper of F. Amer and I. Dobrev [14]

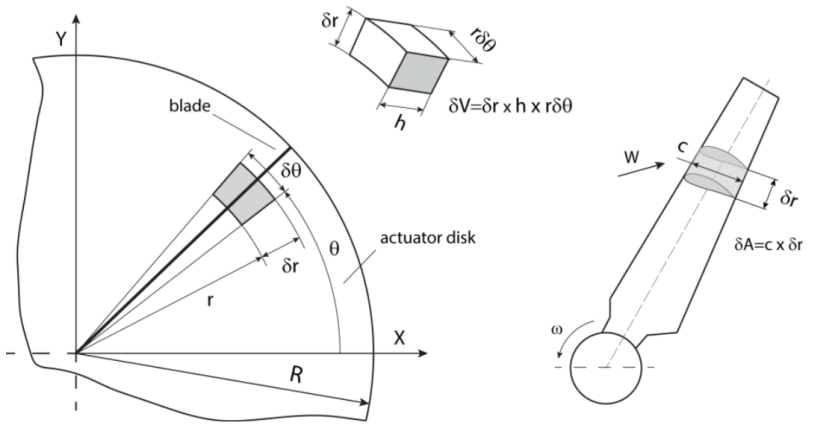


Figure 27: Actuator disk concept illustration

angle $\partial\theta$ during the time $\partial t = \partial\theta/\omega$ is:

$$\partial F_i = \partial F_{D,L}\frac{\partial t}{T} = \partial F_{D,L}\frac{N\partial\theta}{2\pi} \tag{2}$$

The blade element theory decomposes an infinitesimal force as:

$$\partial F_{D,L} = \rho\frac{W^2}{2}C_{D,L}\left(\alpha\right)c\partial r \tag{3}$$

Where, W is the relative velocity magnitude, $C_{D,L}$ the drag/lift coefficient of the profile, and c the chord length. As Eq. 3 is replaced in Eq. 2 the force on one element is given by:

$$\partial F_i = \rho\frac{W^2}{2}C_{D,L}\left(\alpha\right)c\partial r\frac{N\partial\theta}{2\pi} \tag{4}$$

Since that force is applied to an infinitesimal volume of $dV = \partial r \times r\partial\theta \times h$ the force intensity is:

$$f_{D,L} = \frac{\partial F_i}{dV} = \rho\frac{W^2}{2}C_{D,L}\left(\alpha\right)c\partial r\frac{N\partial\theta}{2\pi}\frac{1}{\partial r\partial\theta h} \tag{5}$$

$$f_{D,L} = \rho\frac{W^2}{2}C_{D,L}\left(\alpha\right)c\frac{N}{2\pi r h} \tag{6}$$

With $W = \sqrt{\left(\omega r + u_t\right)^2 + u_a^2}$ where, u_t is the tangential velocity, and u_a is the axial velocity.

Calculation of the resulting force in this manner allows to model the blades as a flat disk. This would have the effect of putting the force distribution on a flat disk in the domain. For mathematical stability this is not an optimal solution. To ensure a stable transition between a source cell and a normal cell, it is useful to smooth the force over a certain distance. That's why the force obtained will be applied with a Gaussian distribution over the actuator disk height. The generic Gaussian distribution is:

$$G\left(z\right) = \frac{1}{\sigma\sqrt{2\pi}}\exp -\frac{1}{2}\left(\frac{z-\mu}{\sigma}\right)^2 \tag{7}$$

Where, μ is the center of the force application, and $h = 3\sigma$ which ensure that the sum of all source terms will be at least 99% of the calculated drag/lift force.

Finally, the force obtained above is expressed inside the reference plane of the actuator disk but Fluent uses the general Cartesian coordinate system to implement the source term. The lift force is simply transferred on the z-axis but the drag will be expressed differently on the x- and y-axis:

$$f_x = -f_t \sin(\theta) G(z) \quad f_y = f_t \cos(\theta) G(z) \quad f_z = f_l G(z) \tag{8}$$

In this case there are two different forces that have to be taken into account. The first one is the force of the sample holder. This one is known since it has been calculated during the 2D cross section analysis. Therefore the force will not be calculated with Eq. 3 but will be extracted from the fine results of the 2D cross section analysis in Table 7.

The second one is the forces of the arms and can be estimated with the known measures taken on a similar profile. However no extensive studies of thick elliptical profiles at high Reynolds numbers have been made since it's not really an optimal aerodynamic shape. Therefore the thickest profile available will be selected and its lift and drag coefficient will be multiplied by 1.5 to take into account the difference in shape and thickness of the profile. This factor comes from the comparison with the low Reynolds characteristics of a similar elliptical profile[1] as this case and the profile selected for the model. The selected profile is a Griffith 30% suction airfoil. It is represented in comparison to the arm profile in Figure 28.

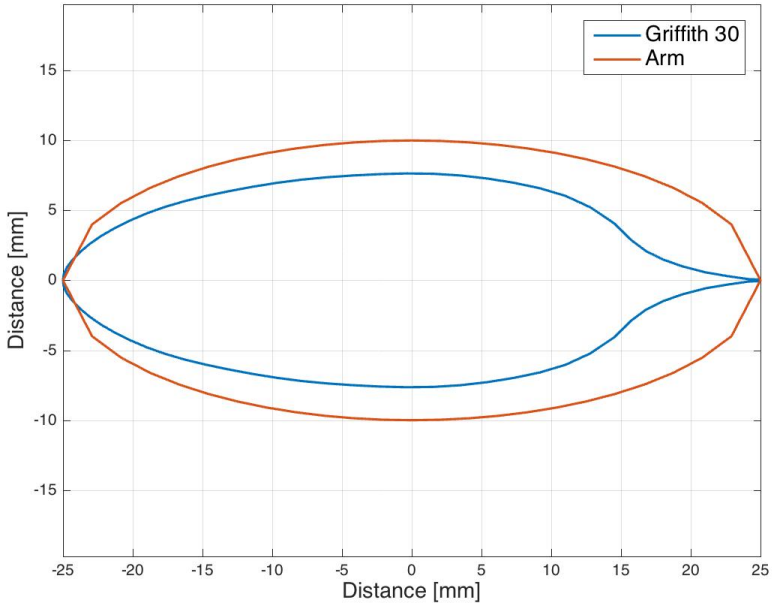


Figure 28: Profile comparison between the arm and the modeled profile

The code used as UDF for Fluent is visible in Appendix B. The UDF will implement either the calculated force on the sample holder trajectory or the equivalent force of the arm on this trajectory. The general structure of the UDF is shown on Figure 29.

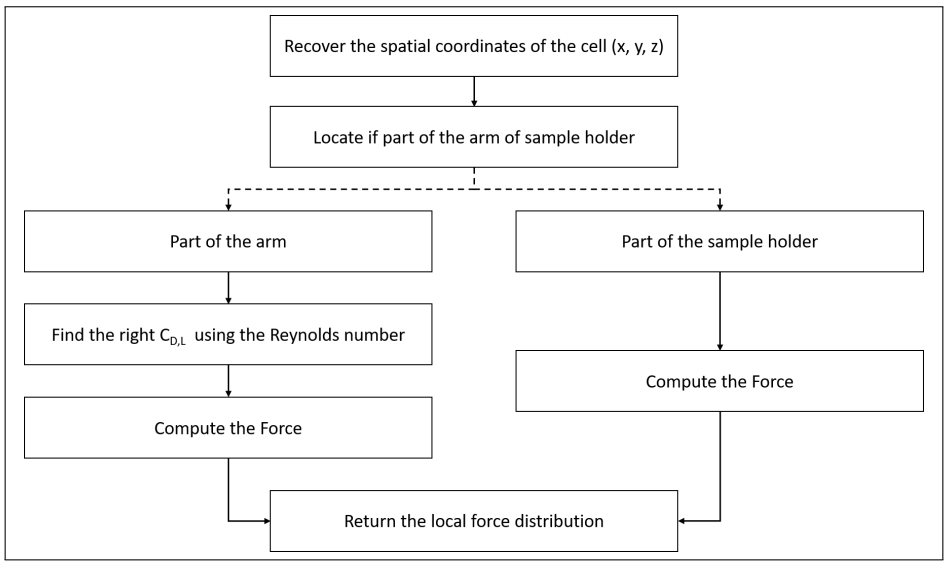


Figure 29: General structure of the User Defined Function used for the Actuator disk

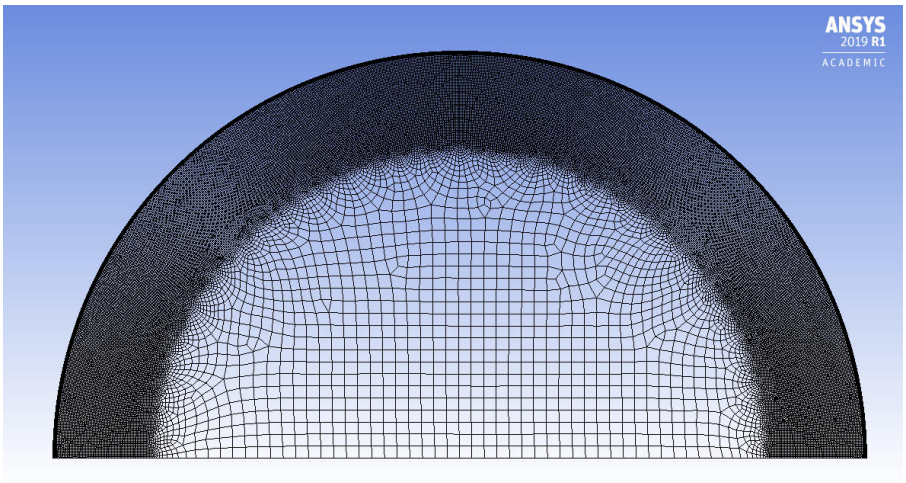


Figure 30: 2D Cross section mesh for the Actuator Disk implementation

2D Testing of the Actuator Disk

The first step is to ensure that the actuator disk actually works in this case. To validate that the 2D cross section analysis will be used as reference. The same domain as the fine mesh of Table 6 is implemented but the sample holder profile is replaced by its equivalent force on a disk and the refinement Zone 2 is therefore not present. Figure 31 shows the velocity comparison between the two cases.

The velocity profiles are very similar. The actuator disk diffuses more than the original case but that is normal with a reproduction of the sample holder's effect everywhere on the trajectory. The velocity in the wake of the sample is almost identical for the two. This ensures the validity of the actuator disk model for our case. One more verification is to implement it on a coarser mesh to ensure that the implementation of the force, in the domain, is not mesh dependent. Figure 32 shows the results with the coarse mesh of Table 6. And once again the results are identical.

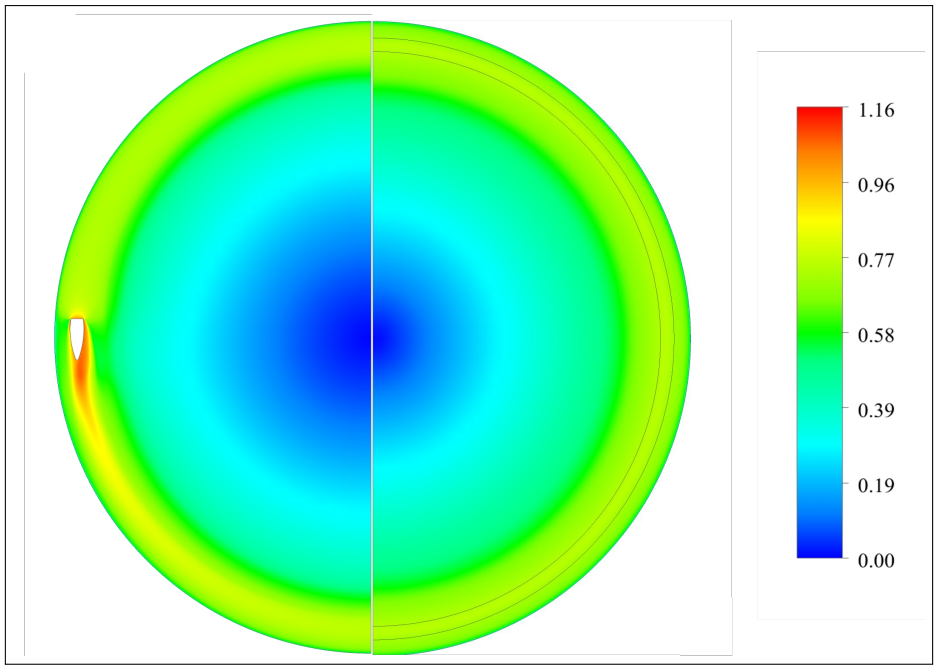


Figure 31: Velocity U/U_∞ comparison between the 2D cross section and the 2D actuator disk

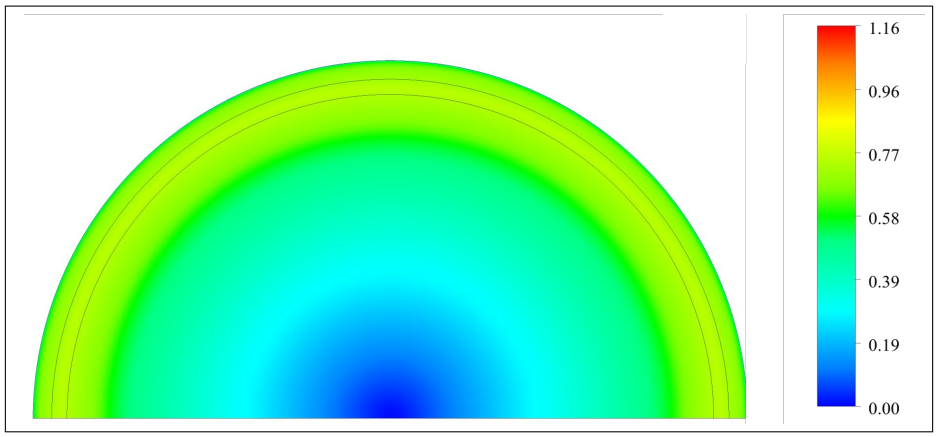
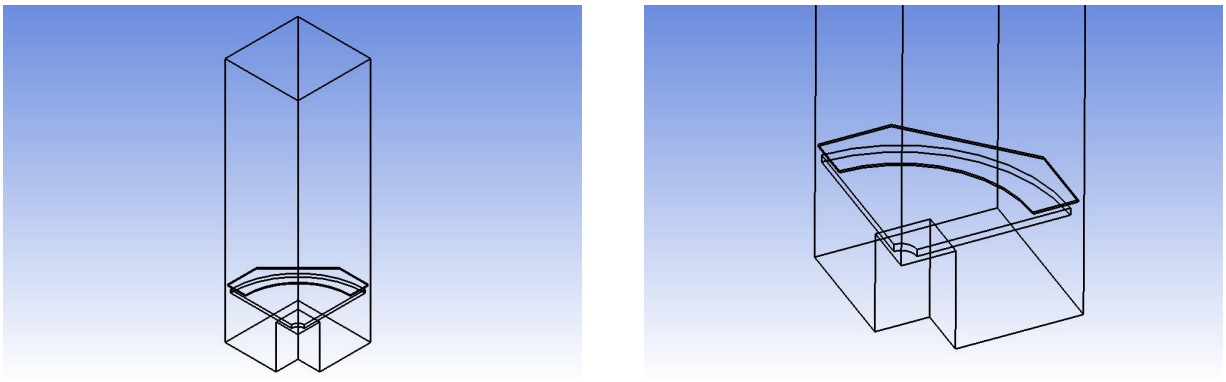


Figure 32: Velocity U/U_∞ of the Actuator Disk on the coarse mesh

3D Actuator Disk



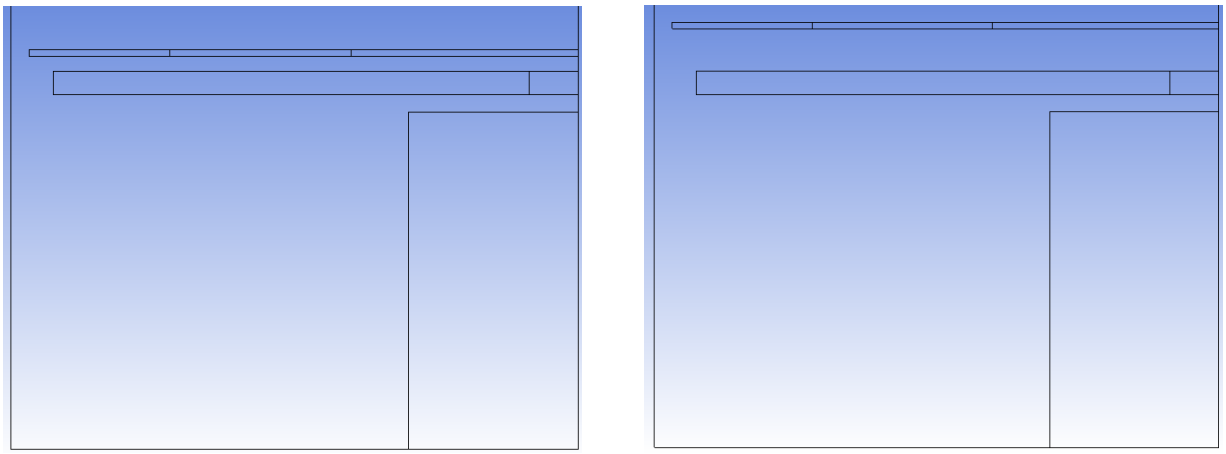
(a) Complete Domain

(b) Zoom on the actuator disk and support

Figure 33: 3D Actuator disk domain

As the actuator disk proved it was accurate for the 2D model of this case, it will be implemented in a 3D representation of the erosion test bench. Since the room is squared, in order to limit the mesh size, it is possible to create a periodic domain of a quarter of the room. This domain is represented in Figure 33. The room is 2.7 meters high and 1.735 meters wide, the sides of the domain will therefore be 86.75 centimeters. The arm is placed on a square table that is 54.5 centimeters high and 52 centimeters wide. To simplify the shape it is assumed to be one solid block. Taking into account the arms mounting points on its support, its center will be located at 56 centimeters from the ground. The actuator disk will therefore be placed at the same height and with a thickness of 3.627 centimeters and a maximal radius of 83.135 centimeters, corresponding to the actual arm dimensions. It will start at 7.5 centimeters from the center to take the hub into account.

An important part of the model is the height at which the support for the water droplet injection mechanism will be placed. Since it can be placed accordingly to the user's demands, it would be too time consuming to simulate every configuration imaginable. A number of assumptions have to be made in order to keep a limited number of simulations. Therefore two configurations will be implemented at first and the need of others will be examined at that point. The first implementation will be the closest possible to the sample holders. With a droplet introduction height of 7 millimeters above the sample holders. The second will be one located at a provisional maximum height of droplet injection of 5 centimeters above the sample holders. The closest configuration has been determined at 7 millimeters in order to allow a small amount of deflection in the arms. However it is unlikely that it will occur. The support of the droplet mechanism will thus be placed at a height of 0.6 meters and 0.643 meters, respectively. Those heights have been calculated to take into account the mounting mechanism of the tubes on the support so that the exits of the droplets are located at the correct injection heights. Those mounting points and tubes are not included in the 3D model to keep the complexity of the domain low. A comparison of the two heights is visible in Figure 34.



(a) Minimum height configuration

(b) Maximum height configuration

Figure 34: Domain comparison between the two support heights

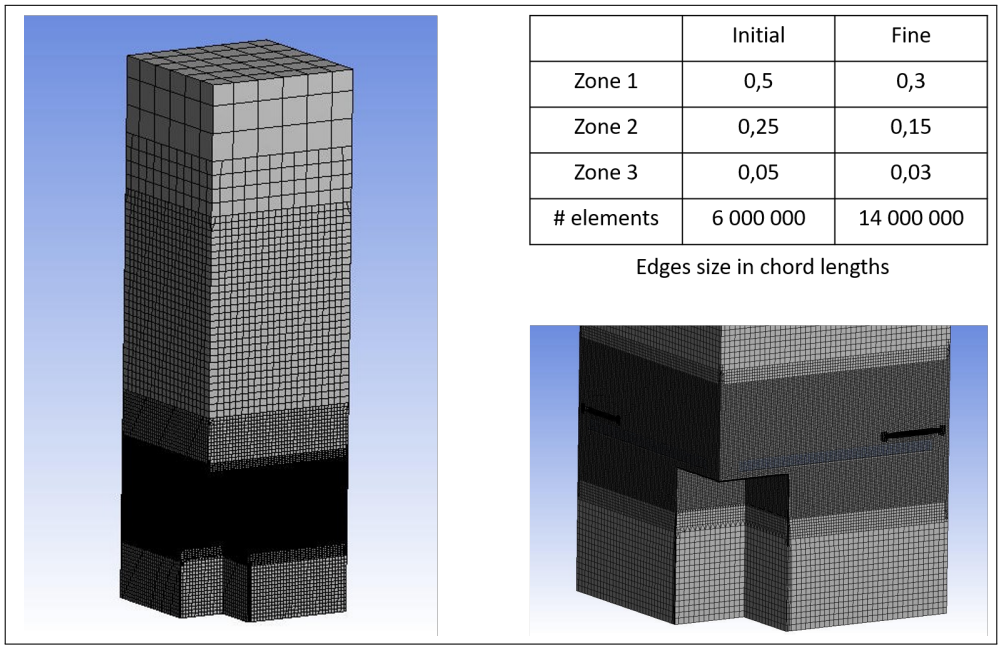
Once again local control zones are used to impose the mesh refinement inside the different areas of the domain. The most refined zone (Zone 3) is centered on the height of the support and is 0.4 meters high. A less refined zone (Zone 2) is held on the part of the domain that is under 1 meter high. The refinement is then coarsened (Zone 1) until 2 meters high, and above that height, it is let to the program default settings to control the size of the domain. The parameters are visible in Figure 35.

As for the boundary conditions all the walls, ground, ceiling, table and support are no slip walls and the periodic conditions applied to the two cutting planes is a zero pressure drop.

In the same way as for the 2D studies, multiple simulations have to be carried on different meshes to compare the results and validate the solution's accuracy. The same validation process is used for the two support heights. In order to lighten the reading only the minimum height validation process will be presented here. The maximum height validation process is presented in Appendix C, but it consists exactly of the same steps and the same data are compared.

The flow field inside the domain can be visualized through its streamlines. Those streamlines are represented in Figure 36 with arrowheads to indicate the direction of the flow. Figure 37 shows the general flow occurring inside the room. Those figures will help in describing the general behaviour of the flow inside the room.

Analyzing those results it can be seen that most of the flow is pulled from the upper side of the room towards the arm and then rejected on the sides of the room. Some of it stays under the arm where vortices are created. As it can be observed, there is not a large amount of vertical circulation involved. It was to be expected since the arms geometry does not aim to create vertical motion of the fluid. What is odd, however, is the very localized velocity, and its large magnitude, at the sample holder's location and the small effect of the arm. This will be investigated later.



	Initial	Fine
Zone 1	0,5	0,3
Zone 2	0,25	0,15
Zone 3	0,05	0,03
# elements	6 000 000	14 000 000

Edges size in chord lengths

Figure 35: Complete information and representation of the 3D actuator disk meshes

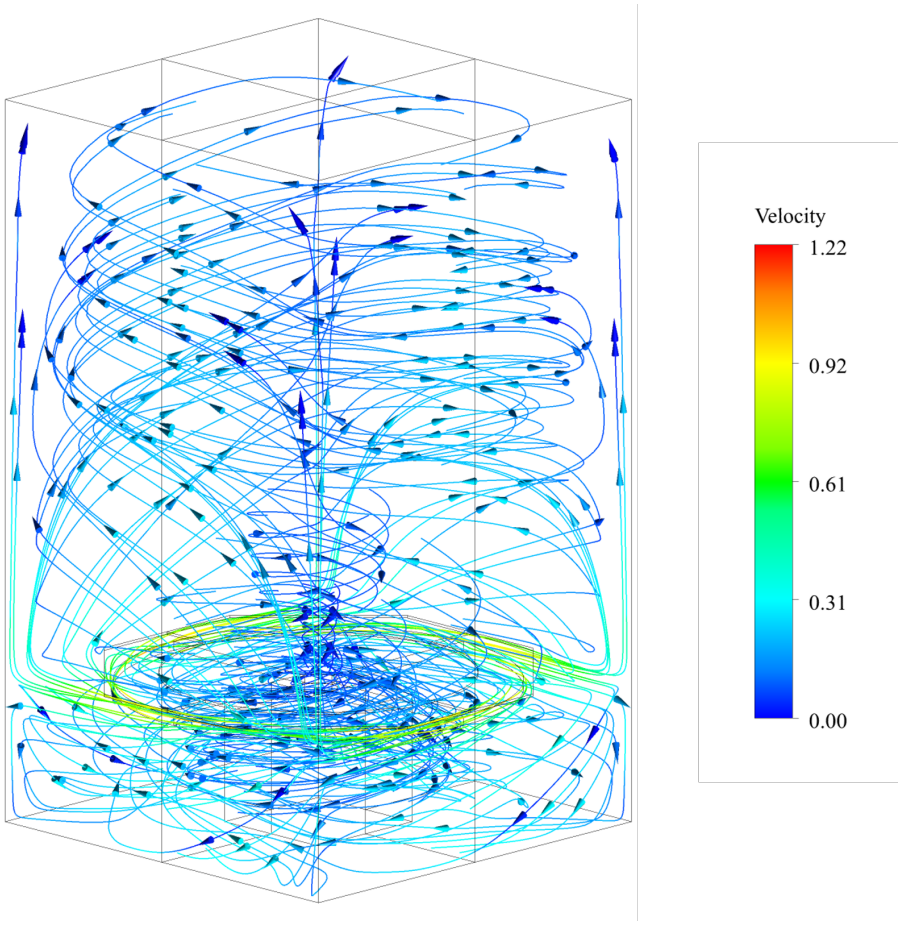
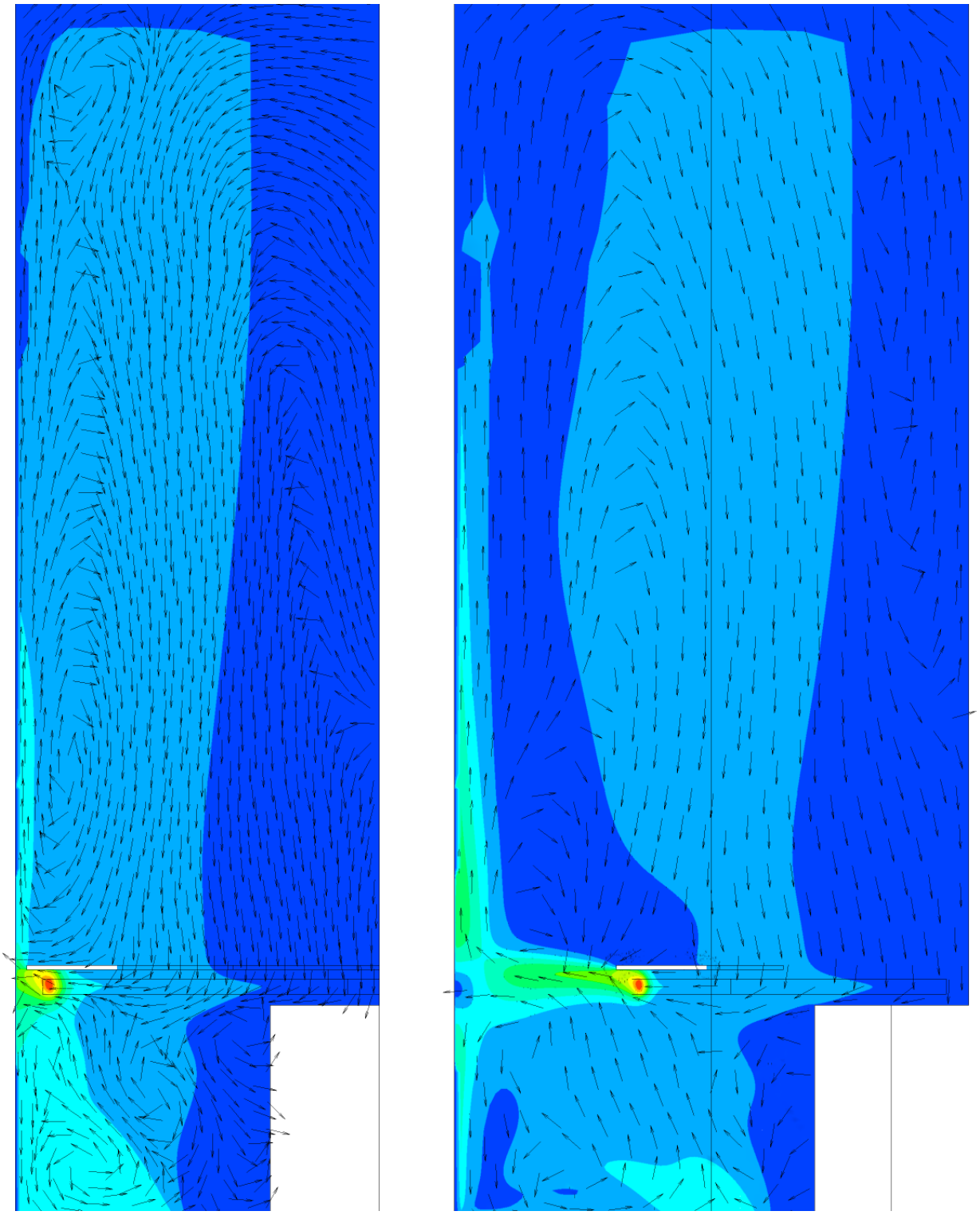


Figure 36: Streamlines visualization of the room color graded for the Velocity U/U_∞



(a) Periodic Boundary

(b) Diagonal of the room

Figure 37: General flow circulation in the room visualization

To validate the results of the simulations the three main components of the velocity, tangential, radial, and vertical will be compared in two different locations.

The first location will be the center of the actuator disk. This will allow a validation of the actuator disk implementation through mesh dependency comparison. The results should be identical since the actuator disk's conditions are imposed by the UDF. They also allow to visualize in what conditions the droplets will evolve in the sample holders area.

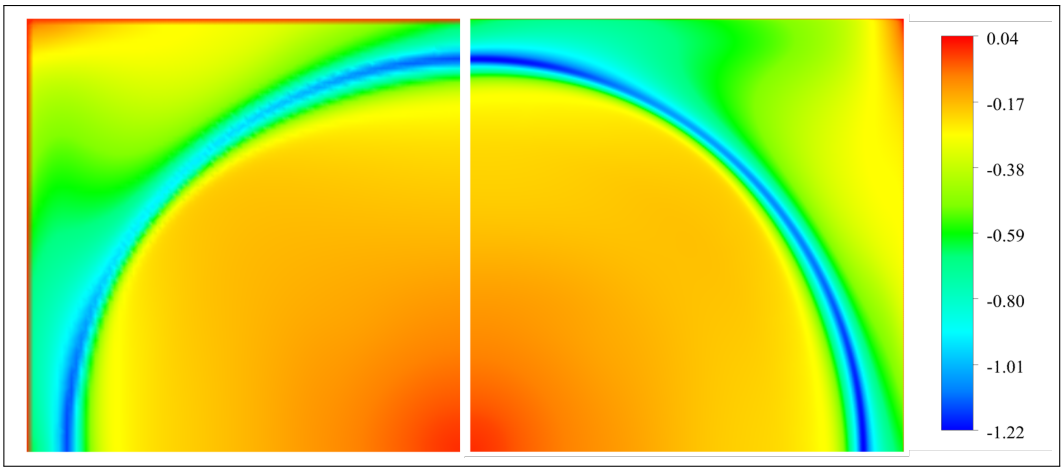
The second location is at the injection height. This is also a crucial point of the droplet's trajectory analysis. It will provide a good comparison point in the region near the actuator disk and also a point of interest for the comparison between the maximum and minimum height configurations.

Figure 38 shows the velocities at the center of the actuator disk. They are presented on the cross section plane in the center of the actuator disk. Viewed from above and disposed as a half-domain representation. The tangential velocity analysis shows a clockwise flow motion due to the actuator disk. The main motion is due to the sample holder. The arm does not seem to have a lot of impact. This may be due to the great difference between the arm and sample holder geometries. Another difference with the 2D analysis is the tangential velocity observed. It is bigger than the ones observed previously. This is likely due to the conversion of the sample holder force, from 2D into 3D that overestimated the force applied by the sample holders. The radial velocity shows that the flow is pushed towards the walls but very weakly in comparison with the tangential motion. For the vertical velocity, the circulation in the actuator disk drags the flow down in the center of it and pushes it up in the corners of the room.

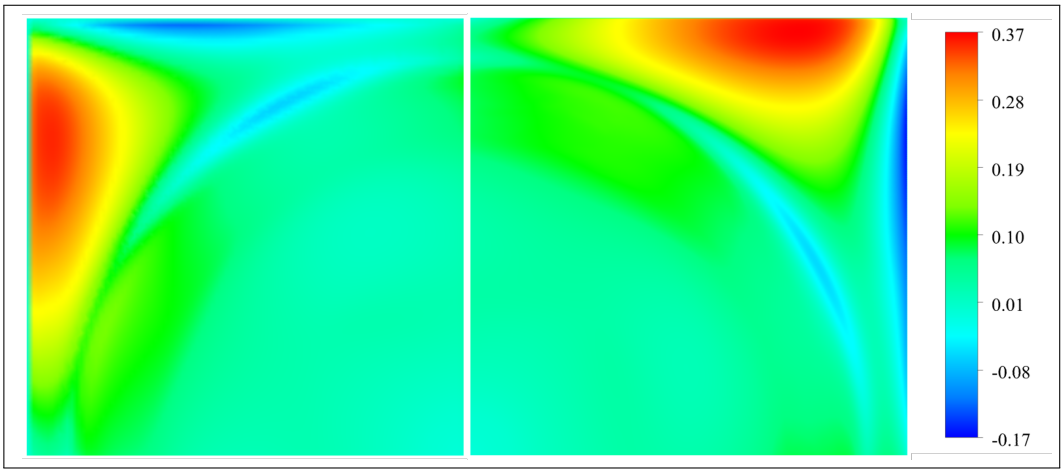
From a comparison point of view, the results are very similar. The finer mesh seems, however, to present a finer definition of the sample holder's velocities. This can clearly be observed in the tangential velocity comparison when the wake's contour is closely examined.

The velocity fields at the droplet injection height are visible in Figure 39. Once again the fields are quite similar to each other. The main difference is that the finer mesh seems to diffuse less. The high positive radial velocity zone is smaller than for the initial mesh. Since the solutions are once again almost identical, it can be concluded that the meshes converge towards an accurate solution.

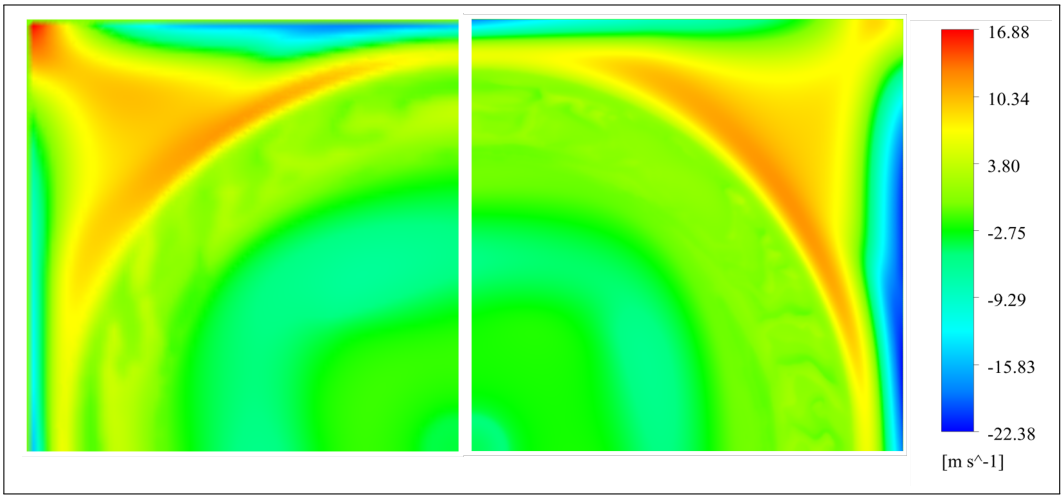
As for the discussion over those results, the vertical velocity confirms that the actuator disk drags the flow down the middle of the room and pushes it back up in the corners. The tangential and radial velocities are in the same order as for the center of the actuator disk. The flow in which the droplets will have to evolve seems to be homogeneous. This encourages the possibility that the droplets will have a stable trajectory.



(a) Tangential Velocity u_t/U_∞

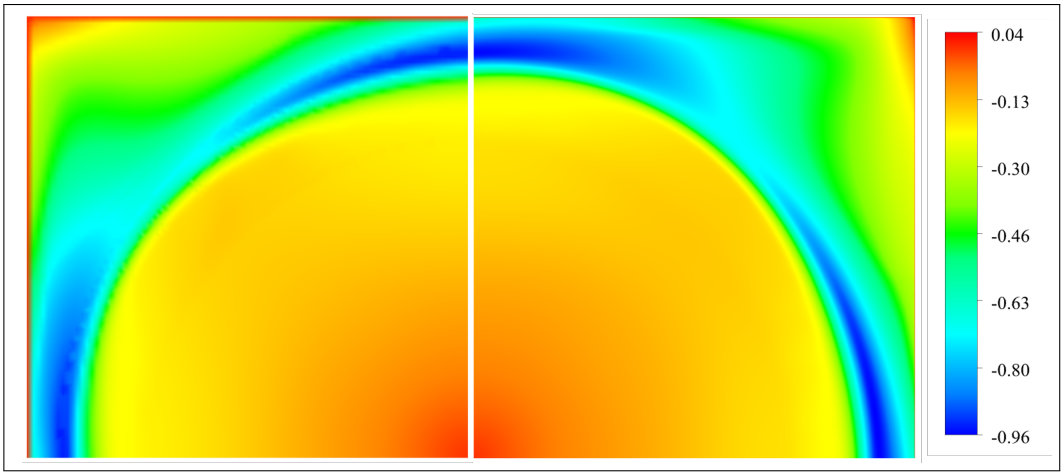


(b) Radial Velocity u_r/U_∞

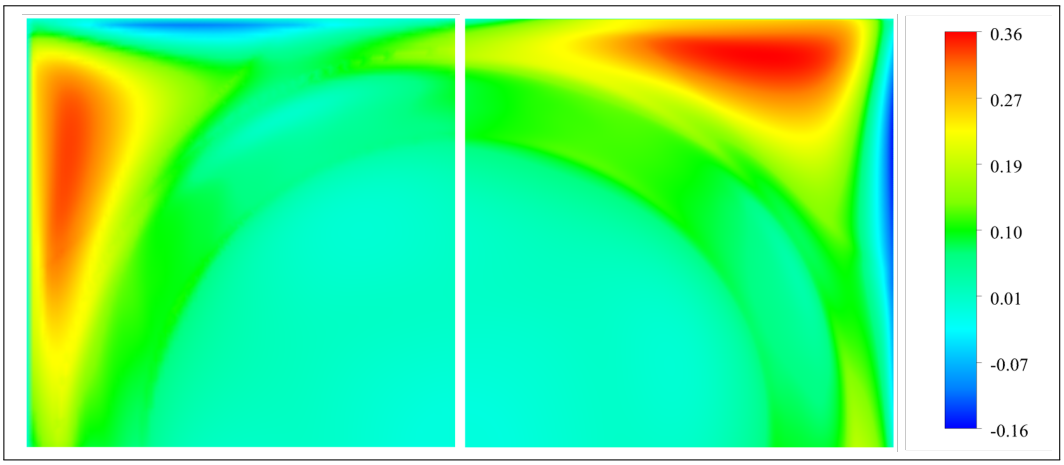


(c) Vertical Velocity u_v

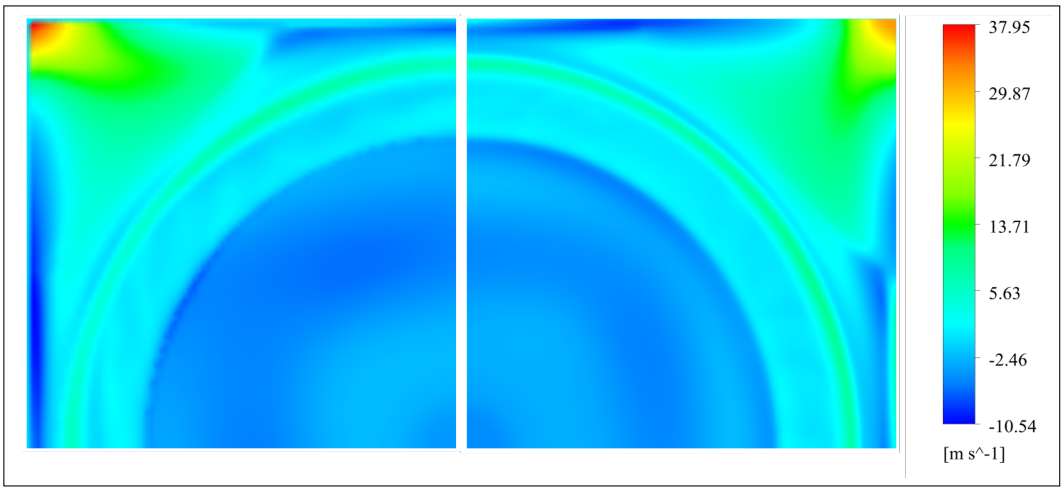
Figure 38: Velocity comparisons at the actuator disk's center. Initial mesh on the left-hand side, Fine mesh on the right-hand side



(a) Tangential Velocity u_t/U_∞



(b) Radial Velocity u_r/U_∞



(c) Vertical Velocity u_v

Figure 39: Velocities comparisons at injection height. Initial mesh on the left-hand side, Fine mesh on the right-hand side

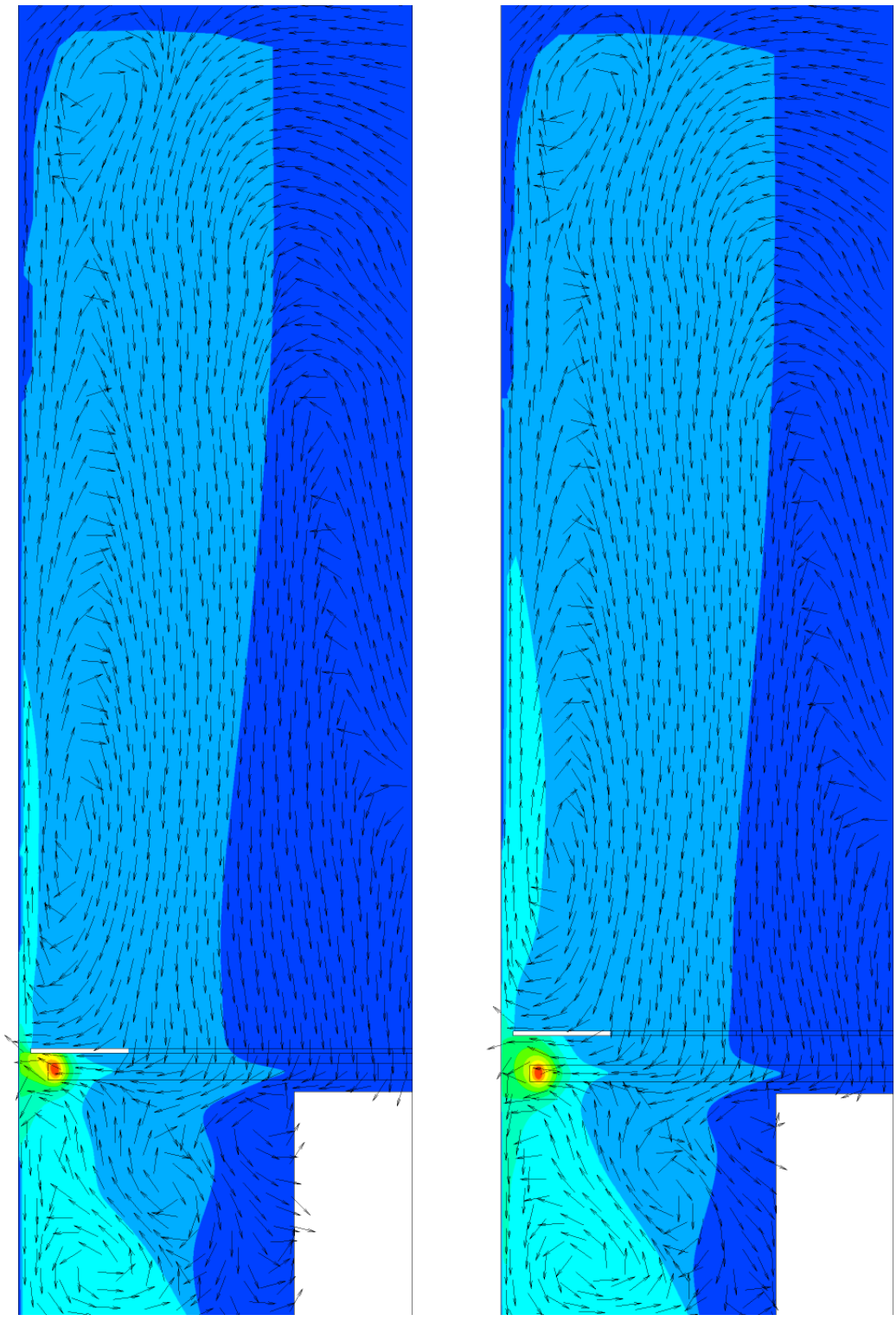
As previously stated the next point of interest is the comparison between the minimum and maximum support height configurations. There are two comparisons that have to be performed.

The general circulation of the flow in the room, and the local difference between the injection mechanism support and the sample holder's trajectories. The general circulation of the room will be compared based on the periodic boundary velocity distribution. Intuition strongly suggests that the general flow will be the same; nevertheless it needs to be verified.

For the local comparison, only the velocity fields on the lowest injection plane will be compared. Since the conditions in the actuator disk are imposed, its center plane is not a relevant point of comparison between the two cases.

If the general and local comparison shows that the two height configurations are close enough to each other this will allow the assumption that the difference with other supports height configurations between the minimum and maximum height are negligible. And thus the injections of the water droplets in the high support configuration will allow a sufficient accurate simulation of all heights in between the lowest configuration and its own. Of course this will have to be confirmed by the later particle trajectory study.

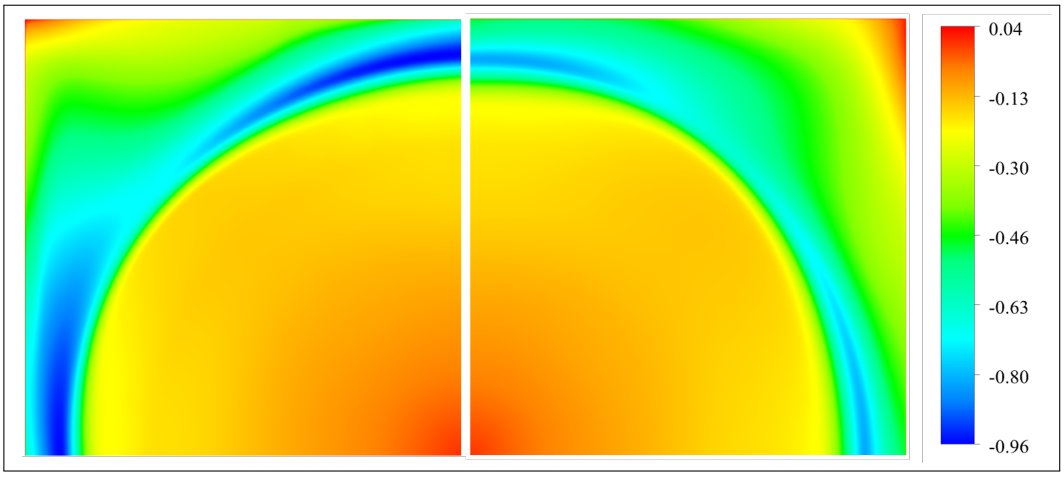
The general flow circulation comparison presented in Figure 40 shows that the two are globally the same, except at the sample holder's position. It is clear that the support confines the wake created by the sample holders. The local comparison will help examine that difference more closely. As shown in Figure 41, the shape of the velocity fields are the same but their intensity varies. The biggest variation is for the tangential velocity in the wake of the sample holders. This is clearly due to the confinement created by the support. In the low configuration, it doesn't allow the wake to grow at its full size as in the higher configuration. This confinement of the flow can either be positive by maintaining the droplet in the sample holder's trajectory or either be negative by accelerating it more and moving it quicker away. Therefore a comparison study between the droplets injected inside both of the cases will be performed. This will inform if the containing of the flow is sufficient enough to affect the trajectory of the droplet or if the position of the support doesn't really affect the trajectory of the droplet at all.



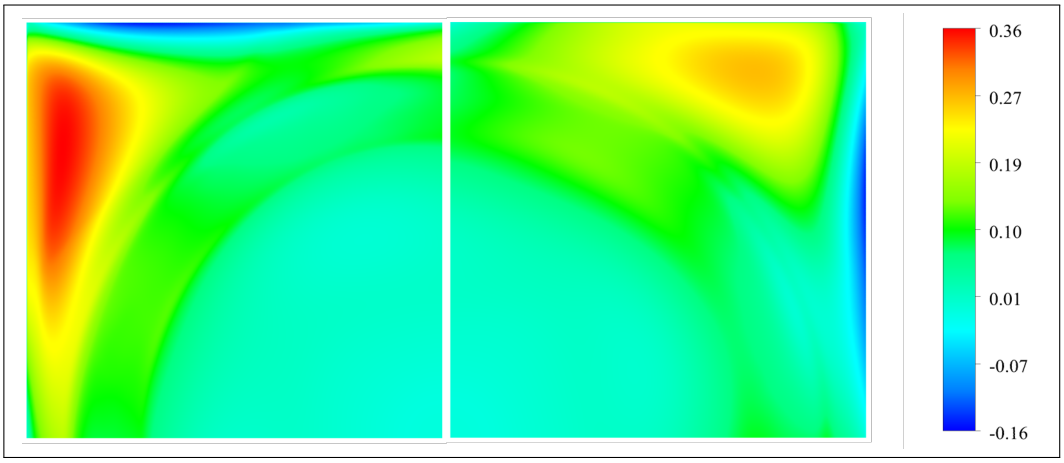
(a) Minimum height configuration

(b) Maximum height configuration

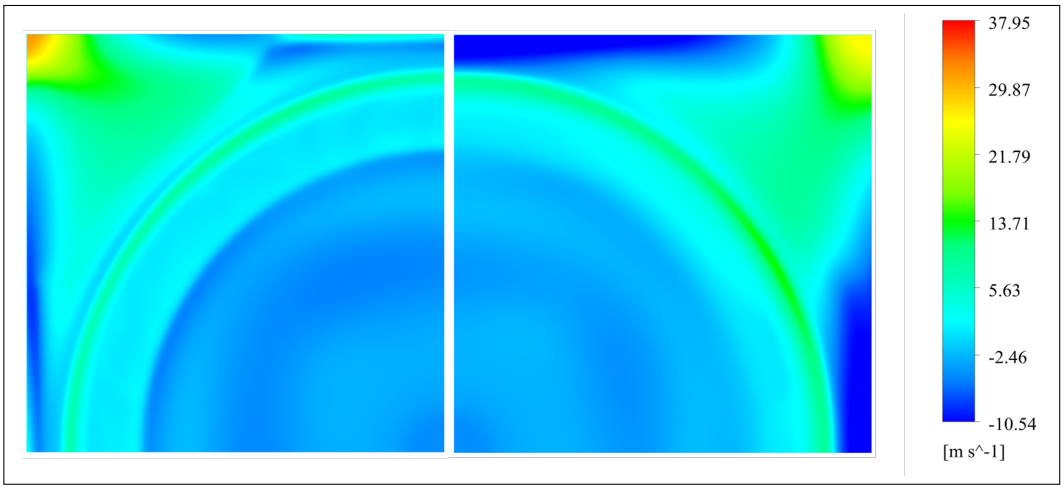
Figure 40: General flow circulation comparison on the periodic boundary



(a) Tangential Velocity u_t/U_∞



(b) Radial Velocity u_r/U_∞



(c) Vertical Velocity u_v

Figure 41: Velocity comparison at injection height. Minimum height on the left-hand side, maximum height on the right-hand side

3.4 Simplified 3D Bench

As the main flow in the room has been simulated the general trajectory of the water droplet can be computed from there. However it will not be enough to only know how the droplets behave in the general flow. Their interaction with the actual arm is really important. Indeed, since the previous simulations does not model the arm, certain local flow behaviours could not be observed. Therefore another domain has to be implemented so that the local behaviour of the flow around the arm can be modeled and the local interaction with the water droplet can be investigated.

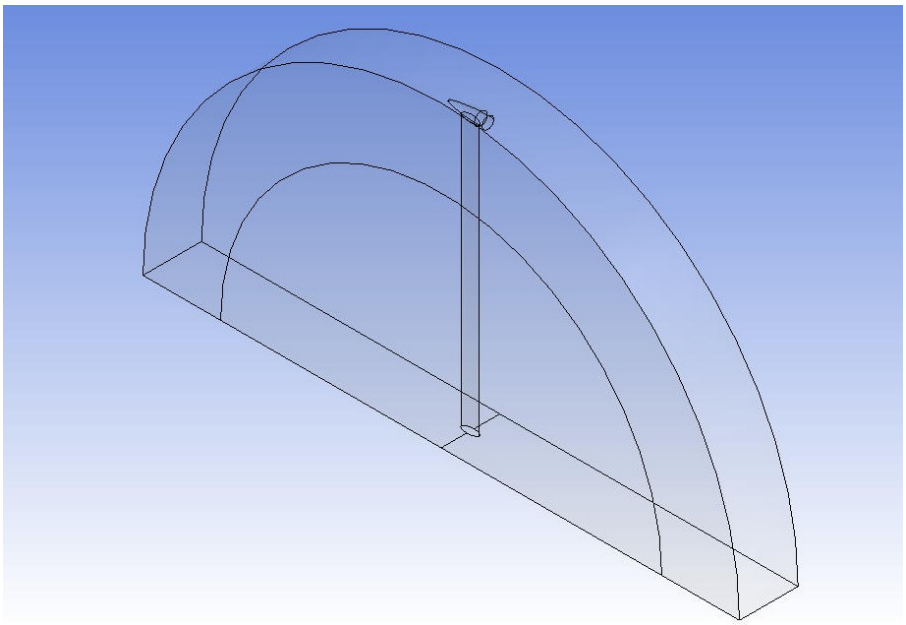
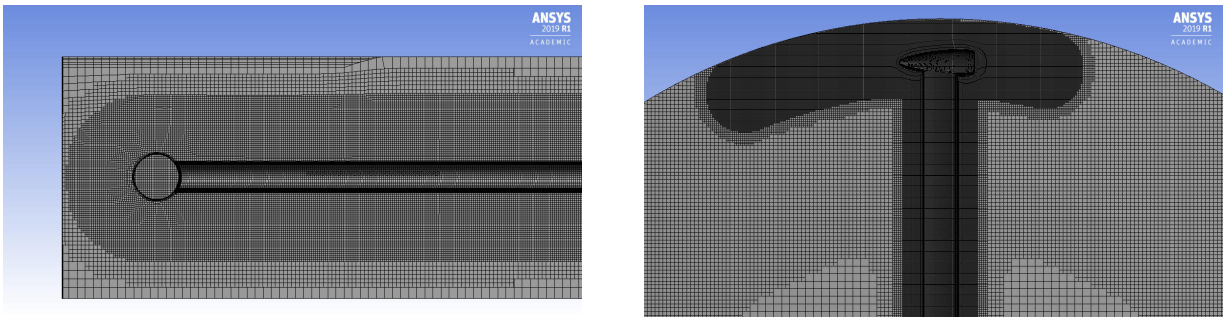


Figure 42: Simplified 3D bench domain

The aim of this simulation is to capture the flow around the rotating arm. This implies simplifications of the general domain. The implemented domain is visible in Figure 42. To ensure an accurate representation in a time-average manner the domain has to be periodic. Since a similar periodic domain was implemented for the 2D cross section, this 3D study will be a simple, 16.6 centimeters high, extrusion of this domain with a complete arm in it. The height of the domain has been determined in order to place an upper wall at the same distance as the maximum support height configuration and have a symmetric height to the center of the arm. The upper boundary will be simplified as a simple circle split into two zones, the outer zone will be a no-slip wall and the inner a free shear wall. The rest of the domain boundaries are free shear walls except for the diameter. This one is split in two to accommodate two periodic boundary conditions that ensures a zero pressure drop between them. Refinements zones are the same as for the 2D cross section domain. The larger one encloses the wake of the sample, and the smaller one will circle the arm with a radius of 0.1 meters. The same refinement as the initial mesh is applied (Table 6). The global mesh is visible in Figure 43.



(a) Vertical cut in the center of the arm

(b) Horizontal cut in the center of the arm

Figure 43: Simplified 3D bench mesh

The velocity results of the horizontal cut in the center of the arm, shown in Figure 44, are comparable to the results of the 2D cross section (Figure 23) but are reasonably differing from the 3D Actuator Disk (Figure 45).

The first difference is with the global drive of the flow by the arm. The explanation of that is likely to be the confinement of the flow. This confinement is happening due to the upper and lower walls of the simplified domain, that aren't present in the complete room. This has the effect to prevent the vertical escape of the flow which could lead to the increased drive from the arm. The other reason could be, as mentioned previously an under estimation of the drag and lift coefficient in the modeling of the actuator disk.

The second difference is the velocity magnitude in the wake of the sample holders. As observed, the velocity in the wake is greater for the actuator disk than for the simplified 3D bench. This was already noted in the actuator disk study. The reasonable explanation is that the conversion of the 2D force calculated on the cross section analysis into a 3D force led to an overestimation of it.

A reasonable way of fixing those problems could be to extract the exact force distribution that the complete arm applies on the flow, from this 3D model. And reiterate the actuator disk model of the room with that distribution implemented instead of the approximation used.

With that in mind, it is still possible to continue to the next step of the study, the introduction of the water droplet.

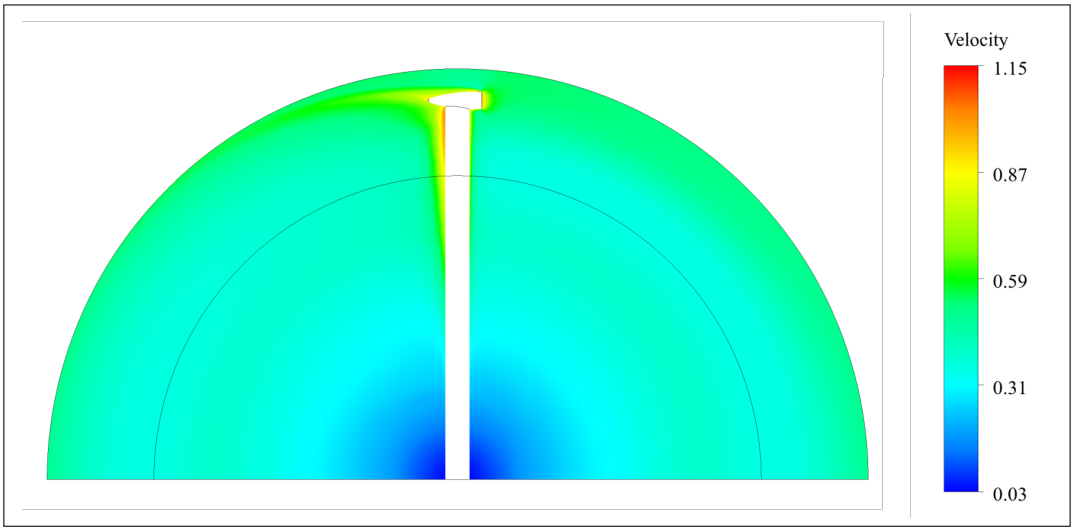


Figure 44: Velocity U/U_∞ in the simplified 3D bench's center

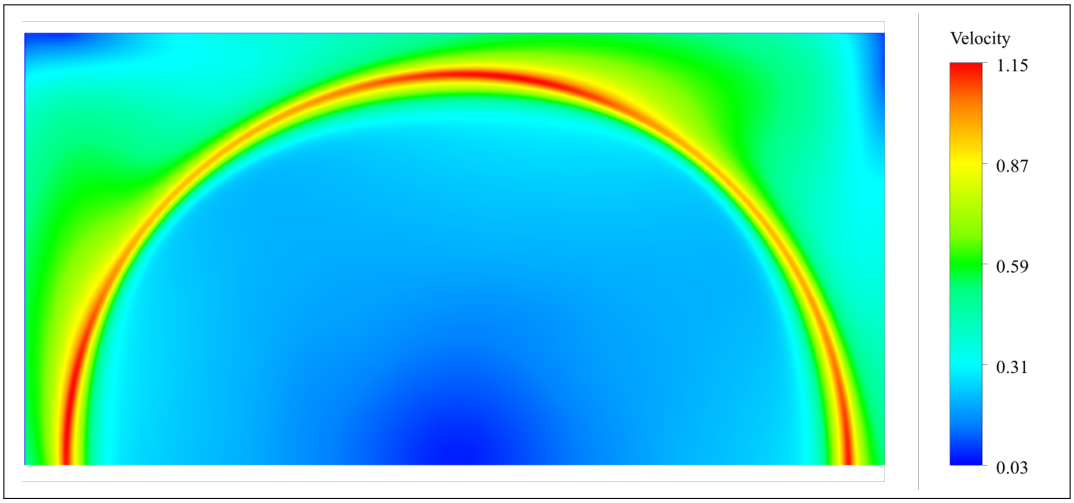


Figure 45: Velocity U/U_∞ in the actuator disk's center

4 Particle Impact Statistics

This section will explain every aspect of the water droplet analysis. First it will go over the principles and hypothesis applied to the study of particles evolving in a flow field. Once the concepts that apply in this case are known, the water droplets trajectories will be computed in the two different support height configurations flow fields. Those trajectories will be compared with the objective to find the optimal one. Once that optimal configuration has been selected, the droplet trajectories that result from that configuration will be injected in the simplified 3D bench to investigate their local behaviour with the arm and sample holder. To conclude this section the pertinent information will be extracted from the different trajectories analyses to provide help for the future erosion study of the sample.

4.1 Implementation Methodology

Since the aim of this study is to compute the interaction of two different fluids, there are two approaches possible for numerical calculation. The Discrete Phase Model (DPM) or the Continuous Phase Model (CPM). The CPM model is used when a large amount of interaction is occurring between different flows or phases of the modeled liquid, differently said, when the volume of the second phase is significant compared to the first. The DPM model is used to track a large number of discrete particles or droplets through a calculated flow field. This is the perfect match for this study.

The implementation of the Discrete Phase Model requires first the calculation of the continuous phase, and then it computes the trajectory of the discrete phase by performing the force balance calculation of the particles. Different forces can be added or neglected depending on the case. In this study the droplets will be considered as inert particles, no mass exchange and no thermal interaction. The used forces will be the ones related to an exchange of momentum (drag, lift, gravity, etc.). The calculation of the resulting force gives the acceleration of the particle. To compute the trajectory a simple implicit trapezoidal discretization scheme is applied. The user can control the time step using one of two parameters. The length scale or the step length factor. In this case a critical length scale will be used so that Fluent automatically adjusts the time step. This ensures that the particle only moves one control volume (in this case a cell of the mesh) at the time. Therefore, the critical length scale will be the same as the minimum length imposed on the mesh edges.

One aspect that will not be treated here is the turbulent dispersion of particles. Indeed, since the flow is turbulent, the trajectory of a droplet could slightly vary depending on the local velocities of the flow. Since the turbulent model used to obtain the flow is a RANS model, those local velocities are averaged and therefore the droplets in this simulation will always follow the same path if they are injected with the same properties. ANSYS Fluent offers two methods to include the local velocities in the DPM simulation. However the aim of this study is to select a number of injection positions that are the most likely to lead to a collision between the sample

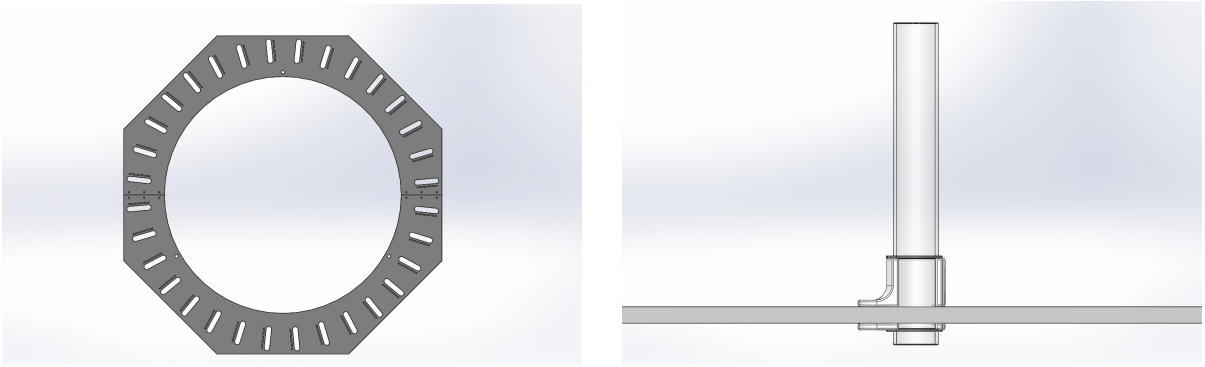
and a droplet. The main path of the particle is by consequence enough to obtain those results.

Another aspect that will not be treated here is the break-up of the droplet. Indeed there is no guarantee that a droplet stays homogeneous and well formed in all situations. The calculation of the break-up phenomena is possible in Fluent only in time dependent simulations and can therefore not be investigated in this case.

4.2 Complete Room Analysis

Now that the integration of the particle model with the flow field is known the study of the droplets can begin. First it's necessary to look at the parameters of the droplets that will be needed to perform the study. The material of the droplet, the injection position and its initial velocity are obvious. The other points that ANSYS Fluent needs are the diameter, mass flow rate and temperature.

Let's first look at where the droplets will be introduced in the room. This will be quite simple since the support plate for the droplet mechanism, shown in Figure 46, has specific slots dedicated to it. They are 32 slots of 10 centimeters long placed radially from an initial radius of 71.25 centimeters. Since the domain is a quarter of the room, there will be 8 slots placed accordingly to the symmetry axes. Each slot will be named by counterclockwise enumeration from 0 to 7. To have a good assumption of where the optimal position to inject a droplet is, 10 droplets will be introduced per slot, each separated by 1 centimeter.



(a) Support Plate (b) Tube and fixing mechanism

Figure 46: CAD model of the droplet injection mechanism

Figure 46 also shows the tube in which the droplet is formed and the fixing mechanism used. There is a minimum distance of 13 millimeters under the support plate that will be occupied by the fixing mechanism and the tube. Therefore the injection points of the droplets will have to take that into account. The height of the tubes is 20 centimeters. The tip of the syringe, which pierces the plug of the tube, is located at 18.5 centimeters from the bottom of the tube. This gives the inlet velocity of the injected particle, the escape velocity of the tube after a free fall of 18.5 cm: $w = -\sqrt{2gh}$. The diameter of the droplets is given by the bench specifications and is 2 millimeters. As for the temperature and mass flow rate, they are not really specified or

controlled but since the calculation is isothermal the same temperature as the room is applied. For the mass flow rate, an injection of one droplet per second will be considered here.

With all that information, the different trajectories can be calculated and the optimal one selected. The first implementation will be carried out with the closest support placement since logic wants that it will have the biggest chance to hit the sample. Then a comparison will be made with the maximum height configuration. This comparison assumes that the distance between the lower limit of the support, and the end of the tube is no longer 13 millimeters but 5 centimeters. This is possible since the supports allow the tube to be mounted with any height configuration. Finally, a comparison study, with height increments of 1 centimeter, will be carried out on the maximum configuration in order to find an optimal injection height.

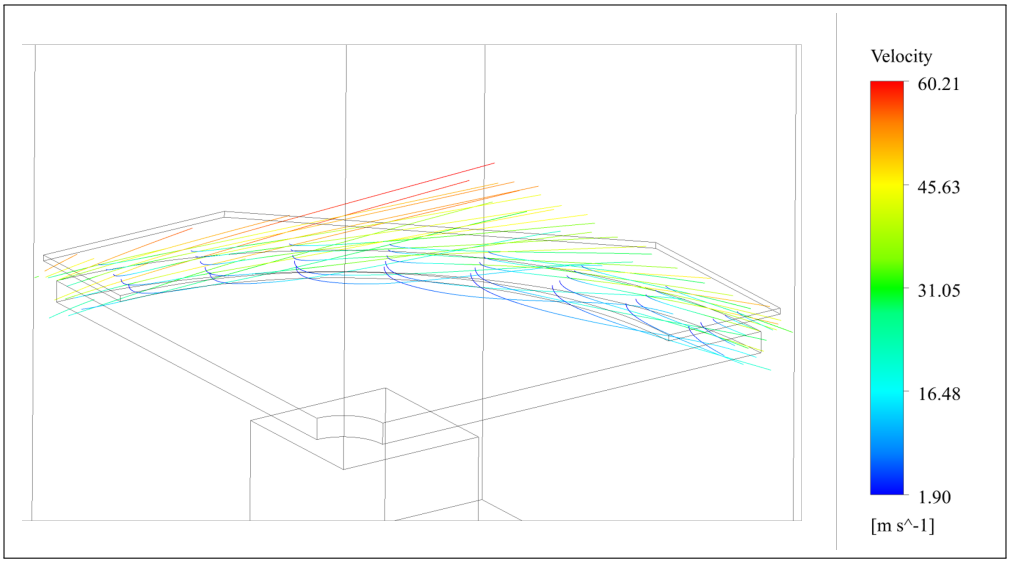
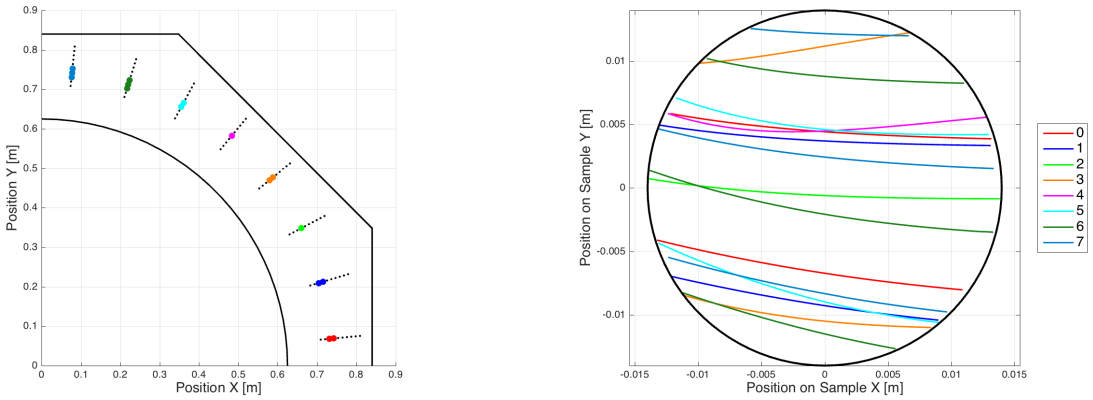


Figure 47: Water droplet trajectories with their velocity magnitude, in the minimum height configuration

Figure 47 shows all the particles trajectories in the domain with the low configuration. A Matlab code was implemented to determine which of them intersect the sample trajectory. The ones that do are colored in Figure 48(a) and their intersecting trajectory with the sample is shown in Figure 48(b).

As it can be seen, 16 different injection locations lead to an intersection with the sample trajectory. From comparing Figure 48(a) and 48(b) it is clear that the droplets are expelled from the center towards the wall and will cross the sample's path at different heights but with similar trajectories.

Figures 49 shows all the different droplet injection locations that will lead to the droplet intersecting the sample trajectory at all the different injection heights implemented. By examining it, it's obvious that, the smaller the height difference between the sample holder and the end of the tube is, the more likely it is that a droplet will intersect the sample's trajectory. A comparison between the intersecting injections on Figure 49(a) and those of Figure 48(a) shows that there are actually more injection positions intersecting the sample when the support is



(a) Injection Locations

(b) Intersecting Trajectories projected on the sample

Figure 48: Intersecting water droplets with the sample in the minimum height configuration

further away from the sample. This is obviously due to the lesser concentration of the flow since the support is further away.

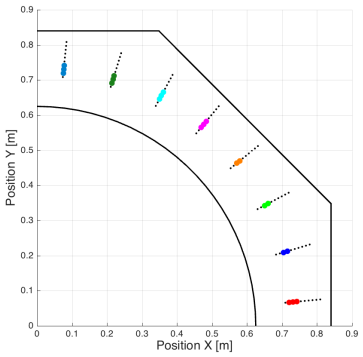
As previously stated more droplets will intersect the sample's trajectory if they are injected more closely to the sample. Therefore some support heights can already be eliminated from further analysis since their likelihood of success is not high enough. All support heights that exceed 3.5 centimeters of separation with the sample holders will be considered irrelevant for the rest of the study. A closer look at the differences between the kept positions and it is clear that the 3 cm and 3.5 cm support heights are almost identical. The 2 cm is evenly placed between the 7 mm and 3.5 cm injection. So an easy choice for further investigation will be the two extremes and the center ones. Hence further investigation of the 7 mm, 2 cm and 3.5 cm injection separation heights will be carried out.

Paying closer attention to the droplets trajectories is essential to understand more about the probability of hitting the sample. For now, the injection locations that will result in the droplet intersecting the sample's trajectory are known but it's possible to go further and to know more about the droplet's probability to hit the sample. This is achieved by comparing the time that the droplet stays on the sample's trajectory to the revolution period of the sample. As shown in Table 8, the maximum time that an injected droplet will stay on the sample's trajectory is almost a quarter of the period. This is very useful for further analysis.

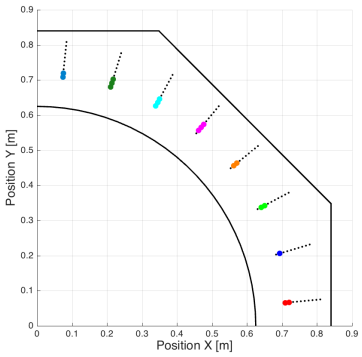
There are two conclusions that can be drawn from this. First, for the local analysis an introduction further than 90 degrees before the sample will be useless since it will not stay long enough on the trajectory to hit the sample. Second, after verification of the local analysis, the hitting probability of a droplet for each injection point can be calculated from this data.

Particle	LC	HC 7mm	HC 2cm	HC 3.5cm
1	0.115	0.084	0.103	0.087
2	0.122	0.114	0.102	0.108
3	0.098	0.069	0.115	0.040
4	0.121	0.112	0.092	0.124
5	0.136	0.083	0.071	0.198
6	0.133	0.121	0.160	0.179
7	0.117	0.076	0.186	0.221
8	0.225	0.128	0.204	0.177
9	0.180	0.168	0.225	0.160
10	0.200	0.080	0.082	0.094
11	0.109	0.237	0.133	0.103
12	0.173	0.122	0.178	0.060
13	0.134	0.150	0.168	N/A
14	0.117	0.183	0.131	N/A
15	0.142	0.104	0.140	N/A
16	0.070	0.077	0.055	N/A
17	N/A	0.146	0.121	N/A
18	N/A	0.121	0.100	N/A
19	N/A	0.106	N/A	N/A
20	N/A	0.120	N/A	N/A
21	N/A	0.078	N/A	N/A
Maximum	0.225	0.237	0.225	0.221

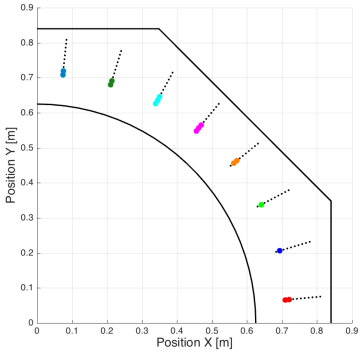
Table 8: Period fraction of the time, a particle, spent on the sample's trajectory for the four analyzed injection height configuration. (LC stands for Low height Configuration and HC for High height Configuration)



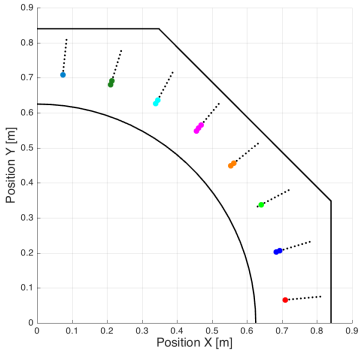
(a) 7 millimeters from the sample



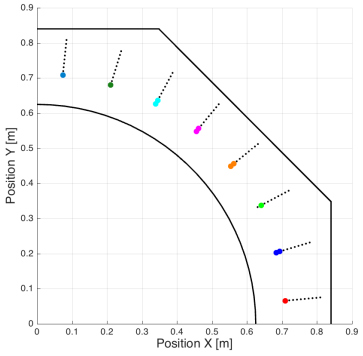
(b) 2 centimeters from the sample



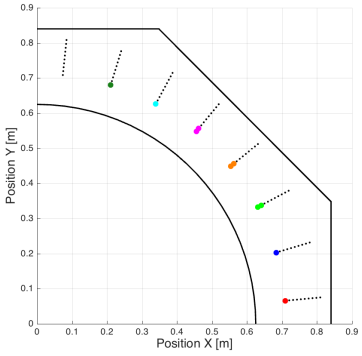
(c) 2.5 centimeters from the sample



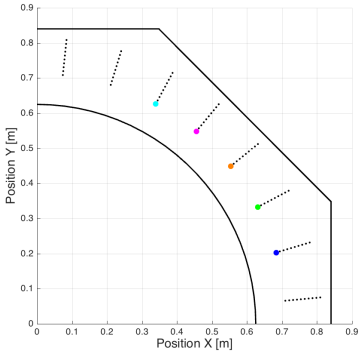
(d) 3 centimeters from the sample



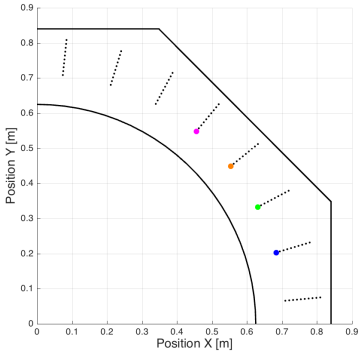
(e) 3.5 centimeters from the sample



(f) 4 centimeters from the sample



(g) 4.5 centimeters from the sample



(h) 5 centimeters from the sample

Figure 49: Injection locations that intersect the sample for all the tested heights

4.3 Local Sample Analysis

The local analysis aim is to determine how the local front perturbation due to the sample holder will affect the incoming water droplets. Another important part is to know exactly in which distances of the sample the droplets will hit it.

To do so all the droplets will be injected on their starting point on the sample trajectory. They will be evenly spaced through the circular trajectory all 5 degrees until a fourth of a period, half of the domain. This has been determined from the maximum time that a particle stays on the sample's trajectory. Their injection velocities will have to be changed from reference frame. Indeed the simplified 3D bench simulation is performed in a local rotating reference frame and the droplet velocities are in the global reference frame. Figure 50 shows different particle trajectories.

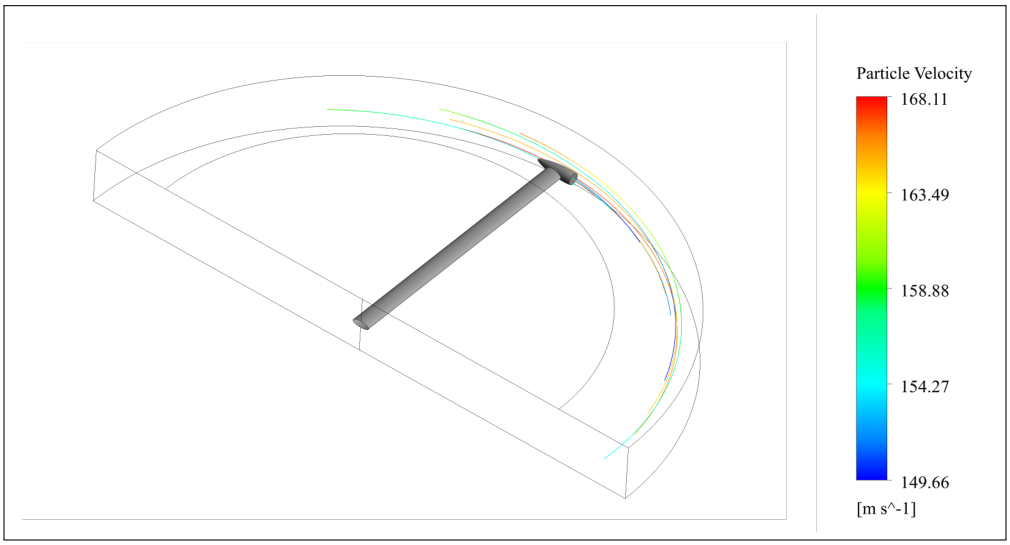


Figure 50: Some droplet trajectories in the simplified 3D bench

Two points can be compared with the complete room analysis.

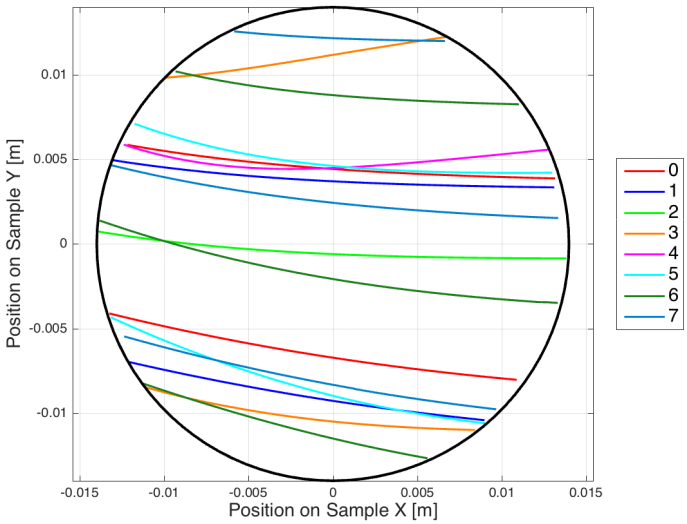
The first one is a confirmation that the maximum amount of time spent by the droplet on the sample trajectory is the same in both simulations. This will be done by finding the maximum angular distance between the sample and a droplet for which the droplet still hits the sample. And then comparing it to the domain size. If the size fraction is the same as the period fraction, previously obtained for that droplet, then there will be no effect of the local sample perturbation on the position and timing in which the droplets have to be injected.

The second point is the trajectory of the droplet on the sample's plane. This will produce an updated location of impact. In comparing the trajectories, the local perturbation can be evaluated as considerable or negligible.

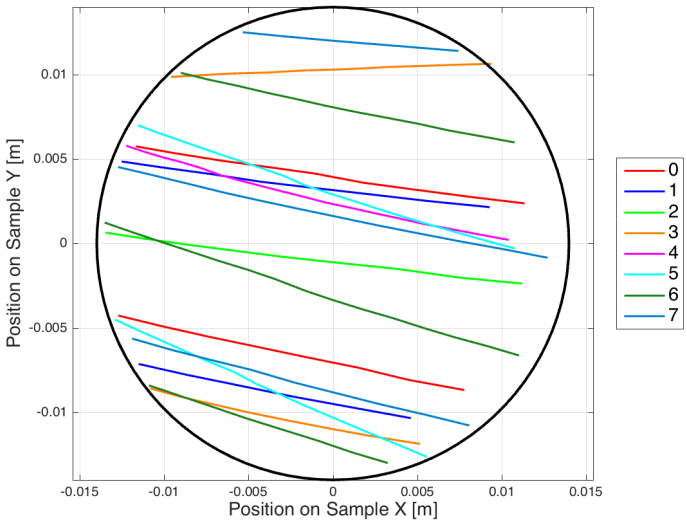
Particle	Complete Room	Simple Bench
1	0.115	0.111
2	0.122	0.125
3	0.098	0.083
4	0.121	0.111
5	0.136	0.125
6	0.133	0.111
7	0.117	0.125
8	0.225	0.250
9	0.180	0.194
10	0.200	0.250
11	0.109	0.111
12	0.173	0.208
13	0.134	0.167
14	0.117	0.125
15	0.142	0.167
16	0.070	0.083

Table 9: Periodic fraction comparison between the complete 3D room and the simplified 3D bench analysis

Upon comparing the period fraction results on Table 9 and the trajectory results on Figure 51. Both results point to a very little difference between the two domains. This has the conclusion that the local perturbation due to the sample holder is not big enough to deviate the droplet's trajectories. Therefore all the injection points intersecting the sample holder's trajectory found during the complete room analysis can be considered as potentially hitting the sample.



(a) Complete Room



(b) Simplified Bench

Figure 51: Intersecting trajectories comparison between the two domains

4.4 Reconciliation

Now that the validity of the different simulations is confirmed it is possible to extract from them the relevant information for the later study of the sample erosion. As mentioned before, only four injection heights will be discussed here. However the complete data are available in Appendix D.

The first point to investigate is the probability to hit a sample with a droplet. For this calculation it will be assumed that the flow rate of droplets is one per second. The corresponding probability of hitting the sample is quite simple to calculate. There is one try per second per injection. There are four injections for each droplet trajectory, since the trajectory was calculated on a fourth of the domain. And the fraction of the trajectory's intersecting time on the sample holder's period is the probability of success. There is one other point to take into account, since there are two sample holders there is no absolute way to know which sample will be hit by the droplet. Therefore the probability of hitting one specific sample will be: $P\left(hit\right) = 4 \times n \times p_f \times \frac{1}{2} = 2 \times p_f$ where, p_f is the period fraction of the intersection between the droplet and sample trajectories, and n is the number of droplets per second. This is expressed in Table 10. The particle id on this table is allocated according to the radial position. The first number corresponds to the slot, from 0 to 7 in the counterclockwise direction. The second number corresponds to the radial position from 0 to 9 in the outwards direction.

As it can be seen, some positions offer a certain advantage over others. But, selected carefully, it is possible to find, on each slot, a position that offers a 25 % chance to hit a specific sample (50% chance to hit one or the other). Table 11 shows the positions in which the injection points should be to maximize the probability of impact and the corresponding probability that at least one impact will occur for this configuration. It is considered here that a maximum of one tube can be mounted per slot. Note that the index number corresponds to the distance in centimeters, from the inner limit of the slot, at which the injection happens.

From a purely probabilistic point of view, the most advantageous configurations should therefore be the lowest support configuration.

The second point that will be investigated is the actual data relevant to the erosion study of the sample. The relevant data for an impact study that can be extracted from the simulations are the relative velocity of the droplet compared to the sample and its angle of impact. Those are presented in Table 12 for the optimal low support configuration. The results of the other configurations are once again available in Appendix D.

Particle ID	LC	HC 7mm	HC 2cm	HC 3.5cm
0	0	0	0.206	0.175
1	0	0.170	0.204	0
2	0.230	0.228	0	0
3	0.244	0.138	0	0
10	0	0	0	0.217
11	0	0	0.230	0.079
12	0.196	0.224	0	0
13	0.242	0.166	0	0
21	0	0	0.185	0.249
22	0	0.242	0.142	0
23	0.272	0.152	0	0
30	0	0	0	0.396
31	0	0	0.320	0.358
32	0	0.256	0.371	0
33	0.266	0.336	0	0
34	0.234	0	0	0
40	0	0	0	0.441
41	0	0	0.408	0.353
42	0	0.160	0.450	0
43	0	0.474	0.165	0
44	0.450	0.244	0	0
50	0	0	0.266	0.320
51	0	0	0	0.188
52	0	0.300	0.355	0
53	0.360	0.368	0	0
54	0.400	0.208	0	0
60	0	0	0.262	0.206
61	0	0.176	0.280	0
62	0.218	0.292	0.111	0
63	0.346	0.242	0	0
64	0.268	0	0	0
70	0	0	0.243	0.120
71	0	0.214	0.201	0
72	0.234	0.241	0	0
73	0.284	0.157	0	0
74	0.140	0	0	0

Table 10: Probability of impact on a specific sample

Slot	0	1	2	3	4	5	6	7	Impact on Sample Probability
LC	3	3	3	3	4	4	3	3	.953
7mm	2	2	3	3	3	3	2	2	.946
2cm	0	1	1	2	2	2	1	0	.939
3.5cm	0	0	0	0	0	0	0	0	.922

Table 11: Tube locations for maximum impact probability

Slot	U_{mag} [m/s]			ϕ [^{o}]		
	Entry	Exit	Average	Entry	Exit	Average
0	153.98	141.34	147.66	88.00	85.64	86.82
1	149.85	137.49	143.65	87.93	85.32	86.63
2	148.09	136.14	142.11	88.12	85.31	86.71
3	151.45	142.37	146.91	88.60	86.91	87.76
4	163.35	141.71	152.53	89.14	87.01	88.08
5	167.28	149.21	158.25	88.99	87.29	88.14
6	165.43	151.48	158.46	88.61	86.88	87.75
7	160.09	146.60	153.35	88.30	86.20	87.25

Table 12: Velocity and Angle of attack of the droplets in the minimum height configuration (LC)

When observing the data of Table 12 two conclusions can be made. The velocity of impact is lower than, the aimed, 180 $[m/s]$. This is due to the increase in velocity of the water droplets caused by the flow. The longer it stays in the flow, the faster the droplet will be. This explains why the relative velocity to the sample is decreasing as the droplet comes to the exit of the sample's trajectory. The angle of impact, on the other hand, stays stable and is very close to the vertical. This is due to the big difference between the sample's velocity and the droplet's velocity. Since there is no definitive way of knowing at which exact point the droplet will impact the sample, the average values are presented for potential use in an erosion model.

In conclusion, the optimal injection height to inject water droplets to impact the sample would be 7 millimeters above it. The chance of at least one impact per second of testing session is 95.3% , if the configuration presented for the low height support in Table 11 is implemented. Doing so the droplets will impact the sample at an average relative velocity magnitude of 150.365 [m/s] with an average impact angle of 87.37 degrees. If testing reveals that configuration to be difficult to implement, all the data relative to the droplets are presented in Appendix D to permit a calculation of impact probability, average velocity, and impact angle for any other configuration.

5 Conclusion

After investigation over the challenges in weight reduction for modern aeronautics, the need for an efficient way of testing the erosion resistance of new composite materials was raised. The UCL is developing a raindrop erosion test bench with the objective of testing those new composite materials. The main challenge of that test bench is the quantification of the erosion rate. To do so, a numerical study of the erosion test bench was put in place. Since the complexity of the problem, a decomposition in smaller problems was performed. This decomposition consists of the gradual modeling of the test bench in increasingly complex geometries. Therefore the first step was determined to be the selection of the appropriate turbulence model, coupled with a basic analysis of a 2D sample holder design. This step would be followed by a simplified 2D analysis of the erosion test bench. After the end of the 2D investigation, the 3D model would be implemented. And finally, the droplet interaction with the erosion test bench would be investigated.

The methodology used to conduct the different investigations was presented and the concepts around it explained. This presentation followed the steps needed in order to solve the problems. The first step was the selection of ANSYS Fluent as software. Then came the discussion over the different meshing options for a domain and how they were used in Fluent. After the mesh, the solvers used by Fluent where discussed and the pressure-based coupled algorithm was selected. The erosion test bench characteristics, as the 2190 rpm of the arms, were then translated into operating and boundary conditions. And finally, a preselection of the relevant turbulence models was done and the $k-\epsilon$ and SST $k-\omega$ models were selected.

After the methodology, the selection of the turbulence model took place on a simple 2D channel implemented around the sample holder's profile. This study showed the weak points of, the $k-\epsilon$ model for a precise near-wall interaction modeling, and the SST $k-\omega$ model for the mesh refinement requirements on 3D domains. The decision was made to use the first one for the 3D domains, and the second one for the 2D domains.

Once the turbulence model was chosen, a simplified 2D cross section of the erosion test bench was studied. This allowed to find out some interactions between the two sample holders and the general velocity of the flow. It also permitted the choice of an initial mesh refinement for the 3D simulations. The information collected on the forces acting on the sample holder also permitted the implementation of the actuator disk needed in the first stage of the 3D study.

After the need for decomposition of the 3D simulations, into two different parts, was expressed, the concept of the first stage, the actuator disk, was presented. After initial testing in 2D, to validate the concept, it was carried out in the room in which the erosion test bench is installed. Two different configurations of the bench where investigated. The first one places the support of the water injection mechanism at the closest of the sample holders, the second one at the furthest. The results of the two configurations were compared and the support was found to contain the size of the wake created by the samples. The second stage is the simula-

tion of the real arm of the test bench. This one was conducted in a confined domain in order to capture the local interaction with the arm and sample holder. The comparison of the two stages raised a question concerning the accurate representation of the arm with the actuator disk model. The flow was more driven by the arm in the local analysis than the complete room, and the velocity magnitude was off. This could be due to the containing of the flow in the local analysis that doesn't happen in the complete room, or by a bad implementation of the arm in the actuator disk model. Ideally, a new complete room simulation should be performed with the force distribution of the real arm implemented inside the actuator disk to be determine the reason behind the flow's behaviour in the complete room.

The next step of the study was to compute the trajectories of water droplets inside the previously calculated 3D flow fields. By performing droplet trajectory analysis with those two stages, the general and local behaviour of the droplet can be analyzed to ensure a good enough prediction of the exact trajectories. To do so, a closer look was taken on the different implementation strategies. The Discrete Phase Model was selected for its efficiency and ease of use. The trajectory analysis was first conducted in the complete room flow fields. This was made in order to know their general behaviour before investigation of the local interaction with the complete arm. This led to the elimination of certain injection positions that wouldn't hit the sample, and the probability of those who could was computed. The promising droplets were then injected inside the local flow field in order to evaluate the importance of the interaction with the real arm. The interaction between the two was concluded to be negligible.

Finally, an optimal position was determined in order to have the best chances of hitting the sample holders. The data relative to the impact parameters of the droplets in that configuration where presented so they could be used in further erosion models investigations.

Furthermore the study should be validated by experimental data, and improvements could be made on the actuator disk by extraction of the simple bench data analysis.

A Validation of the Sample Simplification

As noticed the sample geometry used in this study is not the exact geometry of the real one. The real one is presented in Figure 52. The different geometry is due to the blocking mechanism of the sample. The problem with that geometry is the added computational effort needed to accurately model the effects of that little 'horn'. Since its size, it could have little to no effect on the general behaviour of the flow. A good choice to simplify the computational expense is to eliminate that by the simplification that has been done. But does it have an effect on the local behaviour of the flow? To verify that the removal of the 'horn' does not influence the results of the study, a complementary study of the simplified sample holder geometry compared to the real one was made.

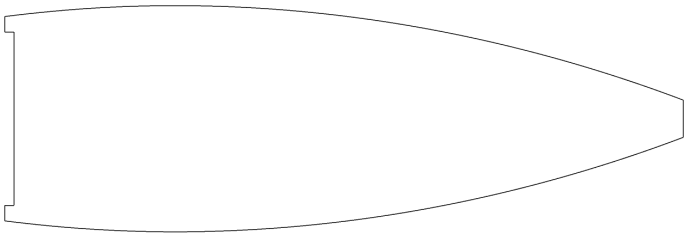
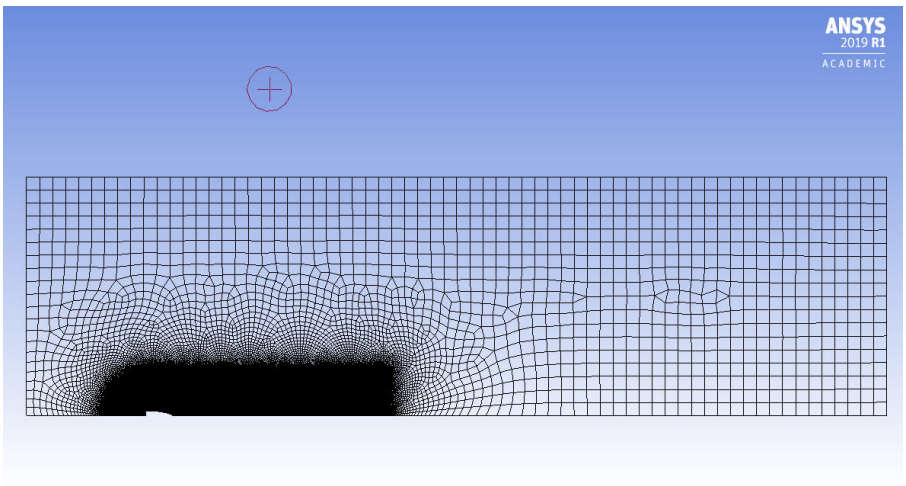


Figure 52: 2D Cut of the real sample holder geometry

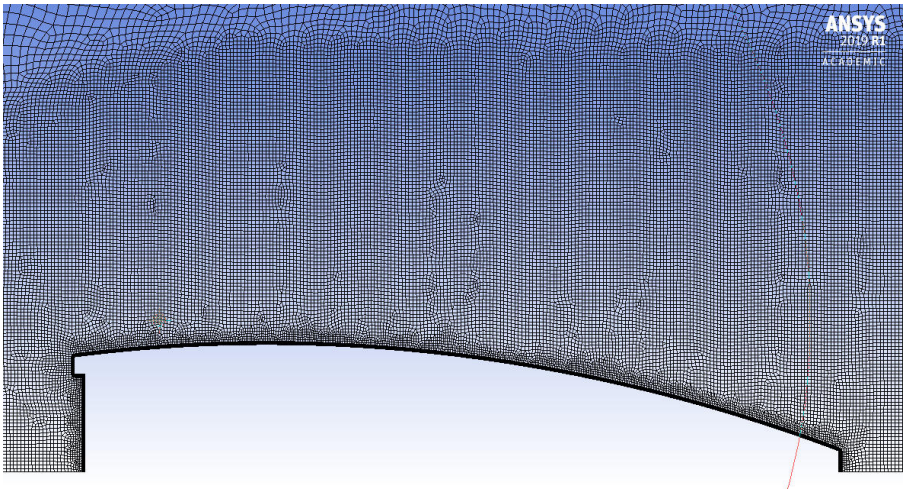
The validation of this will be done by comparing the same data as for the mesh validation and turbulence model. Since the difference between the two cases is the presence of that 'horn', the turbulence model used has to be the optimal one for near-wall modeling. This immediately selects the SST $k-\omega$ model.

The domain will be the same, 33 on 9 chord lengths, 2D channel as for the previous studies on the turbulent model and the mesh section. The boundary conditions will also be the same as for the previous studies. The finest mesh configuration will be implemented in order to model with the most accuracy the possible changes in the flow. And more specifically the changes around the profile.

When Figure 54 is observed, no real difference can be made with the simplified sample holder geometry. For a more efficient comparison, the same tree data as for the previous studies are presented here. For reminder, they are the velocity distribution at one chord distance in front and after the profile, and the size of the circulation bubble in the wake of the profile. Those results are visible in Figures 55 and 56. And what they show is that both of the flows are really similar, this is encouraging for the implementation of the simplified profile. A more rigorous analysis will be the one held on the near-wall treatment.



(a) Complete mesh



(b) Zoom on the sample holder

Figure 53: Fine mesh for the exact sample holder geometry

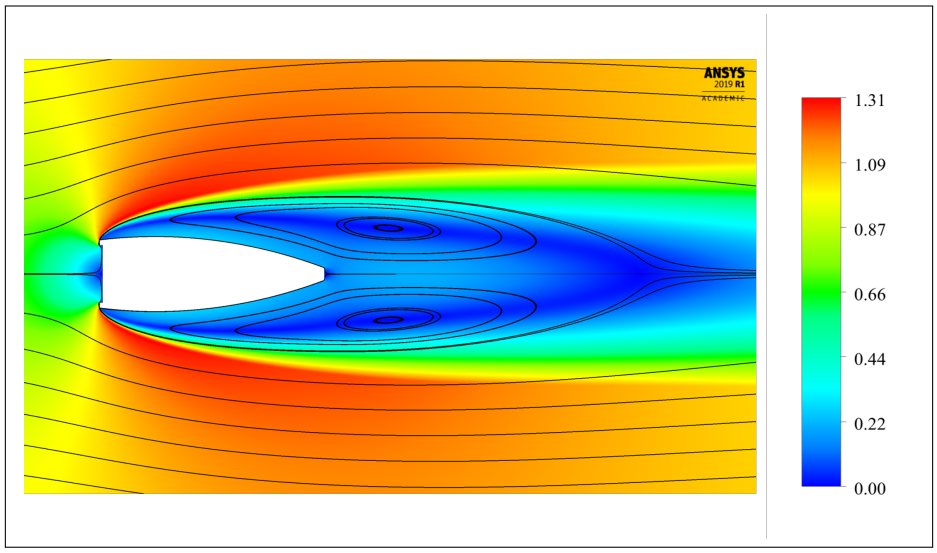
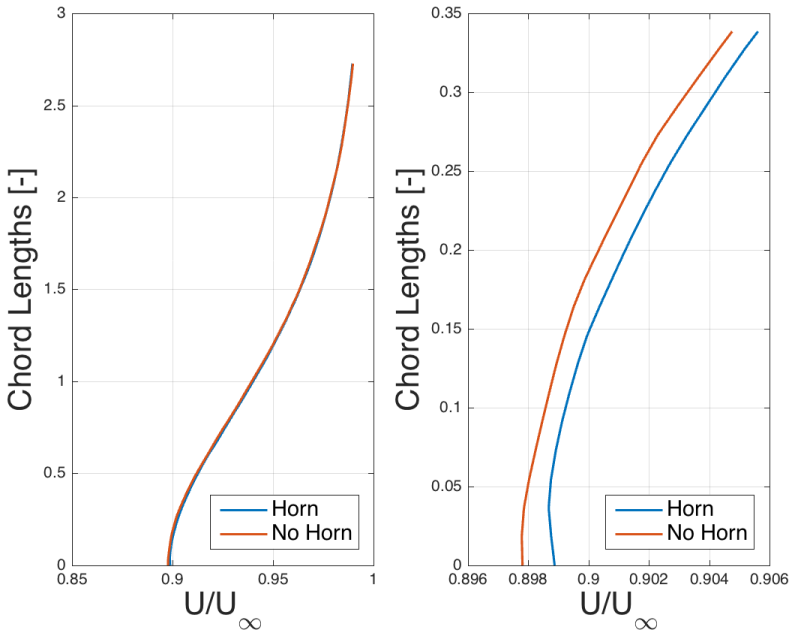
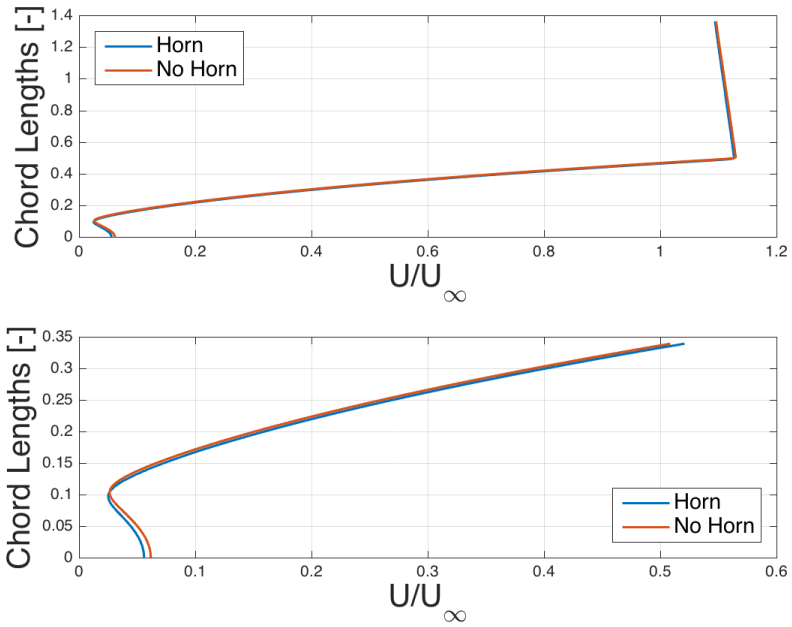


Figure 54: Velocity U/U_∞, with streamlines, on the exact sample holder geometry



(a) 1 chord length in front of the profile



(b) 1 chord length after the profile

Figure 55: Velocity comparison between the two sample holder geometries

To see the real difference a closer look has to be taken on the 'horn's' location (Figure 57). This shows the more complex flow that has to be computed when the exact sample holder geometry is modeled. Looking at the exact geometry, on the left-hand side, the behaviour of the flow is indeed complex. The boundary layer detaches a little bit before the horn in order to pass it. This creates a circulation bubble between the sample's front face and the horn's inner side. Once it has passed the horn, the incoming flow pushes it back on the horn's front face which

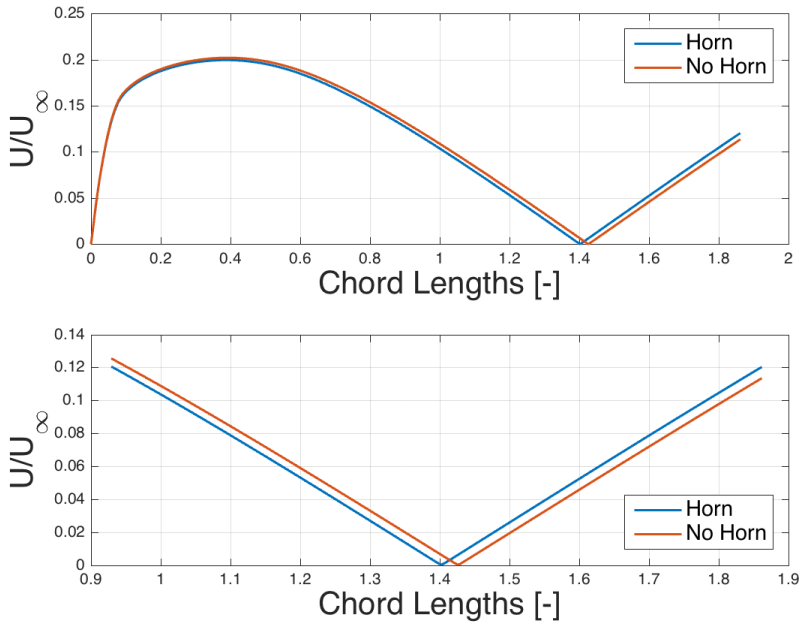
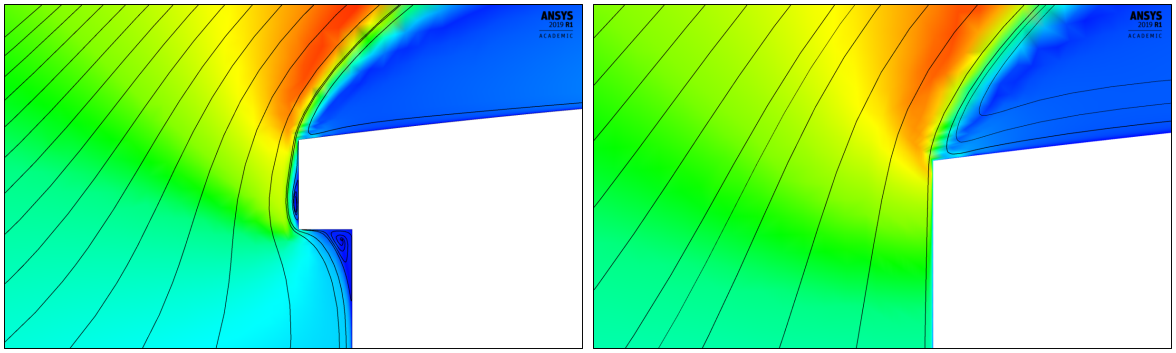


Figure 56: Velocity comparison of the two sample holder geometries on the symmetrical axe after the profile

creates another circulation bubble. The boundary layer has just the time to reattach itself that it is separated at the end of the front face of the horn. In comparison, for the simplified profile the flow just separates at the end of the front face. This is a much simpler flow and involves less calculation from the solver. The need for a comparison between the drag and lift forces of the two geometries becomes obvious. If they are reasonably similar, the simpler geometry can be implemented without loss of information on the general behaviour of the flow, and with a much simpler local flow behaviour.



(a) Exact Sample Holder Geometry (b) Simplified Sample Holder Geometry

Figure 57: Velocity U/U_∞, with streamlines, close up on the sample front

The lift and drag forces on the half profiles are presented in Table 13. Those forces differ from only 2 and 1 % respectively. This is a negligible difference in this study.

	Exact Geometry	Simplified Geometry
Drag [N]	484.86	489.75
Lift [N]	1454.01	1424.83

Table 13: Forces applied on the two different half profile geometries

In conclusion, since the absence of the horn does not modify the general behaviour of the flow, and the computational expense in the near-wall region is simplified without loss of information. The simplified profile can be validated as an alternative to the exact one.

B User Defined Function for the Actuator Disk

```
const double alpha[5][157] = {...};
const double CL[5][157]    = {...};
const double CD[5][157]    = {...};
const double ft = -87.1873;
const double fr = -52.6001;

DEFINE_SOURCE(force_x, cell, thread, dS, eqn){
  double rho_c, theta;
  double fx_c;
  real x[ND_ND];
  C_CENTROID(x, cell, thread);
  rho_c = sqrt(x[0]*x[0] + x[1]*x[1]);
  theta = atan2(x[1],x[0]);
  double r_start = 0.075;
  double r_start_ech = 0.767;
  double r_end = 0.8037;
  double chord = 0.05;
  double omega = -36.5*2*PI;
  double dens = C_R(cell, thread);
  double mu = C_MU_EFF(cell, thread);
  double u = C_U(cell, thread);
  double v = C_V(cell, thread);
  double w = C_W(cell, thread);
  double V_c = C_VOLUME(cell, thread);
  double Re_l = (dens * sqrt(pow((omega*rho_c-u*sin(theta)+v*cos(theta)),2)+pow(
   u*cos(theta)+v*sin(theta),2)+w*w) * chord)/mu;
  int id, length;
  double sigma = 0.005;
  double Gauss = exp(-0.5*pow(((x[2]-0.56)/sigma),2))/sqrt(2*PI)/sigma;
  if (rho_c >= r_start && rho_c < r_start_ech){
    if (Re_l <= 75000){
      id = 3;
      length = 151;
    }
    else if ((Re_l <= 150000) && (Re_l > 75000)){
      id = 0;
      length = 154;
    }
    else if ((Re_l <= 350000) && (Re_l > 150000)){
      id = 2;
      length = 156;
    }
    else if ((Re_l <= 750000) && (Re_l > 350000)){
      id = 4;
      length = 153;
```

```
45      }
46      else if (Re_l > 750000){
47        id = 1;
48        length = 155;
49      }
50      double Fd;
51      double alpha_l = atan2(w,sqrt(pow((omega*rho_c+u*sin(theta)+v*cos(theta)),2)
        ))*180/PI;
52      int count_alpha = 0;
53      double W = pow((omega*rho_c-u*sin(theta)+v*cos(theta)),2)+pow(u*cos(theta)+v
        *sin(theta),2);
54          int i;
55      for( i = 1; i<length;i++){
56        if(alpha[id][i-1] <= alpha_l && alpha_l <= alpha[id][i]){
57          Fd = dens*W/2*(-5)*chord/PI/rho_c;
58          count_alpha++;
59        }
60      }
61      if( count_alpha == 0){
62        if( alpha_l <0){
63          Fd = dens*W/2*-5*chord/PI/rho_c;
64        }
65        if (alpha_l > 0){
66          Fd = dens*W/2*-5*chord/PI/rho_c;
67        }
68      }
69      fx_c = Fd*-sin(theta)*Gauss;
70    }
71    else if(rho_c >= r_start_ech && rho_c <= r_end){
72      double ft_c, fr_c;
73      double Gauss2 = exp(-0.5*pow(((rho_c-0.785)/0.005),2))/sqrt(2*PI)/sigma;
74      ft_c = ft*Gauss2;
75      fr_c = fr*Gauss2;
76      fx_c  =  (fr_c*cos(theta) -  ft_c*sin(theta))*2*36.5;
77    }
78    else{
79      fx_c =0;
80    }
81    return fx_c;
82  }
83
84  DEFINE_SOURCE(force_y, cell, thread, dS, eqn){
85    double rho_c, theta;
86    double ft_c, fr_c;
87    double fy_c;
88    int l = 699;
89    double dft_c, dfr_c;
```

```
90  real x[ND_ND];
91  C_CENTROID(x, cell, thread);
92  rho_c = sqrt(x[0]*x[0] + x[1]*x[1]);
93  theta = atan2(x[1],x[0]);
94  double r_start = 0.075;
95  double r_start_ech = 0.767;
96  double r_end = 0.8037;
97  double chord = 0.05;
98  double omega = -36.5*2*PI;
99  double dens = C_R(cell, thread);
100 double mu = C_MU_EFF(cell, thread);
101 double u = C_U(cell, thread);
102 double v = C_V(cell, thread);
103 double w = C_W(cell, thread);
104 double V_c = C_VOLUME(cell, thread);
105 double Re_l = (dens * sqrt(pow((omega*rho_c-u*sin(theta)+v*cos(theta)),2)+pow(
    u*cos(theta)+v*sin(theta),2)+w*w) * chord)/mu;
106 int id, length;
107 double sigma = 0.005;
108 double Gauss = exp(-0.5*pow(((x[2]-0.56)/sigma),2))/sqrt(2*PI)/sigma;
109 if (rho_c >= r_start && rho_c < r_start_ech){
110   if (Re_l <= 75000){
111     id = 3;
112     length = 151;
113   }
114   else if ((Re_l <= 150000) && (Re_l > 75000)){
115     id = 0;
116     length = 154;
117   }
118   else if ((Re_l <= 350000) && (Re_l > 150000)){
119     id = 2;
120     length = 156;
121   }
122   else if ((Re_l <= 750000) && (Re_l > 350000)){
123     id = 4;
124     length = 153;
125   }
126   else if (Re_l > 750000){
127     id = 1;
128     length = 155;
129   }
130   double Fd;
131   double alpha_l = atan2(w,sqrt(pow((omega*rho_c+u*sin(theta)+v*cos(theta)),2)
    ))*180/PI;
132   int count_alpha = 0;
133   double W = pow((omega*rho_c-u*sin(theta)+v*cos(theta)),2)+pow(u*cos(theta)+v
    *sin(theta),2); //double W = pow((omega*rho_c+u*sin(theta)+v*cos(theta)),2);
```

```
        int i;
    for( i = 1; i<length;i++){
      if(alpha[id][i-1] <= alpha_l && alpha_l <= alpha[id][i]){
        Fd = dens*W/2*(-5)*chord/PI/rho_c;
        count_alpha++;
      }
    }
    if( count_alpha == 0){
      if( alpha_l <0){
        Fd = dens*W/2*(-5)*chord/PI/rho_c;
      }
      if (alpha_l > 0){
        Fd = dens*W/2*(-5)*chord/PI/rho_c;
      }
    }
    fy_c = Fd*cos(theta)*Gauss;
  }
  else if(rho_c >= r_start_ech && rho_c <= r_end){
    double Gauss2 = exp(-0.5*pow(((rho_c-0.785)/0.005),2))/sqrt(2*PI)/sigma;
    ft_c = ft*Gauss2;
    fr_c = fr*Gauss2;
    fy_c = (fr_c*sin(theta) + ft_c*cos(theta))*2*36.5;
  }
  else{
    fy_c =0;
  }
  return fy_c;
}

DEFINE_SOURCE(force_z, cell, thread, dS, eqn){
  double fz_c;
  double dfz_c;
  real x[ND_ND];
  C_CENTROID(x, cell, thread);
  double rho_c = sqrt(x[0]*x[0] + x[1]*x[1]);
  double theta = atan2(x[1],x[0]);
  double chord = 0.05;
  double r_start = 0.075;
  double r_start_ech = 0.767;
  double r_end = 0.8037;
  double omega = -36.5*2*PI;
  double dens = C_R(cell, thread);
  double mu = C_MU_EFF(cell, thread);
  double u = C_U(cell, thread);
  double v = C_V(cell, thread);
  double w = C_W(cell, thread);
  double V_c = C_VOLUME(cell, thread);
```

```
181  double Re_l = (dens * sqrt(pow((omega*rho_c-u*sin(theta)+v*cos(theta)),2)+pow(
      u*cos(theta)+v*sin(theta),2)+w*w) * chord)/mu;
182  int id, length;
183  double sigma = 0.005;
184  double Gauss = exp(-0.5*pow(((x[2]-0.56)/sigma),2))/sqrt(2*PI)/sigma;
185  if (rho_c >= r_start && rho_c < r_start_ech){
186    if (Re_l <= 75000){
187      id = 3;
188      length = 151;
189    }
190    else if ((Re_l <= 150000) && (Re_l > 75000)){
191      id = 0;
192      length = 154;
193
194    }
195    else if ((Re_l <= 350000) && (Re_l > 150000)){
196      id = 2;
197      length = 156;
198    }
199    else if ((Re_l <= 750000) && (Re_l > 350000)){
200      id = 4;
201      length = 153;
202    }
203    else if (Re_l > 750000){
204      id = 1;
205      length = 155;
206    }
207    double Fl;
208    double alpha_l = atan2(w,sqrt(pow((omega*rho_c+u*sin(theta)+v*cos(theta)),2)
     ))*180/PI;
209    int count_alpha = 0;
210    double W = pow((omega*rho_c-u*sin(theta)+v*cos(theta)),2)+pow(u*cos(theta)+v
     *sin(theta),2);
211        int i;
212    for( i = 1; i<length;i++){
213      if(alpha[id][i-1] <= alpha_l && alpha_l <= alpha[id][i]){
214
215        Fl = dens*W/2*-5*chord/PI/rho_c;
216        count_alpha++;
217      }
218    }
219    if( count_alpha == 0){
220      if( alpha_l <0){
221        Fl = dens*W/2*(-5)*chord/PI/rho_c;
222      }
223      if (alpha_l > 0){
224        Fl = dens*W/2*(-5)*chord/PI/rho_c;
```

```
225         }
226       }
227       fz_c = Fl*Gauss;
228     }
229     else{
230       fz_c =0;
231     }
232     return fz_c;
233 }
```

C 3D Actuator Disk Maximum Height Configuration

This appendix will present the validation study performed on the maximum support height configuration of the erosion test bench. The domain was presented in section 3.3.

The flow field inside the domain can be visualized through its streamlines. Those streamlines are represented in Figure 58 with arrowheads to indicate the direction of the flow. Figure 59 shows the general flow occurring inside the room. Those figures will help in describing the general behaviour of the flow inside the room.

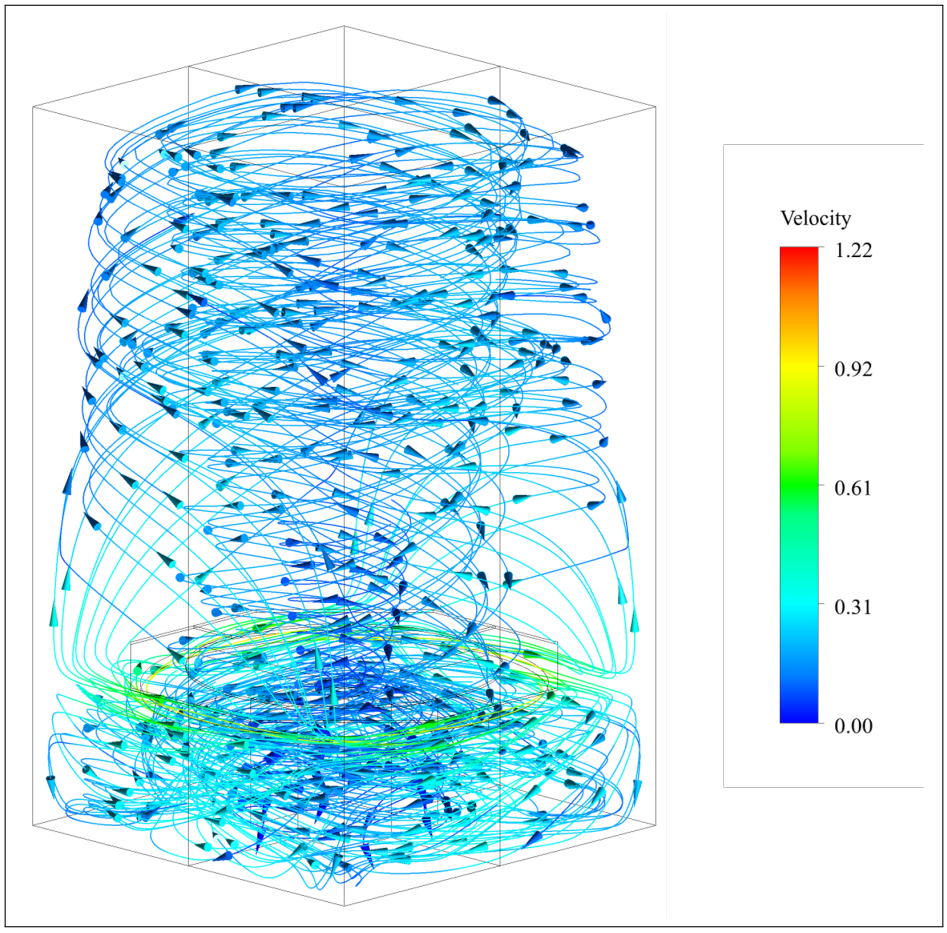
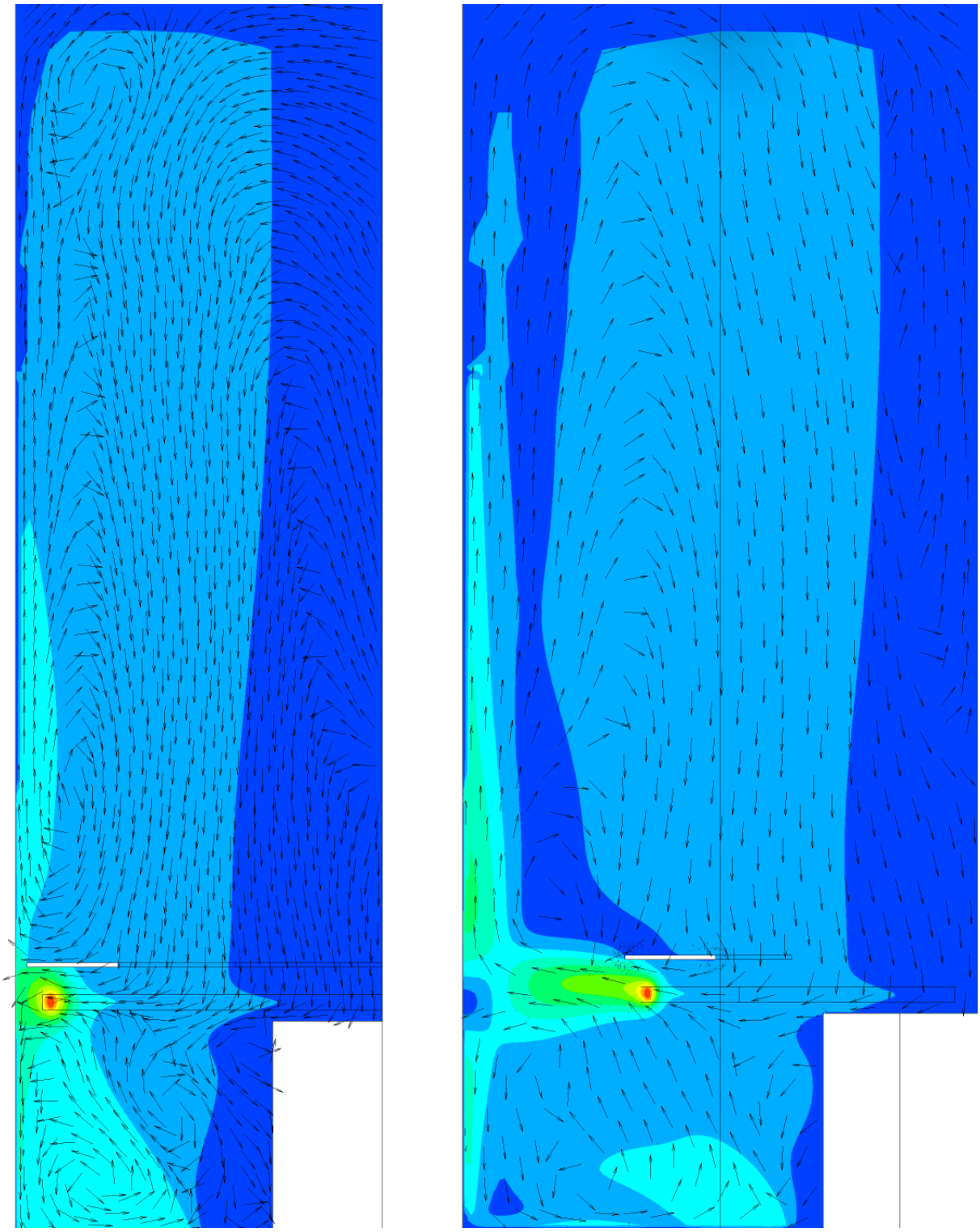


Figure 58: Streamlines visualization of the flow in the maximum height configuration (HC), color graded for the Velocity U/U_∞

As it was expected, the behaviour of the flow is very similar to the low support configuration. Like the low configuration, most of the flow is pulled from the upper side of the room towards the arm and then rejected in the corners of the room. Some of it stays under the arm where vortices are created. As it can be observed, there is not a large amount of vertical circulation involved. It was to be expected since the arms geometry does not aim to create vertical motion of the fluid. Once again the very localized velocity at the sample holder's location and the small effect of the arm are odd.



(a) Periodic Boundary

(b) Diagonal of the room

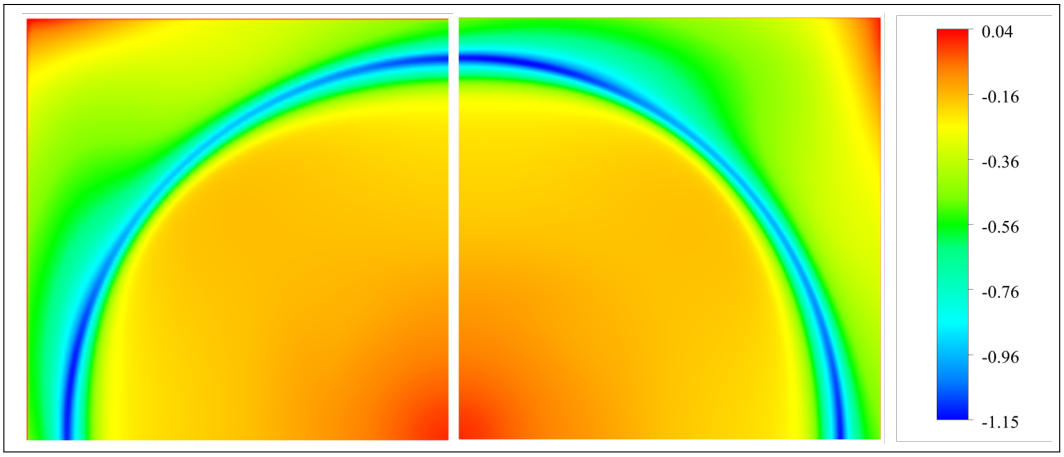
Figure 59: General flow circulation in the room visualization for the HC

As presented for the low configuration, the three main components of the velocity, tangential, radial, and vertical will be compared in two different locations. The first location will be the center of the actuator disk. This will allow a validation of the actuator disk implementation through mesh dependency comparison. The results should be identical since the actuator disk's conditions are imposed by the UDF. They also allow to visualize in what conditions the droplets will evolve in the sample holders area. The second location is at the closest injection height. This is also a crucial point of the droplet's trajectory analysis. It will provide a good comparison point in the region near the actuator disk. And also a point of interest for the comparison between the maximum and minimum height configuration.

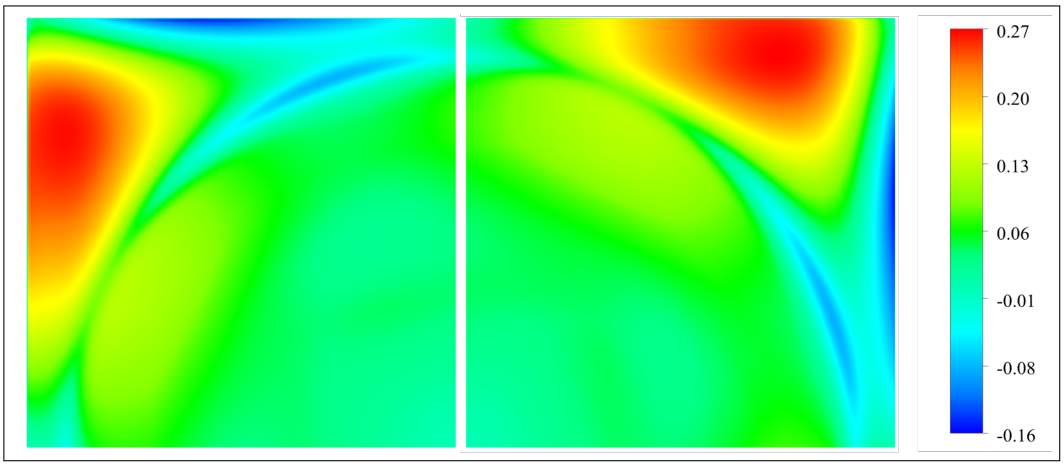
Figure 60 shows the velocities at the center of the actuator disk. They are presented in the cross section plane at the center of the actuator disk. Viewed from above, and disposed as a half-domain representation. The tangential velocity analysis shows a counterclockwise flow motion due to the actuator disk. The same observation as for the low configuration is made. The main motion is due to the sample holder. The arm does not seem to have a lot of impact. This may be due to the great difference between the arm and sample holder geometries. Another difference with the 2D analysis is the tangential velocity observed. It is quite bigger than the one observed previously. This is likely due to the conversion of the sample holder forces from 2D into 3D that overestimated the forces applied by the sample holder. The radial velocity shows that the flow is pushed towards the walls but very weakly in comparison with the tangential motion. For the vertical velocity, the circulation in the actuator disk drags the flow down in the center of it and pushes it up in the corner of the room.

For the comparison between the two meshes, the results are very similar. More so than for the low configuration. The results are almost indistinguishable.

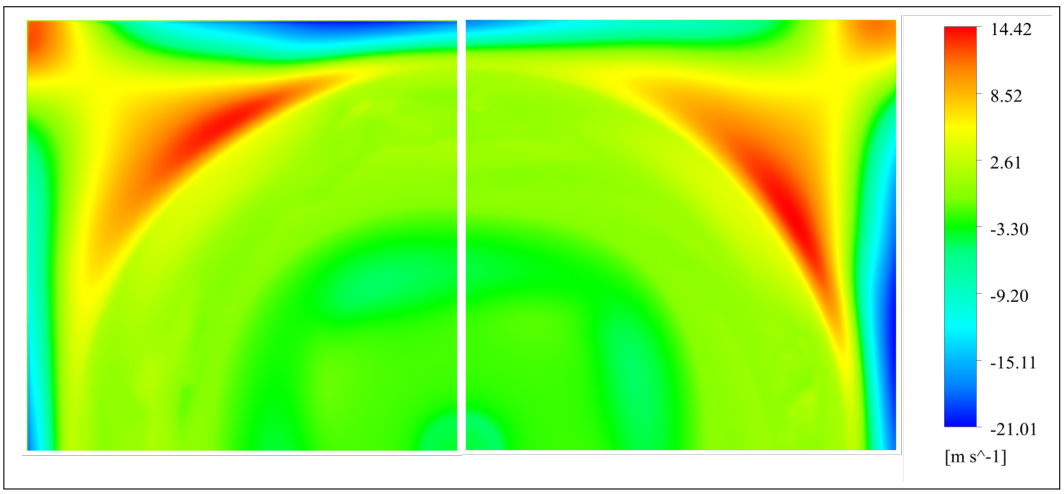
The velocity fields at the lowest droplet injection height are visible in Figure 61. Once again the fields are similar to each other. Since the solutions are once again almost identical, it can be concluded that the meshes converge towards an accurate solution.



(a) Tangential Velocity U_t/U_∞

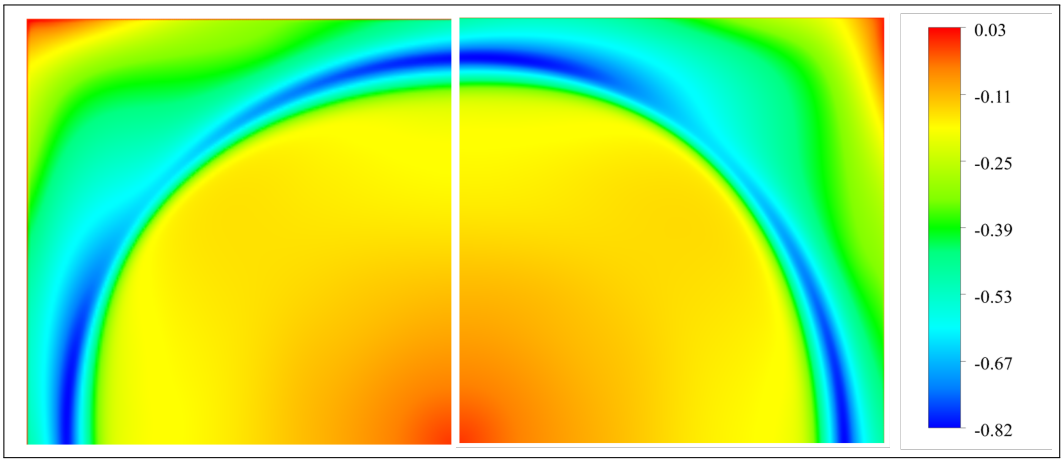


(b) Radial Velocity U_r/U_∞

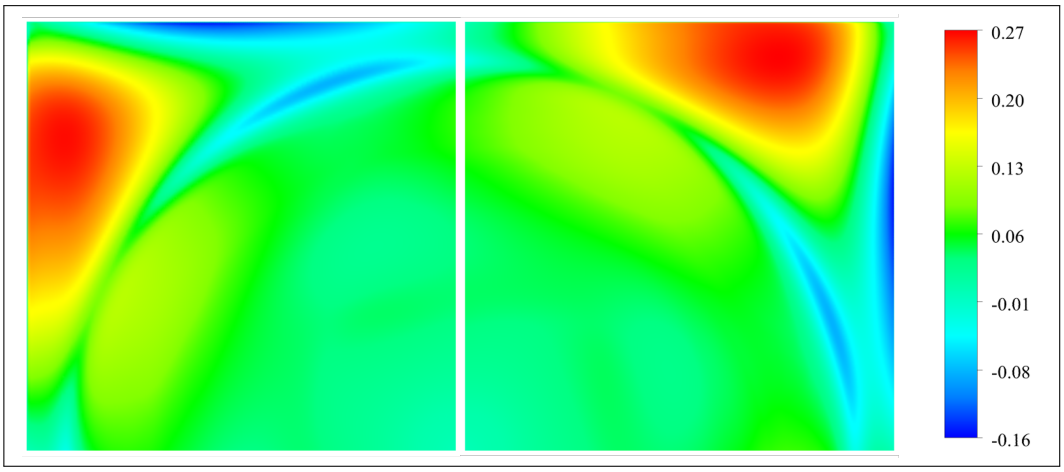


(c) Vertical Velocity U_v

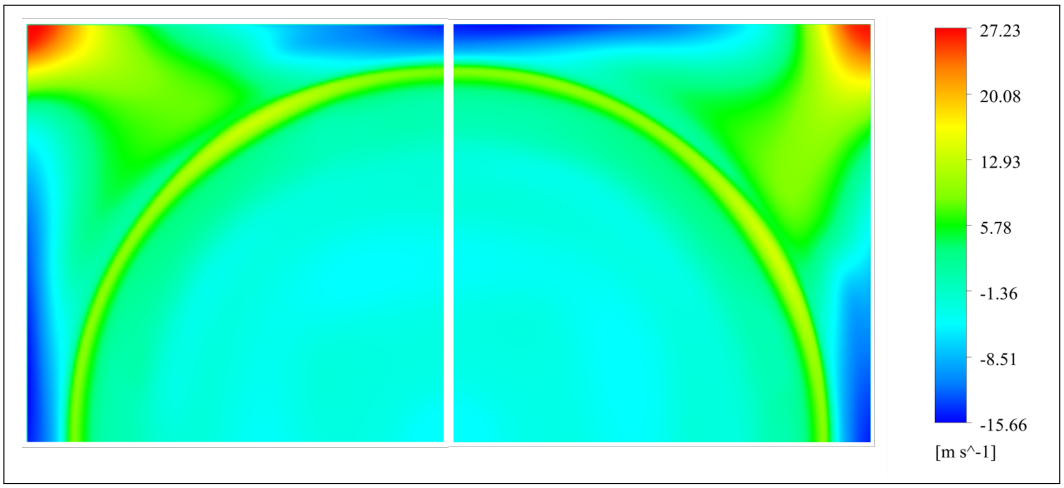
Figure 60: Velocity comparisons at the actuator disk's center. Initial mesh on the left-hand side, fine mesh on the right-hand side



(a) Tangential Velocity u_t/U_∞



(b) Radial Velocity u_r/U_∞



(c) Vertical Velocity u_v

Figure 61: Velocity comparisons at the lowest injection height. Initial mesh on the left-hand side, fine mesh on the right-hand side

D Particle Injection Complete Data Tables

ID	U_{mag} [m/s]			ϕ [^{o}]			Period fraction
	Entry	Exit	Average	Entry	Exit	Average	
2	154.99	145.19	150.09	87.85	86.00	86.93	0.115
3	153.98	141.34	147.66	88.00	85.64	86.82	0.121
12	150.76	142.81	146.78	87.66	85.98	86.82	0.098
13	149.85	137.49	143.67	87.93	85.32	86.63	0.122
23	148.09	136.14	142.12	88.12	85.31	86.72	0.136
33	151.45	142.37	146.91	88.60	86.91	87.76	0.133
34	149.66	136.78	143.22	88.70	86.73	87.72	0.117
44	163.35	141.71	152.53	89.14	87.01	88.08	0.226
53	167.35	154.93	161.14	88.84	87.73	88.29	0.180
54	167.28	149.21	158.24	88.99	87.29	88.14	0.200
62	165.16	158.25	161.70	88.36	87.52	87.94	0.109
63	165.43	151.48	158.45	88.61	86.88	87.75	0.173
64	164.46	151.48	157.97	88.62	87.09	87.86	0.134
72	160.20	151.25	155.73	88.07	86.64	87.36	0.117
73	160.09	146.60	153.35	88.30	86.20	87.25	0.142
74	157.36	149.58	153.47	88.07	86.95	87.51	0.070

Table 14: Velocity and Angle of attack for the LC

ID	U_{mag} [m/s]			ϕ [^{o}]			Period fraction
	Entry	Exit	Average	Entry	Exit	Average	
1	150.94	145.59	148.27	87.25	85.84	86.55	0.085
2	150.09	142.17	146.13	87.54	85.40	86.47	0.114
3	148.15	143.19	145.67	87.42	86.08	86.75	0.069
12	146.59	139.11	142.85	87.49	85.26	86.38	0.112
13	144.90	139.20	142.05	87.43	85.68	86.56	0.083
22	146.81	138.89	142.85	87.95	85.92	86.94	0.121
23	144.19	138.89	141.54	87.75	86.34	87.05	0.076
32	154.10	147.38	150.74	88.64	87.61	88.13	0.128
33	153.10	140.53	146.82	88.87	87.06	87.97	0.168
42	162.85	158.62	160.74	88.66	88.34	88.50	0.080
43	164.41	148.93	156.67	88.97	87.47	88.22	0.237
44	161.77	152.27	157.02	88.99	88.14	88.57	0.122
52	165.70	157.33	161.52	88.51	87.56	88.04	0.150
53	165.49	153.33	159.41	88.67	87.26	87.97	0.183
54	163.77	156.22	160.00	88.60	87.76	88.18	0.104
61	162.06	157.28	159.67	87.92	87.14	87.53	0.088
62	161.80	152.37	157.09	88.16	86.62	87.39	0.146
63	161.01	152.32	156.67	88.21	86.85	87.53	0.121
71	156.43	149.80	153.12	87.61	86.18	86.90	0.106
72	155.64	147.18	151.41	87.78	85.97	86.88	0.121
73	153.99	148.19	151.09	87.71	86.47	87.09	0.078

Table 15: Velocity and Angle of attack of the HC for the 7mm injection distance

ID	U_{mag} [m/s]			ϕ [^{o}]			Period fraction
	Entry	Exit	Average	Entry	Exit	Average	
1	152.53	145.59	149.06	87.36	85.71	86.54	0.103
2	151.85	144.45	148.15	87.42	85.68	86.55	0.102
12	147.96	139.93	143.95	87.48	85.30	86.39	0.115
22	147.23	141.15	144.19	87.83	86.43	87.13	0.092
23	145.21	139.98	142.60	87.73	86.50	87.12	0.071
32	155.42	146.59	151.01	88.72	87.47	88.10	0.160
33	154.86	140.84	147.85	88.89	87.04	87.97	0.186
42	165.05	153.20	159.13	88.75	87.77	88.26	0.203
43	165.13	149.49	157.31	88.87	87.52	88.20	0.225
44	162.03	155.42	158.73	88.73	88.28	88.51	0.082
51	166.60	159.43	163.02	88.34	87.63	87.99	0.133
52	166.59	155.62	161.11	88.48	87.33	87.91	0.178
53	166.41	154.83	160.62	88.54	87.36	87.95	0.168
61	163.26	155.33	159.30	87.99	86.81	87.40	0.131
62	163.01	153.39	158.20	88.09	86.70	87.40	0.140
63	161.08	157.00	159.04	87.84	87.27	87.56	0.055
71	157.88	149.78	153.83	87.64	86.07	86.86	0.121
72	157.11	149.75	153.43	87.63	86.26	86.95	0.100

Table 16: Velocity and Angle of attack of the HC for the 2cm injection distance

ID	U_{mag} [m/s]			ϕ [^{o}]			Period fraction
	Entry	Exit	Average	Entry	Exit	Average	
0	152.70	144.66	148.68	87.41	85.56	86.49	0.112
1	151.40	146.99	149.20	87.19	86.21	86.70	0.059
11	148.14	139.93	144.04	87.50	85.35	86.43	0.112
21	147.65	138.43	143.04	88.04	85.82	86.93	0.133
31	155.93	142.69	149.31	88.84	86.93	87.89	0.207
32	152.91	144.33	148.62	88.74	87.82	88.28	0.104
40	165.12	155.34	160.23	88.66	87.94	88.30	0.177
41	165.50	150.72	158.11	88.79	87.55	88.17	0.229
42	165.01	150.53	157.77	88.83	87.74	88.29	0.192
50	166.74	156.82	161.78	88.38	87.41	87.90	0.163
51	166.65	155.09	160.87	88.46	87.31	87.89	0.171
52	165.81	157.37	161.59	88.42	87.63	88.03	0.115
60	163.60	154.23	158.92	88.03	86.72	87.38	0.142
61	162.83	154.79	158.81	87.99	86.90	87.45	0.110
70	158.11	149.53	153.82	87.65	86.06	86.86	0.121
71	156.25	153.07	154.66	87.35	86.79	87.07	0.042

Table 17: Velocity and Angle of attack of the HC for the 2.5cm injection distance

ID	U_{mag} [m/s]			ϕ [^{o}]			Period fraction
	Entry	Exit	Average	Entry	Exit	Average	
0	153.01	145.00	149.01	87.42	85.67	86.55	0.108
10	148.57	142.77	145.67	87.32	85.88	86.6	0.085
11	148.08	141.29	144.69	87.40	85.71	86.56	0.091
21	147.65	137.53	142.59	88.10	85.63	86.87	0.142
30	155.43	147.55	151.49	88.66	87.60	88.13	0.143
31	156.02	141.02	148.52	88.88	86.82	87.85	0.211
40	165.52	152.20	158.86	88.70	87.65	88.18	0.217
41	165.22	150.09	157.66	88.77	87.59	88.18	0.209
42	163.52	154.19	158.86	88.72	88.11	88.42	0.116
50	166.95	155.78	161.37	88.39	87.34	87.87	0.168
51	166.58	156.12	161.35	88.41	87.43	87.92	0.147
60	163.78	154.42	159.10	88.02	86.75	87.39	0.134
61	161.85	158.13	159.99	87.76	87.27	87.52	0.050
70	158.17	150.58	154.38	87.59	86.25	86.92	0.103

Table 18: Velocity and Angle of attack of the HC for the 3cm injection distance

ID	U_{mag} [m/s]			ϕ [^{o}]			Period fraction
	Entry	Exit	Average	Entry	Exit	Average	
0	152.97	146.35	149.66	87.33	85.93	86.63	0.087
10	148.78	141.04	144.91	87.44	85.49	86.47	0.108
11	147.29	144.29	145.79	87.09	86.39	86.74	0.040
21	147.17	137.99	142.58	88.03	85.85	86.94	0.124
30	156.12	143.73	149.93	88.78	87.06	87.92	0.198
31	155.26	141.41	148.34	88.85	87.14	88.00	0.179
40	165.65	150.66	158.16	88.72	87.57	88.15	0.220
41	164.95	151.31	158.13	88.74	87.79	88.27	0.176
50	167.12	156.07	161.60	88.38	87.38	87.88	0.160
51	165.94	159.06	162.50	88.30	87.69	88.00	0.094
60	163.62	156.13	159.88	87.93	86.97	87.45	0.103
70	157.67	153.15	155.41	87.41	86.65	87.03	0.060

Table 19: Velocity and Angle of attack of the HC for the 3.5cm injection distance

ID	U_{mag} [m/s]			ϕ [^{o}]			Period fraction
	Entry	Exit	Average	Entry	Exit	Average	
0	152.20	149.17	150.69	87.06	86.45	86.76	0.040
10	149.05	140.47	144.76	87.51	85.35	86.43	0.117
20	147.75	140.64	144.20	87.90	86.31	87.11	0.104
21	146.44	139.66	143.05	87.87	86.34	87.11	0.090
30	156.26	141.70	148.98	88.83	86.84	87.84	0.211
31	153.72	144.55	149.14	88.74	87.82	88.28	0.110
40	165.62	150.56	158.09	88.71	87.63	88.17	0.206
41	163.97	154.68	159.33	88.66	88.10	88.38	0.115
50	166.82	157.88	162.35	88.31	87.55	87.93	0.124
60	162.02	160.11	161.07	87.64	87.40	87.52	0.026

Table 20: Velocity and Angle of attack of the HC for the 4cm injection distance

ID	U_{mag} [m/s]			ϕ [^{o}]			Period fraction
	Entry	Exit	Average	Entry	Exit	Average	
11	149.21	140.73	144.97	87.50	85.43	86.47	0.113
21	148.07	138.74	143.41	88.04	85.88	86.96	0.132
31	156.08	141.06	148.57	88.84	86.92	87.88	0.201
41	165.04	151.91	158.48	88.67	87.83	88.25	0.168
51	165.56	161.90	163.73	88.15	87.86	88.01	0.050

Table 21: Velocity and Angle of attack of the HC for the 4.5cm injection distance

ID	U_{mag} [m/s]			ϕ [^{o}]			Period fraction
	Entry	Exit	Average	Entry	Exit	Average	
10	149.16	141.70	145.43	87.43	85.68	86.56	0.097
20	148.18	137.91	143.05	88.09	85.69	86.89	0.142
30	155.54	141.72	148.63	88.82	87.21	88.02	0.175
40	164.11	154.63	159.37	88.61	88.07	88.34	0.117

Table 22: Velocity and Angle of attack of the HC for the 5cm injection distance

ID	LC	HC 7mm	HC 2cm	HC 2.5cm	HC 3cm	HC 3.5cm	HC 4cm	HC 4.5cm	HC 5cm
0	0	0	0.206	0.238	0.216	0.175	0	0	0
1	0	0.170	0.204	0.118	0	0	0	0	0
2	0.230	0.228	0	0	0	0	0	0	0
3	0.244	0.138	0	0	0	0	0	0	0
10	0	0	0	0	0.170	0.217	0.225	0.225	0.194
11	0	0	0.230	0.224	0.182	0.079	0	0	0
12	0.196	0.224	0	0	0	0	0	0	0
13	0.242	0.166	0	0	0	0	0	0	0
20	0	0	0	0	0	0	0.264	0.264	0.284
21	0	0	0.185	0	0.284	0.249	0	0	0
22	0	0.242	0.142	0	0	0	0	0	0
23	0.272	0.152	0	0	0	0	0	0	0
30	0	0	0	0	0.286	0.396	0.402	0.402	0.349
31	0	0	0.320	0.414	0.422	0.358	0	0	0
32	0	0.256	0.371	0.210	0	0	0	0	0
33	0.266	0.336	0	0	0	0	0	0	0
34	0.234	0	0	0	0	0	0	0	0
40	0	0	0	0.354	0.434	0.441	0.336	0.336	0.232
41	0	0	0.408	0.456	0.419	0.353	0	0	0
42	0	0.160	0.450	0.384	0.232	0	0	0	0
43	0	0.474	0.165	0	0	0	0	0	0
44	0.450	0.244	0	0	0	0	0	0	0
50	0	0	0.266	0.326	0.338	0.320	0.099	0.099	0
51	0	0	0	0.342	0.294	0.188	0	0	0
52	0	0.300	0.355	0.230	0	0	0	0	0
53	0.360	0.368	0	0	0	0	0	0	0
54	0.400	0.208	0	0	0	0	0	0	0
60	0	0	0.262	0.284	0.269	0.206	0	0	0
61	0	0.176	0.280	0.221	0.101	0	0	0	0
62	0.218	0.292	0.111	0	0	0	0	0	0
63	0.346	0.242	0	0	0	0	0	0	0
64	0.268	0	0	0	0	0	0	0	0
70	0	0	0.243	0.241	0.206	0.120	0	0	0
71	0	0.214	0.201	0.084	0	0	0	0	0
72	0.234	0.241	0	0	0	0	0	0	0
73	0.284	0.157	0	0	0	0	0	0	0
74	0.140	0	0	0	0	0	0	0	0

Table 23: Probability of Impact on a specific sample (complete table)

References

[1] R. H. Smith A. F. Zahm and F. A. Louden. Forces on elliptic cylinders in uniform air stream. Technical report, Aerodynamical Laboratory, Bureau of Construction and Repair United States Navy.

[2] Airfoil tools. `http://airfoiltools.com/airfoil/details?airfoil=griffith30symsuction-il&fbclid=IwAR0JZ_7Gf-iS0gOVU4czHDk0vYYB-TbQ58NPYM-hV_tjhEk2MCqhF3iyI0E`. Accessed: April 2019.

[3] Inc. ANSYS. *ANSYS FLUENT 12.0 User's Guide*. ANSYS, Inc.

[4] Inc. ANSYS. *ANSYS FLUENT Theory Guide*. ANSYS, Inc.

[5] Inc. ANSYS. *FLUENT 6.3 Text Command List*. ANSYS, Inc.

[6] Inc. ANSYS. *FLUENT 6.3 UDF Manual*. ANSYS, Inc.

[7] André Bakker. Applied computational fluid dynamics, lecture 7 - meshing. `http://www.bakker.org`, 2006.

[8] Etienne Bousser. *SOLID PARTICLE EROSION MECHANISMS OF PROTECTIVE COATINGS FOR AEROSPACE APPLICATIONS*. PhD thesis, Université de Montréal, April 2013.

[9] William K. George. Lectures in turbulence for 21st century. `http://www.turbulence-online.com/index.html`, January 2013.

[10] Jr. George F. Schmitt. Liquid and solid particle impact erosion. Technical report, WRIGHT-PATTERSON AIR FORCE BASE, OHIO 45433, November 1979.

[11] Kristian Haller Knezevic. *High-Velocity Impact of a Liquid Droplet on a Rigid Surface: The Effect of Liquid Compressibility*. PhD thesis, SWISS FEDERAL INSTITUTE OF TECHNOLOGY ZURICH, Octobre 2002.

[12] Lukasz Paluszek. Lecture: Actuator disk udf for ansys fluent. EUROCOPTER.

[13] PhD Pietro Asinari. Lecture, multiphase flows: Basic physics and engineering modeling, Spring 2007.

[14] Faway Massouh Rodeyna Amer, Ivan Dobrev. Determination af wind turbine far wake using actuator disk. *Valencia Global 2014, Escuela Técnica Superior de Ingenieria del Diseno*, pages 254–260, June 2014.

[15] Ju Chen Jingrong Zhao Ming Liang Rong Liu, Kuiying Chen. Simulation studies of solid-particle and liquid-drop erosion of nial alloy. *International Journal of Environmental, Chemical, Ecological, Geological and Geophysical Engineering*, 9(5), 2015.

[16] SW _ TECCOMA. Formulaire appel à projets pôles de compétitivité. pages 33-36.

[17] Wallonia.be. https://www.awex-export.be/fr/plus-d-infos/actualites/les-materiaux-composites-dans-l-aeronautique?fbclid=IwAR0JZ_7Gf-iS0gOVU4czHDk0vYYB-TbQ58NPYM-hV_tjhEk2MCqhF3iyI0E. Accessed: June 2019.

UNIVERSITÉ CATHOLIQUE DE LOUVAIN
École polytechnique de Louvain
Rue Archimède, 1 bte L6.11.01, 1348 Louvain-la-Neuve, Belgique | **www.uclouvain.be/epl**